

The low-lying photonresponse of the even-even chromium isotopes

Ries, Philipp
(2020)

DOI (TUprints): <https://doi.org/10.25534/tuprints-00011909>

Lizenz:



CC-BY-SA 4.0 International - Creative Commons, Attribution Share-alike

Publikationstyp: Ph.D. Thesis

Fachbereich: 05 Department of Physics

Quelle des Originals: <https://tuprints.ulb.tu-darmstadt.de/11909>

The low-lying photonresponse of the even-even chromium isotopes

Die niedrig-liegende Photonenresponse der gerade-gerade Chromiumisotope

Zur Erlangung des Grades eines Doktors der Naturwissenschaften
(Dr. rer. nat.)

genehmigte Dissertation im Fachbereich Physik von Philipp Christian Ries aus Hadamar

Tag der Einreichung: 11. Mai 2020, Tag der Prüfung: 22. Juni 2020

1. Gutachten: Prof. Dr. Dr. h.c. Norbert Pietralla

2. Gutachten: Prof. Dr. Joachim Enders

Darmstadt – D 17



TECHNISCHE
UNIVERSITÄT
DARMSTADT

Fachbereich Physik
Institut für Kernphysik
AG Pietralla

Supported by the DFG
through CRC 1245



HGS-HiRe for FAIR
Helmholtz Graduate School for Hadron and Ion Research

The low-lying photonresponse of the even-even chromium isotopes
Die niedrig-liegende Photonenresponse der gerade-gerade Chromiumisotope

genehmigte Dissertation im Fachbereich Physik von Philipp Christian Ries

1. Gutachten: Prof. Dr. Dr. h.c. Norbert Pietralla

2. Gutachten: Prof. Dr. Joachim Enders

Tag der Einreichung: 11. Mai 2020

Tag der Prüfung: 22. Juni 2020

Darmstadt – D 17

Bitte zitieren Sie dieses Dokument als:

URN: urn:nbn:de:tuda-tuprints-119097

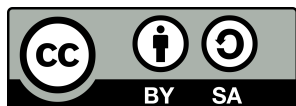
URL: <http://tuprints.ulb.tu-darmstadt.de/id/eprint/11909>

Dieses Dokument wird bereitgestellt von tuprints,

E-Publishing-Service der TU Darmstadt

<http://tuprints.ulb.tu-darmstadt.de>

tuprints@ulb.tu-darmstadt.de



Die Veröffentlichung steht unter folgender Creative Commons Lizenz:

Namensnennung – Weitergabe unter gleichen Bedingungen

4.0 International

<http://creativecommons.org/licenses/by-sa/4.0/>

Erklärungen laut Promotionsordnung

§8 Abs. 1 lit. c PromO

Ich versichere hiermit, dass die elektronische Version meiner Dissertation mit der schriftlichen Version übereinstimmt.

§8 Abs. 1 lit. d PromO

Ich versichere hiermit, dass zu einem vorherigen Zeitpunkt noch keine Promotion versucht wurde. In diesem Fall sind nähere Angaben über Zeitpunkt, Hochschule, Dissertationsthema und Ergebnis dieses Versuchs mitzuteilen.

§9 Abs. 1 PromO

Ich versichere hiermit, dass die vorliegende Dissertation selbstständig und nur unter Verwendung der angegebenen Quellen verfasst wurde.

§9 Abs. 2 PromO

Die Arbeit hat bisher noch nicht zu Prüfungszwecken gedient.

Darmstadt, den 11. Mai 2020

Philipp Christian Ries



Abstract

Most of this work is dedicated to the nuclear photonresponse of the stable even-even chromium isotopes. These nuclei are of great interest, due to their unique position at the lower end of the medium heavy nuclei and with regards to magic nucleon number. They were investigated with the nuclear resonance fluorescence method at the accelerator facilities of the Darmstadt super-conducting electron accelerator S-DALINAC and the High-Intensity γ -ray Source HI γ S. Numerous excited states were observed, many of those for the first time. Spin and parity quantum numbers as well as transition strengths were determined for these states.

This enables the photonresponse to be distinguished between electric and magnetic dipole strength distribution. Therefore, it is possible to analyze the behavior of known modes, such as the scissors mode, the spin-flip resonance and in particular the pygmy dipole resonance, across a shell closure. In order to do so, the interpretation of the obtained data is supported by calculations within the nuclear shell model and the relativistic mean-field model.



Zusammenfassung

Diese Arbeit beschäftigt sich maßgeblich mit der nuklearen Photonenresponse der stabilen geraden-geraden Chromisotope. Diese Kerne sind aufgrund ihrer einzigartigen Lage am unteren Ende der mittelschweren Kerne und in Bezug auf magische Nukleonenzahlen von großem Interesse. Sie wurden mittels der Methode der Kernresonanzfluoreszenz an den Beschleunigereinrichtungen des supraleitenden Darmstädter Elektronenbeschleunigers S-DALINAC und der High-Intensity γ -ray Source HI γ S vermessen. Mit dem Einsatz von reellen Photonen als Probe wurden zahlreiche Zustände beobachtet, viele davon zum ersten Mal. Für die beobachteten Zustände konnten Spin- und Paritätsquantenzahlen sowie Übergangsstärken bestimmt werden.

Dies gestattet die Unterscheidung der Photonenresponse zwischen elektrischer und magnetischer Dipolestärkeverteilung. Somit ist es möglich, das Verhalten bekannter Moden, wie der Scherenmode und der Spin-Flip-Resonanz, insbesondere aber der Pygmy Dipol Resonanz, über einen Schalenabschluss hinweg zu untersuchen. Die Interpretation der erhobenen Daten wird dabei durch Rechnungen im Schalenmodell und im relativistic mean-field Modell unterstützt.

Contents

| | | |
|----------|---|-----------|
| 1 | Introduction | 1 |
| 1.1 | Nuclear shell model | 2 |
| 1.2 | Dipole excitation | 4 |
| 1.2.1 | Magnetic dipole excitation | 5 |
| 1.2.2 | Electric dipole excitation | 7 |
| 2 | Motivation | 11 |
| 3 | Nuclear resonance fluorescence | 13 |
| 3.1 | Basics | 14 |
| 3.2 | NRF with unpolarized photons | 16 |
| 3.3 | NRF with quasi-monoenergetic polarized photon beam | 19 |
| 4 | Experimental setup | 23 |
| 4.1 | S-DALINAC | 23 |
| 4.2 | DHIPS | 24 |
| 4.3 | HI γ S | 25 |
| 4.4 | γ^3 -setup | 26 |
| 4.5 | Experimental details | 31 |
| 5 | Analysis | 33 |

| | | |
|----------|---|------------|
| 5.1 | Energy calibration | 33 |
| 5.2 | Detector efficiency and photon number | 34 |
| 5.2.1 | Efficiency calibration | 36 |
| 5.2.2 | Photon flux calibration | 36 |
| 5.2.3 | Parity and spin quantum numbers | 37 |
| 6 | Results | 41 |
| 6.1 | Results for ^{50}Cr | 41 |
| 6.1.1 | Revised transition strength | 41 |
| 6.1.2 | Average branching ratios | 43 |
| 6.2 | Results for ^{54}Cr | 44 |
| 6.2.1 | Parity quantum numbers | 45 |
| 6.2.2 | Spin quantum numbers | 47 |
| 6.2.3 | Cross section | 49 |
| 6.2.4 | Average branching ratios | 57 |
| 7 | Discussion | 59 |
| 7.1 | Magnetic dipole strength | 59 |
| 7.2 | Electric dipole strength | 65 |
| 8 | Summary | 73 |
| A | Spectra of the measurements of the isotope ^{54}Cr | 75 |
| A.1 | Spectra recorded at DHIPS | 76 |
| A.1.1 | Endpoint energy 7.5 MeV | 76 |
| A.1.2 | Endpoint energy 9.7 MeV | 78 |
| A.2 | Spectra recorded at HI γ S | 81 |
| B | LINTOTT scattering chamber | 101 |
| C | Gas target | 105 |

| | |
|-----------------------------|------------|
| Bibliography | 111 |
| Lebenslauf | 119 |
| List of publications | 121 |
| Danksagung | 123 |

List of Figures

| | | |
|-----|--|----|
| 1.1 | The nuclear shell structure | 3 |
| 1.2 | The magnetic dipole response | 6 |
| 1.3 | Spin-flip transition | 7 |
| 1.4 | The electric dipole response | 8 |
| 3.1 | The NRF process | 15 |
| 3.2 | Angular Distribution | 18 |
| 3.3 | Azimuthal angular distribution | 20 |
| 4.1 | Schematic of the S-DALINAC | 24 |
| 4.2 | Schematic of DHIPS | 28 |
| 4.3 | Schematic of HI γ S | 29 |
| 4.4 | Schematic γ^3 -setup | 30 |
| 5.1 | Energy resolution detector 1 | 35 |
| 5.2 | Detector efficiency | 38 |
| 5.3 | Photon flux calibration | 39 |
| 6.1 | Average branching ratios in ^{50}Cr | 44 |
| 6.2 | Cutout of ^{54}Cr DHIPS spectra | 45 |
| 6.3 | Azimuthal asymmetry | 46 |
| 6.4 | Ratio of angular distribution | 47 |
| 6.5 | Average branching ratios in ^{54}Cr | 57 |

| | | |
|------|---|----|
| 7.1 | Magnetic dipole transition strengths | 63 |
| 7.2 | Shell model calculation | 64 |
| 7.3 | Electric dipole transition strengths | 66 |
| 7.4 | Thomas-Reiche-Kuhn sum rule | 67 |
| 7.5 | Neutron skin thickness in Cr isotopes | 71 |
| 7.6 | Running sum of transition widths | 72 |
| | | |
| A.1 | DHIPS endpoint energy of 7.5 MeV, range: 2.5 to 5.1 MeV . . | 76 |
| A.2 | DHIPS endpoint energy of 7.5 MeV, range: 5.1 to 7.5 MeV . . | 77 |
| A.3 | DHIPS endpoint energy of 9.7 MeV, range: 2.5 to 5.1 MeV . . | 78 |
| A.4 | DHIPS endpoint energy of 9.7 MeV, range: 5.1 to 7.5 MeV . . | 79 |
| A.5 | DHIPS endpoint energy of 9.7 MeV, range: 7.5 to 10 MeV . . | 80 |
| A.6 | HI γ S beam setting 5.5 MeV | 81 |
| A.7 | HI γ S beam setting 5.7 MeV | 82 |
| A.8 | HI γ S beam setting 5.9 MeV | 83 |
| A.9 | HI γ S beam setting 6.1 MeV | 84 |
| A.10 | HI γ S beam setting 6.3 MeV | 85 |
| A.11 | HI γ S beam setting 6.5 MeV | 86 |
| A.12 | HI γ S beam setting 6.7 MeV | 87 |
| A.13 | HI γ S beam setting 6.9 MeV | 88 |
| A.14 | HI γ S beam setting 7.1 MeV | 89 |
| A.15 | HI γ S beam setting 7.3 MeV | 90 |
| A.16 | HI γ S beam setting 7.5 MeV | 91 |
| A.17 | HI γ S beam setting 7.7 MeV | 92 |
| A.18 | HI γ S beam setting 7.9 MeV | 93 |
| A.19 | HI γ S beam setting 8.2 MeV | 94 |
| A.20 | HI γ S beam setting 8.5 MeV | 95 |
| A.21 | HI γ S beam setting 8.8 MeV | 96 |
| A.22 | HI γ S beam setting 9.1 MeV | 97 |
| A.23 | HI γ S beam setting 9.4 MeV | 98 |
| A.24 | HI γ S beam setting 9.7 MeV | 99 |

| | |
|---|-----|
| A.25 HI γ S beam setting 10.0 MeV | 100 |
| B.1 New scattering chamber design | 102 |
| B.2 Technical drawing: New scattering chamber top view | 104 |
| B.3 Technical drawing of the new scattering chamber side view | 104 |
| C.1 Comparison of gaseous target designs | 106 |
| C.2 Technical drawing: New target container | 107 |
| C.3 Technical drawing: Support frame | 108 |
| C.4 Gas target leak rate | 109 |

List of Tables

| | | |
|-----|--|----|
| 4.1 | Experimental details of the DHIPS campaign | 31 |
| 4.2 | Experimental details of the HI γ S campaign | 32 |
| 5.1 | Energy resolution at DHIPS | 34 |
| 6.1 | Revised results for ^{50}Cr | 42 |
| 6.2 | Quantum numbers ^{54}Cr | 50 |
| 6.3 | Transition strength of ^{54}Cr | 53 |
| 7.1 | Nuclear matrix elements | 61 |

1. Introduction

Nuclear physics arose as a new discipline at the end of the 19th century with the discovery of radioactivity by Henri Becquerel [1] as well as Marie and Pierre Curie [2]. Soon after, Earnest Rutherford performed the first nuclear scattering experiments, which ultimately led to the development of the Rutherford model of the atom [3]. The characteristic elements of this atomic model, namely an outer electron hull and an inner, positively charged nucleus, remain prevalent today. After the discovery of the neutron by James Chadwick [4] in 1932, Werner Heisenberg was able to formulate his model on the composition of atomic nuclei [5], which describes protons and neutrons as their constituents. Further advances were made by George Gamow amongst others. In his semi-classical liquid-drop model the protons and neutrons are collectively treated as an incompressible fluid, much like molecules in a drop of liquid [6]. One of the most important and far reaching developments for nuclear physics was the shell model (SM) promoted by various recognizable physicists including and based on the work of Maria Goeppert Mayer [7].

1.1. Nuclear shell model

Maria Goeppert Mayer created the foundation for the SM when she examined the elements for their number of isotopes and isotones as well as their natural abundances [7]. She reported particular high stability and abundances for nuclei with 20, 50, 82 and 126 protons or neutrons. These and the numbers 2, 8 and 28 will later be referred to as *magic numbers*. Key element of the SM is the grouping of the protons and neutrons into orbitals. These orbitals are described by three quantum numbers: the main quantum number n , the angular momentum quantum number l and the total angular momentum quantum number j . They are noted in the fashion of nl_j . Here, spectroscopic notation are used for l , starting with s, p, d, f instead of 0, 1, 2 and 3 respectively and continuing in further alphabetic order from there on. The total angular momentum quantum number j originates from the coupling between the angular momentum l and the spin $s = 1/2$ of the nucleons and may take the values $j = l \pm s$. It defines the maximum number of nucleons in the respective orbit equal to $j \cdot 2 + 1$, due to the range of its possible projections, represented by the magnetic quantum number m_j , of $m_j = [-j, -j + 1, \dots, j - 1, j]$. Applying a potential, which resembles that of a nucleus, for instance a Woods-Saxon potential [8], energy levels for the orbitals as shown in Figure 1.1 are reproduced. The orbitals are split due the spin-orbit interaction, which gives rise to the energetic spacing of the orbitals. It appears self-evident to group them together to so-called shells. Following the interpretation of the shell model, these levels are filled from the bottom up with nucleons in order to recreate a nucleus' energetic lowest configuration, the ground state. Here, the Pauli Principle prohibits any two nucleons to receive the same combination of quantum numbers, which also implies, that protons and neutrons fill their respective orbitals independent of each other. In this way the magic numbers are reproduced, as they correspond to the numbers of either protons or neutrons necessary to fill any shell.

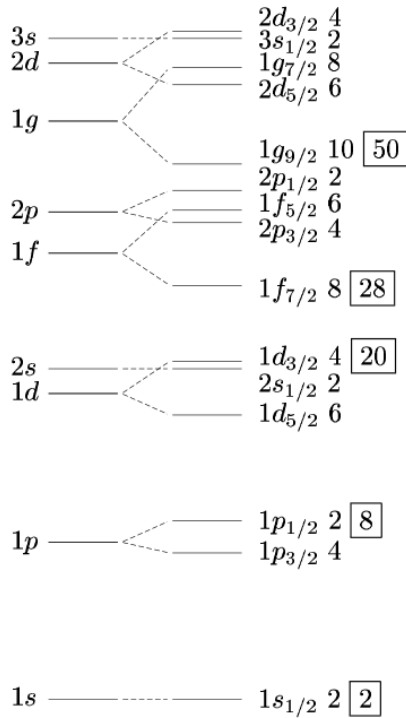


Figure 1.1.: Schematic representation of the nuclear shell structure: The graphic illustrates the splitting of the nuclear orbitals and their energy spacing. The number to the right of the orbital denomination nl_j indicates the maximal occupation number. The biggest gaps separate the shells and are here highlighted by the corresponding particle number in frames. Graphic taken from [9]

This system of filled up orbitals can be excited, if external energy is provided to lift one or more nucleons into higher-lying orbitals, collectively called valence

space. This interpretation is capable to explain various phenomena, as will be discussed in further sections of this chapter. One evident example is the increased level energy of first excited states in (doubly) magic nuclei, as here the excitation requires to lift at least one particle across a shell gap.

Yet, it is not possible to explain all phenomena observed within the nuclear shell model, in particular collective excitations. These will also be part of the following sections.

1.2. Dipole excitation

Nuclear transitions can be categorized by the electromagnetic character σ and angular momentum transfer (also multipole order) L . Since angular momentum is preserved, the nucleus' total angular momentum of the initial state J_i^π and of the final state J_f^π limit the allowed momentum transfer according to the triangle inequality:

$$|J_i^\pi - J_f^\pi| \leq L \leq J_i^\pi + J_f^\pi \quad (1.1)$$

The radiation character σ is determined in combination with the parity π . It is either $\sigma = E$ for electric transitions, if

$$\pi_i = (-1)^L \cdot \pi_f, \quad (1.2)$$

or $\sigma = M$ for magnetic transitions, if

$$\pi_i = (-1)^{L+1} \cdot \pi_f. \quad (1.3)$$

In general, this leads to a range of combinations σL for a given transition. However, in nuclei with an even number of protons and even number of neutrons (even-even nuclei) the ground state is always $J^\pi = 0^+$, due to the pairing of protons and neutrons. Therefore, Equation (1.1) is effectively reduced

to $L = J_{\text{excited}}$ for transitions from and to the ground state (ground state transitions), allowing only pure transitions of σL . According to the multipole order, nuclear excitations with $L = 1$ are referred to as dipole excitations, which are divided into electric dipole excitation, $E1$, and magnetic dipole excitation, $M1$.

1.2.1. Magnetic dipole excitation

For nearly spherical nuclei in the mass region of $A \approx 50$, also called fp -shell, one typically can distinguish two magnetic dipole excitation modes, as described in Ref. [10] and shown in Figure 1.2. At lower energies of 2-4 MeV, a two-phonon state is observed. This state results from the $[2_1^+ \otimes 2_{ms}^+]$ coupling of the quadrupole phonons of the first excited 2^+ state and of the first mixed symmetric 2_{ms}^+ state [11]. This has been demonstrated within the framework of the extended interacting boson model (IBM-2) [12], where nuclear excitations are considered in terms of pairs of protons or neutrons coupling in the valence space, called bosons. Here, the first excited 2^+ state is considered symmetric in respect to the exchange of the bosons. One example is the wave function

$$|\Phi_1\rangle = \frac{1}{\sqrt{2}}(s_\pi^\dagger d_\nu^\dagger + d_\pi^\dagger s_\nu^\dagger) |0\rangle, \quad (1.4)$$

with the creation operators s^\dagger and d^\dagger for s - or d -bosons. An s - or d -boson corresponds to a coupled pair of nucleons in the same orbital with coupled $J = 0$ (s) or $J = 2$ (d), their indices π or ν specifying proton shell or neutron shell, respectively. In contrast to that, the mixed symmetric state is asymmetric in respect to the exchange of boson labels, as shown in this example:

$$|\Phi_2\rangle = \frac{1}{\sqrt{2}}(s_\pi^\dagger d_\nu^\dagger - d_\pi^\dagger s_\nu^\dagger) |0\rangle \quad (1.5)$$

In deformed nuclei, the 1^+ state resulting from the coupling of the symmetric state and mixed symmetric state is interpreted as a scissors-like isovector

oscillation of valence protons and neutrons and hence referred to as scissors mode.

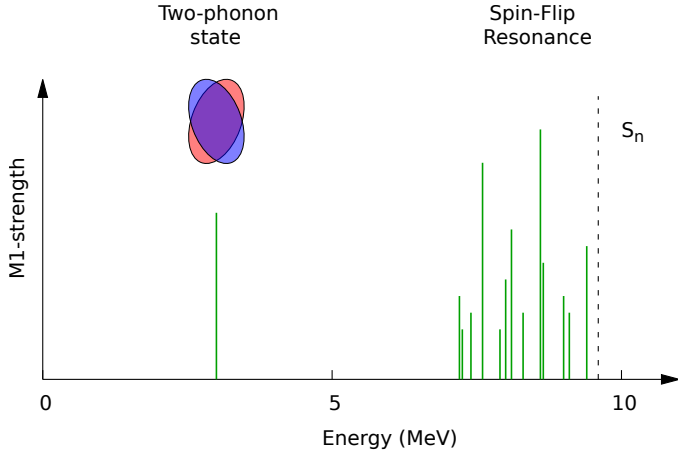


Figure 1.2.: Schematic of the typical magnetic dipole response of a nucleus in the $A = 50$ mass region: The scissors mode and spin-flip resonance usually are well separated by their respective excitation energies.

For distinctive higher excitation energies, an accumulation of magnetic dipole transitions, called spin-flip resonance, can be found. As the name suggests, the origin of the excited states of this resonance is a change of the sign of a nucleon's spin-orbit coupling $j = l + s$ to $j = l - s$. Its angular momentum l remains, which results in a change of the total angular momentum $\Delta j = 1$. This is illustrated in Figure 1.3 for the proton shell of the chromium isotopes, populating the $1f_{7/2}$ orbital with 4 protons in the ground state. Flipping the spin of one of these valence protons results in the population of the $1f_{5/2}$ orbital.

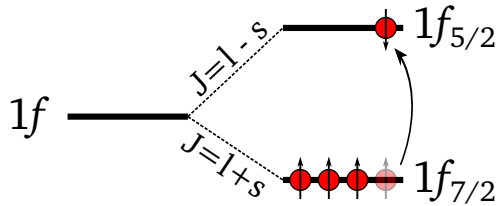


Figure 1.3.: Illustration of a spin-flip transition: The flipping of the spin, while the angular momentum remains unchanged, results in a change in total angular momentum of $\Delta j = 1$.

1.2.2. Electric dipole excitation

For electric dipole excitations, an even-even nucleus typically exhibits three phenomena. These are shown in Figure 1.4. At lower energies, up to 5 MeV, a two-phonon $J^\pi = 1^-$ state can be found. Analog to the scissors mode, this excitation is part of the spin quintuplet $J^\pi = 1^-, 2^-, \dots, 5^-$ resulting from the $[2_1^+ \otimes 3_1^-]$ coupling of the quadrupole phonon of the first excited 2^+ state and the octupole phonon of the first excited 3^- state [13]. An example, where the complete quintuplet was observed is given in Ref. [14]. Its excitation energy is usually close to the sum of excitation energies of the 2^+ and 3^- states, which indicates nearly harmonic coupling. Other indications for the two-phonon nature of these states are given by the reported correlations between the decay strengths of the involved phonons [15, 16].

Another phenomenon is the isovector giant dipole resonance (IVGDR), which is located at excitation energies of 10 to 20 MeV, well above the neutron separation threshold [17]. It has been one of the first nuclear excitations to be described and observed [18, 19, 20]. This continuous structure incorporates most of the experimentally observed electric dipole excitation strength of a given nucleus. This often is further quantified using the exhausted percentage of the Thomas-Reiche-Kuhn energy-weighted sum rule (EWSR) [21, 22],

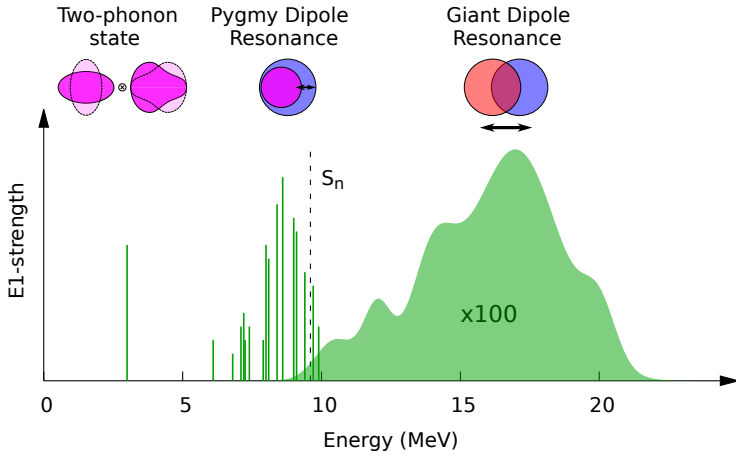


Figure 1.4.: Schematic of the typical electric dipole response of an even-even nucleus: The three depicted effects are most commonly observed: the two-phonon state below 5 MeV, the pygmy dipole resonance below and in the vicinity of the neutron separation threshold and the giant dipole resonance above that. Illustrations of these modes according to the liquid drop model are given with proton matter in red, neutron matter in blue and mixed matter in magenta.

which gives an estimation for expected overall dipole strength I_{total} of a given nucleus:

$$\sum_{\text{nucleons}} \sum_i \int dE_i \sigma_{0 \rightarrow i} = I_{\text{total}} \approx 60 \left(\frac{NZ}{A} \right) \text{MeV mb} \quad (1.6)$$

Derived in a single-particle picture, the summation of the integrated cross section $\int dE_i \sigma_{0 \rightarrow i}$ over all states i and all nucleons yields the total integrated cross section for electric dipole excitation I_{total} . The estimation for its value

only depends on the nucleus' neutron, proton and mass numbers N , Z and A . A well established interpretation considers the GDR as an out-of-phase oscillation of the protons against the neutrons [23].

Between the excitation energies of two-phonon state and IVGDR, the so-called pygmy dipole resonance (PDR) is observed. It originally refers to a accumulation of electric dipole strength in the vicinity of the neutron separation threshold. First observations of associated γ -ray strength after capture of thermal neutrons were reported by Bartholomew *et al.* [24] in the early 1960s. Later the term *pygmy* was coined in contrast to the vastly predominant *giant* dipole resonance [25]. Considering the EWSR, the PDR typically exhausts a few percent of the overall strength [26]. This mode is typically interpreted in terms of the liquid drop model as an oscillation of a balanced proton-neutron core against a neutron skin [23, 27, 28]. Its nature is not yet fully understood and therefore has continuously been the aim of ongoing research in nuclear structure. In this spirit, the motivation for this work is based on the demand of the scientific community for completion of experimental data available on the PDR and for the study of its evolution throughout the nuclear chart. This will be presented in detail in the following chapter.



2. Motivation

The comprehensive study of the PDR provides crucial insights to ongoing research in nuclear physics and related disciplines. This will be further clarified, as the connection of the PDR to the nuclear equation of state (EoS) will be established in this chapter. The EoS describes the energy per particle E in a nuclear system as a function of its density ρ and its asymmetry in nuclear matter $\alpha = (N - Z)/A$. Considering the lowest terms in a Taylor expansion around symmetric matter yields

$$E(\rho, \alpha) = E(\rho, 0) + S(\rho)\alpha^2 + \mathcal{O}(\alpha^4). \quad (2.1)$$

The term $S(\rho)$ is referred to as symmetry energy, which describes the variation in energy depending on the neutron-proton ratio. In turn, expanding the symmetry energy around saturation density ρ_0 results in

$$S(\rho) = J + L\frac{\rho - \rho_0}{3\rho_0}. \quad (2.2)$$

Dedicated research aims to restrict the parameters for the symmetry energy at saturation density J (in literature also referred to as a_4) and the slope parameter L . The variety of the approaches to restrict these parameters is presented in Ref. [29]. In this article, average values for these parameters determined from over 50 data sets amount to $J = 31.7 \pm 3.2$ MeV and $L = 58.7 \pm 28.1$ MeV. In particular, the uncertainty given for L demonstrates the necessity of further investigation.

In the first instance, the connection of the low-lying electric dipole strength associated with the PDR to the neutron skin thickness ΔR_{np} is a relevant factor. The neutron skin thickness can be defined by the difference

$$\Delta R_{np} = \sqrt{\langle r_n^2 \rangle} - \sqrt{\langle r_p^2 \rangle} \quad (2.3)$$

of the mean mass radius $\langle r_n^2 \rangle$ and mean charge radius $\langle r_p^2 \rangle$. Considering the semi-classical picture of the PDRs liquid drop model interpretation, this connection seems evident, as an increase of ΔR_{np} and thus an increase of the oscillating mass would be accompanied by an increased dipole moment. This of course, has been studied more rigorously. The EWSR is used to establish the correlation of low-lying electric dipole strength and neutron skin thickness, as the work of Klimkiewicz *et al.* [30] and Piekarewicz [31] amongst others demonstrates. In turn, the connection of the neutron skin thickness to the parameters of the EoS has been shown by Brown [28] or Roca-Maza and Paar [32].

With this connection of PDR to EoS established, the study of the low-lying electric dipole strength promises great insight. As crucial aspects of the PDR have not been examined until now, this work is dedicated to the investigation of the influence of shell effects on the PDR. Thus, focus of this work are nuclear structure aspects of the nuclei $^{50,52,54}\text{Cr}$. This group of isotopes is distinguished from the thousands of known isotopes by a unique set of properties. The chromium isotopic chain is the only one featuring stable isotopes below a neutron shell closure (in this case $N = 28$) as well as above, yet with natural abundances of several percent for each isotopes [33]. The latter allows for the production of highly enriched and comparatively large amounts of target material, providing the necessary conditions for photon scattering experiments. Thus, as of today, the chromium isotopic chain is the only case, where the study of nuclear structure across a neutron shell closure (or indeed any shell closure, considering isotonic chains as well) can be performed with real photons as probes.

3. Nuclear resonance fluorescence

Over several decades the nuclear resonance fluorescence method has proven itself as reliable tool in experimental nuclear physics [34, 35]. In particular, NRF is regularly applied in the studies of low-lying dipole transitions and their strength [13], as it is in this work. In general, this method provides access to the following observables of nuclear excited states:

- excitation energy E
- spin quantum number J
- parity quantum number π
- integrated cross section I
- transition width Γ
- transition strength $B(\sigma L)$
- branching ratio β and
- average branching ratio $\langle\beta\rangle$

This chapter will present the basic concepts of this method and will provide an overview of the accessibility of the listed observables. The nomenclature given here will be employed, if not stated otherwise.

3.1. Basics

The essential characteristic of NRF is the irradiation of the target material with real photons in order to populate excited nuclear levels and the detection of their decay via emission of γ -radiation. This is also referred to as *photon scattering*, which is not correct in the literal sense, as the incident photons are not scattered, but absorbed, with new photons being emitted. The process is visualized in Figure 3.1: A nucleus in its ground state with the energy E_0 and spin J_0 is excited to a higher state i with the energy E_i and spin J_i by absorption of a photon carrying the energy difference $E_i - E_0$. Subsequently, state i will decay either directly to the ground state or to one (of possibly many) intermediate state j with $E_i > E_j > E_0$. The decay to the ground state is often referred to as *elastic* transition/scattering, latter as *inelastic* transition/scattering. The process of populating an intermediate state via inelastic transitions is also called feeding.

The relative frequency of these possible decay channels is given by the branching ratios:

$$\beta_j = \frac{\Gamma_j}{\Gamma}, \quad (3.1)$$

determined by the individual transition widths Γ_j and the total transition width of the excited state $\Gamma = \sum_j \Gamma_j$. In turn Γ is connected with the lifetime of the state in question τ via

$$\Gamma = \frac{\hbar}{\tau}. \quad (3.2)$$

According to Ref.[36], the transition widths are connected to the cross section $\sigma_{0 \rightarrow i \rightarrow j}(E_\gamma)$ for the NRF process via

$$\sigma_{0 \rightarrow i \rightarrow j}(E_\gamma) = \frac{\pi}{2} \left(\frac{\hbar c}{E_i} \right)^2 \frac{2J_i + 1}{2J_0 + 1} \frac{\Gamma_0 \Gamma_{i \rightarrow j}}{(E_\gamma - E_i)^2 + \frac{\Gamma^2}{4}}, \quad (3.3)$$

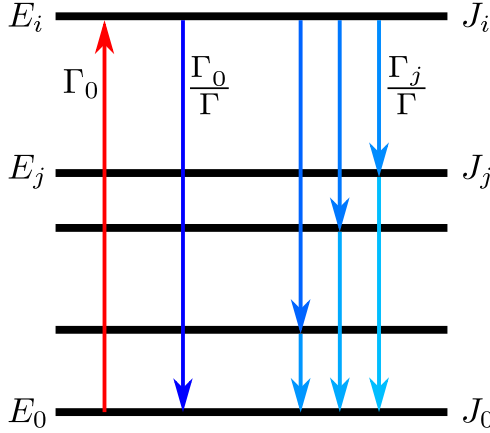


Figure 3.1.: Schematic of the NRF process: A nucleus is excited via a resonant absorbed photon and decays through emission of a photon. Various decay channels may be accessible.

where E_γ is the incident photons energy. The accessible observable in NRF experiments is the integrated cross section $I_{0 \rightarrow i \rightarrow j}(E_\gamma)$ defined by

$$I_{0 \rightarrow i \rightarrow j}(E_\gamma) = \int dE \sigma_{0 \rightarrow i \rightarrow j}(E_\gamma) = \pi^2 \cdot \left(\frac{\hbar c}{E_i} \right)^2 \cdot g \cdot \frac{\Gamma_0 \Gamma_j}{\Gamma}, \quad (3.4)$$

with the spin-dependent factor $g = \frac{2J_i+1}{2J_0+1}$.

In general, not all decay channels of an individual state are known. In most cases, only the ground state transition is observed, while possible other decays may be too weak to be detected against the background. In this case, the approximation $\Gamma \approx \Gamma_0$ is reasonable, so that the ground state transition width is determined via

$$\Gamma_0 = \frac{I_{0 \rightarrow i \rightarrow 0}}{\pi^2 \cdot \left(\frac{\hbar c}{E_i} \right)^2 \cdot g} \frac{\Gamma}{\Gamma_0} \approx \frac{I_{0 \rightarrow i \rightarrow 0}}{\pi^2 \cdot \left(\frac{\hbar c}{E_i} \right)^2 \cdot g}. \quad (3.5)$$

One should keep in mind, that any value of Γ_0 obtained with the aforementioned approximation is an lower limit and would be increased with every additional decay channel observed. The transition width is also connected to the reduced transition probability or transition strength $B(\sigma L)$ [35], which is frequently used in theoretical considerations:

$$\Gamma_j = 8\pi \sum_L \left(\frac{E_i - E_j}{\hbar c} \right)^{2L+1} \cdot \frac{L+1}{L((2L+1)!!)^2} \cdot B(\lambda L) \downarrow, \quad (3.6)$$

which yields the following for the transition typically observed in NRF:

$$\frac{B(E1) \uparrow}{[e^2 \text{fm}^2]} = 9.554 \cdot 10^{-4} \cdot g \cdot \frac{\Gamma_j}{[\text{meV}]} \cdot \left(\frac{[\text{MeV}]}{E_i} \right)^3 \quad (3.7)$$

$$\frac{B(M1) \uparrow}{[\mu_N^2]} = 8.641 \cdot 10^{-2} \cdot g \cdot \frac{\Gamma_j}{[\text{meV}]} \cdot \left(\frac{[\text{MeV}]}{E_i} \right)^3 \quad (3.8)$$

$$\frac{B(E2) \uparrow}{[e^2 \text{fm}^4]} = 1.245 \cdot 10^3 \cdot g \cdot \frac{\Gamma_j}{[\text{meV}]} \cdot \left(\frac{[\text{MeV}]}{E_i} \right)^5 \quad (3.9)$$

In particular, NRF experiments using bremsstrahlung for the production of photons are well suited for the determination of integrated cross sections and subsequently the transition strengths, since the continuous bremsstrahlung spectrum excites all available states simultaneously and only one measurement relative to a known standard is needed. The Equations (3.7) to (3.9) are applicable according to the multipole order and electromagnetic character of the transition radiation, as was described in the previous chapter. The NRF method offers access to the observables necessary to determine those.

3.2. NRF with unpolarized photons

In NRF experiments utilizing an unpolarized photon beam, such as it is provided by bremsstrahlung, the multipole order and consequently the spin quan-

tum number can be determined. This is accomplished by measuring the angular distribution of the intensity of emitted photons. The expected angular distribution $W(\theta)_{i \rightarrow j \rightarrow k}$ of a sequence of states $i \rightarrow j \rightarrow k$ via the two transitions γ_1 and γ_2 is known [37]:

$$W(\theta)_{i \rightarrow j \rightarrow k} = \sum_{\nu=\text{even}} B_\nu(\gamma_1) A_\nu(\gamma_2) P_\nu(\cos \theta) \quad (3.10)$$

Here, $P_\nu(\cos \theta)$ are the Legendre polynomials and θ is the polar angle between incident and emitted photon. The coefficients $B_\nu(\gamma_1)$ and $A_\nu(\gamma_2)$ are defined as:

$$B_\nu(\gamma_1) = \left(\frac{1}{1 + \delta^2(\gamma_1)} \right) \cdot [F_\nu(L_1 L_1 J_i J) - 2\delta(\gamma_1) F_\nu(L_1 L'_1 J_i J) + \delta^2(\gamma_1) F_\nu(L'_1 L'_1 J_i J)] \quad (3.11)$$

and

$$A_\nu(\gamma_2) = \left(\frac{1}{1 + \delta^2(\gamma_2)} \right) \cdot [F_\nu(L_2 L_2 J_k J) + 2\delta(\gamma_2) F_\nu(L_2 L'_2 J_k J) + \delta^2(\gamma_2) F_\nu(L'_2 L'_2 J_k J)]. \quad (3.12)$$

The F_ν coefficients are defined and tabulated in Ref. [38]. The multipole mixing ratio δ is considered, if transitions of different multipole order are possible. However, this is not the case for the excitation of an even-even nuclei from its 0^+ ground state to a $J = 1$ excited state and consecutive decay back to the ground state. The cascades $0^+_{g_s} \rightarrow 1^\pi \rightarrow 0^+_{g_s}$ and $0^+_{g_s} \rightarrow 2^\pi \rightarrow 0^+_{g_s}$ yield pure transitions as follows from Equation (1.1). The angular distributions for these two cases are written by:

$$W(\theta)_{0^+_{g_s} \rightarrow 1^\pi \rightarrow 0^+_{g_s}} = \frac{3}{4}(1 + \cos^2 \theta) \quad (3.13)$$

$$W(\theta)_{0^+_{g_s} \rightarrow 2^\pi \rightarrow 0^+_{g_s}} = \frac{5}{4}(1 - 3 \cos^2 \theta + 4 \cos^4 \theta) \quad (3.14)$$

The angular distributions are depicted in Figure 3.2. Comparing between dipole and quadrupole transitions, the ratio of each angular distribution at two separate angles

$$w_i = W_{0 \rightarrow i \rightarrow 0}(\alpha) / W_{0 \rightarrow i \rightarrow 0}(\beta) \quad (3.15)$$

differs the most for the angles of $\alpha = 90^\circ$ and $\beta = 127^\circ$. It is equal to $w_1 = 0.71$ for dipole and equal to $w_2 = 2.26$ for quadrupole transitions. Thus, the ratio w is determined for each excited state, considering the relative intensity recorded at 90° and 127° . The multipole order of the transition and the spin quantum number is assigned through the comparison with the ideal values of w_1 and w_2 .

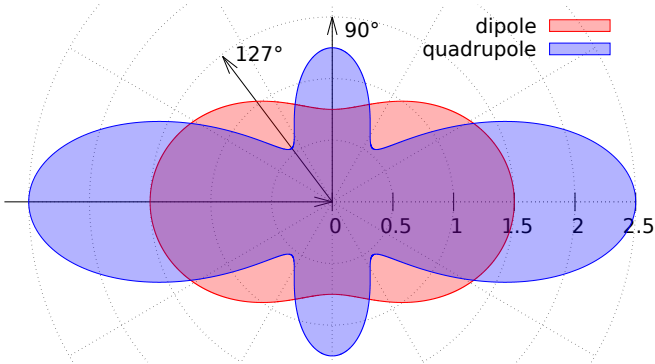


Figure 3.2.: Angular Distribution of NRF measurements: The angular distribution for the cascade $0_{gs}^+ \rightarrow 1^\pi \rightarrow 0_{gs}^+$ is shown in red, for $0_{gs}^+ \rightarrow 2^\pi \rightarrow 0_{gs}^+$ in blue. The direction of the beam is marked by the horizontal arrow. The angles, at which the angular distributions differ most, are 90° and 127° .

3.3. NRF with quasi-monoenergetic polarized photon beam

The usage of a polarized and quasi-monoenergetic photon beam offers access to additional observables. Polarized photons allow the determination of the parity quantum number and the resulting radiation character. Similar to the previous discussion, the angular distribution is used. If the incident photon is polarized Equation (3.10), yielding the angular distribution, has to be modified by an additional term. The new equation is given by [39, 40]:

$$\begin{aligned}
 W(\theta, \phi)_{i \rightarrow j \rightarrow k} = & \sum_{\nu=\text{even}} B_{\nu}(\gamma_1) A_{\nu}(\gamma_2) P_{\nu}(\cos \theta) \\
 & + \sum_{\nu=\text{even}} A_{\nu}(\gamma_2) \frac{1}{1 + \delta^2(\gamma_1)} \cos(2\phi) P_{\nu}^{(2)}(\cos \theta) \\
 & \cdot [(\pm)_{L_1} \kappa_{\nu}(L_1 L_2) F_{\nu}(L_1 L_2 J_i J) \\
 & + (-1)^{L_1 + L'_1} (\pm)_{L'_1} \kappa_{\nu}(L_1 L'_1) 2\delta F_{\nu}(L_1 L'_1 J_i J) \\
 & + (\pm)_{L'_1} \kappa_{\nu}(L'_1 L'_1) F_{\nu}(L'_1 L'_1 J_i J)]. \tag{3.16}
 \end{aligned}$$

Here, the polar angle θ is defined as before and ϕ gives the azimuthal angle between the polarization plane of the incident photons and the reaction plane, spanned by incident and emitted photon. The sign $(\pm)_L$ is determined by the radiation character, i.e. positive for electric transitions and negative for magnetic ones. The coefficients κ_{ν} are spin dependent factors as defined in Ref. [40]. This formula is substantially shorted, if all coefficients are filled in and the sequence $0_{gs}^+ \rightarrow 1^{\pi} \rightarrow 0_{gs}^+$ is considered:

$$W(\theta, \phi)_{0_{gs}^+ \rightarrow 1^{\pi} \rightarrow 0_{gs}^+} = 1 + \frac{1}{4} [3 \cos^2(\theta) - 1 + \pi_j 3 \cos(2\phi) \cdot (1 - \cos^2(\theta))], \tag{3.17}$$

with the parity quantum number π_j of the excited state. This allows for the determination of the parity quantum number via the azimuthal asymmetry

[41]. It is most advantageous to consider the pairs of angles $\theta = 90^\circ, \phi = 0^\circ$ and $\theta = 90^\circ, \phi = 90^\circ$, respectively, as for those angles $W(\theta, \phi)$ differs the most: $W(90^\circ, 0^\circ)$ is maximum, $W(90^\circ, 90^\circ)$ is minimal for magnetic transitions and vice versa for electric transitions, which is depicted in Figure 3.3. Accordingly, the analyzing power Σ , defined as

$$\Sigma = \frac{W(90^\circ, 0^\circ) - W(90^\circ, 90^\circ)}{W(90^\circ, 0^\circ) + W(90^\circ, 90^\circ)}, \quad (3.18)$$

is +1 for the former and -1 for the latter, which corresponds to the parity quantum number.

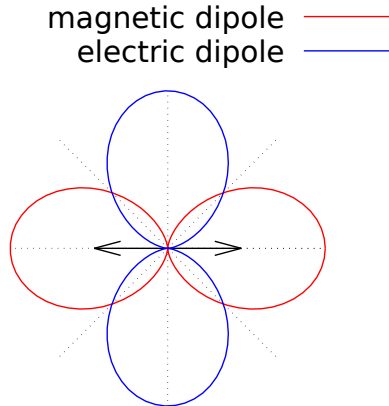


Figure 3.3.: Azimuthal angular distribution for a polarized photon beam: Shown are the angular distribution for elastic electric (blue) and elastic magnetic (red) dipole transitions in the plane orthogonal to the photon beam. The black arrow illustrates the polarization of the beam.

The experiment yields the azimuthal asymmetry ϵ via the intensities within the polarization plane I_{\parallel} and perpendicular I_{\perp} :

$$\epsilon = \frac{I_{\parallel} - I_{\perp}}{I_{\parallel} + I_{\perp}} = Q\Sigma P_{\gamma}, \quad (3.19)$$

which, in ideal environment, would be equal to Σ . In reality, ϵ is attenuated, due to the photon beam's polarization degree P_{γ} and the polarization sensitivity Q , incorporating effects from finite target size and the finite solid angle covered by the detectors.

As the following chapter will further elaborate, polarized photons are typically produced via Compton-backscattering, which provides a quasi-monoenergetic beam. This means, that the range of energies of the photons is limited to a narrow band, in contrast to a continuous spectrum, like it is produced by bremsstrahlung. In regards to the aforementioned, the low background and high analyzing power allow a rather unambiguous assignment of parity quantum numbers. Moreover, the selective excitation of states only within the narrow energy range provides the opportunity to determine branching ratios. States observed outside this excitation range have to be populated via inelastic transitions and can be associated to a ground state transition by their energy. A branching ratio is then determined by the relative intensity.

If the inelastic transition of the first excited state (for even-even nuclei most often $J^{\pi} = 2^{+}$) to the ground state is observed, it is possible to obtain an average branching ratio. It may be argued, that sooner or later most of the inelastic transition funnel through the first excited state, resulting in an observed intensity of its decay $I_{2^{+}}$. The summed up intensity of the elastic transitions I_0 may be treated as if originating from one excited state. The average branching ratio for each energy range $\langle\beta\rangle$ follows:

$$\langle\beta\rangle = \frac{I_0}{I_0 + I_{2^{+}}} \quad (3.20)$$

These considerations may be further refined by the study of the decay behavior of states of a specific parity. An average branching ratio for all electric dipole states within an energy range $\langle\beta^{-}\rangle$ can be determined:

$$\langle\beta^{-}\rangle = \frac{I_0^{-}}{I_0^{-} + \frac{2}{3}I_{2+}^{-}}. \quad (3.21)$$

Here, the intensity of ground state transition of only electric dipole states N_0^{-} is summed up and the decay of the first excited state N_{2+}^{-} is considered as it is only fed by inelastic decay of those states. N_{2+}^{-} results from the decomposition of N_{2+} :

$$I_{2+}^{-} = I_{2+} \cdot \left(\frac{3}{2}\epsilon_{2+} + \frac{1}{2} \right), \quad (3.22)$$

with the azimuthal asymmetry of the first excited state ϵ_{2+} .

The average branching ratios may offer a good approximation of the ratio of the strength, which is not observed in ground state transitions, especially if no inelastic transition is observed other than the ground state transition of the first excited state, fed from higher lying states. The missing strength may be added back in order to discuss global properties of the nuclei.

4. Experimental setup

The experiments of this work were conducted at two major research facilities for NRF: On the one hand, at the superconducting Darmstadt linear accelerator (S-DALINAC) [42] at the Institut für Kernphysik of the Technische Universität Darmstadt in Germany. On the other hand, at the High-Intensity γ -ray Source (HI γ S) facility [43] of the Duke Free Electron Laser Laboratory at the Triangle Universities Nuclear Laboratory (TUNL), located in North Carolina, USA. The details of these facilities and the setups used for the NRF experiments will be presented in the following sections.

4.1. S-DALINAC

The S-DALINAC is a recirculating linear electron accelerator using superconducting acceleration elements. A schematic overview of the accelerator is given in Figure 4.1. Here, the electrons are produced by a thermionic gun and pre-accelerated to 250 keV. In the following normal-conducting part the beam is prepared with a chopper and pre-buncher, which imprint a 3 GHz frequency. The superconducting acceleration structures house niobium cavities with up to 20 cells each. The cavities are cooled to 2 K by liquid helium. After the injector, the beam can be either brought to the Darmstadt High-Intensity Photon Setup (DHIPS) with a beam energy of up to 10 MeV or

bend to the main accelerator. With its recent upgrade, the S-DALINAC is designed to provide electron beams with up to 130 MeV for further experimental sides: a low-energy photon-tagger (NEPTUN), an electron spectrometer with quadrupole-dipole magnet arrangement (Q-Clam) and a high-resolution electron spectrometer (LINTOTT).

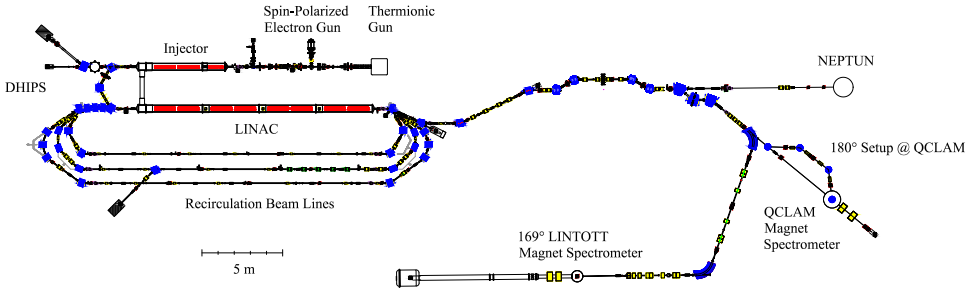


Figure 4.1.: Schematic of the S-DALINAC: After passing the injector, the beam can be used at DHIPS for NRF or photo-fission experiments or can be further accelerated in the main linac and then be passed on to NEPTUN or the electron-spectrometers. Figure taken from Ref. [42]

4.2. DHIPS

Parts of the NRF experiments described in this work were performed at DHIPS [44], which is illustrated schematically in Figure 4.2. Here, the electron beam provided by the injector of the S-DALINAC is stopped in a gold or copper radiator target in order to generate high-intensity bremsstrahlung. The continuous bremsstrahlung spectrum is filtered by an aluminum beam hardener, which suppresses background by attenuating low-energy photon. The remaining photons are collimated onto the target by a copper collimator. The radiation

emitted by the target through the means of NRF is detected by three high-purity germanium (HPGe) detectors. These detectors are encased in eight bismuth germanium oxide scintillator (BGO) detectors each, which themselves are shielded from the target by lead. The setup allows for further reduction of background from Compton-scattering and pair-production via anti-coincidence between HPGe detector and corresponding BGO shield. In order to reduce low-energy background from the target, slices made out of copper and lead called filters are placed in front of the HPGe detectors. These detectors have 100% relative efficiency compared to a 3"×3" NaI detector and are positioned at 90°, 95° and 130° with respect to the incident γ -beam.

The detection of emitted γ -radiation at these angles facilitates the determination of spin quantum number of excited states, as described in Section 3.2.

Due to the continuous spectrum of the bremsstrahlung, photons of all energies up to endpoint energy are available and simultaneously excite states in this energy range. Thus, a simultaneous measurement of each excited state's cross section is possible through the consecutive γ -decays. These measurements are done relative to a calibration standard. The isotope ^{11}B is most commonly used. Two containers of ^{11}B are stacked around the target of interest. A second measurement at lower energies is conducted to identify inelastic transitions by comparison. In addition, DHIPS provides the opportunity to perform relative self-absorption experiments as covered in Ref. [46].

4.3. HI γ S

The High-Intensity γ -ray Source is composed of mainly three parts. The first part is an electron linear accelerator, which provides a pulsed beam with energies of 180-280 MeV. The electrons are then further accelerated in a booster

synchrotron up to energies of 1.2 GeV and led to the race-track shaped storage ring. On the straight section of the storage ring, the electron bunches are forced on oscillating trajectory by alternating magnetic fields in the so-called wigglers. Due to the oscillation of the charged particles synchrotron radiation is emitted, which is called a free-electron laser (FEL). Since this laser system is not limited by the discrete energies like a conventional laser, this FEL can be continuously tuned to wavelengths of 190-1064 nm. The light is reflected back towards the oncoming electron bunch. Scattering off of these bunches via Compton-scattering, the photons are boosted to γ -ray energies of up to 100 MeV. During this process, the initial polarization of the FEL is conserved and thus collimating these photons produces a quasi-monoenergetic γ -ray beam with a polarization degree P_γ exceeding 99% [47]. Linear and circular polarized beams may be realized, using various wiggler setups.

4.4. γ^3 -setup

For the experiments covered in this work, a linear polarized γ -ray beam was produced. Up to two setups can be used simultaneously, allowing the conduction of two NRF measurements at the same time. Both setups together are called γ^3 -setup in a broader sense. In the more narrower sense, the first part, positioned upstream, is the γ^3 -setup described in Ref. [48]. Here, the combined usage of HPGe detectors and lanthanum bromide scintillator (LaBr) detectors, which yield higher efficiency, enable γ -ray coincidences measurements, that is ($\gamma, \gamma'\gamma''$) experiments, hence the name γ^3 . For the placement of both, HPGe and LaBr detectors following combinations of polar angle θ and azimuthal angle ϕ are available: For $\theta = 90^\circ$, detectors may be placed at $\phi = 0^\circ, 90^\circ, 180^\circ$ and 270° ; for backwards angle $\theta = 135^\circ$ at $\phi = 45^\circ, 135^\circ, 225^\circ$ and 315° . Figure 4.4 illustrates a typical arrangement and combination of detectors.

The second part, positioned downstream from γ^3 is referred to as polarimetry-setup. This setup simultaneously utilizes the polarized photon beam, since most photons traverse the target material placed in γ^3 without interaction. Up to four HPGe detectors are positioned at polarimetry-setup at $\theta = 90^\circ$, mirroring the equivalent detector plane from γ^3 . The detectors are numbered as follows: detector 6 is positioned at $\phi = 0^\circ$, viewing in the direction of the beam to the right. Continuing in positive mathematical sense of rotation, detector 7 is at $\phi = 90^\circ$, detector 8 at $\phi = 180^\circ$ and detector 9 at $\phi = 270^\circ$.

The simultaneous operation of γ^3 and the polarimetry-setup has little to no effect on the excitation within the energy range of the mono-chromatic beam. However, background at lower energies originating from Compton-scattering is increased at the polarimetry-setup compared to γ^3 , due to the additional components in and near the beam upstream. Hence, studies focusing on inelastic transitions are best performed at γ^3 , also taking advantage of the detector configuration for coincidences, while elastic transition and resulting parity assignments may be studied at the polarimetry-setup just as well.

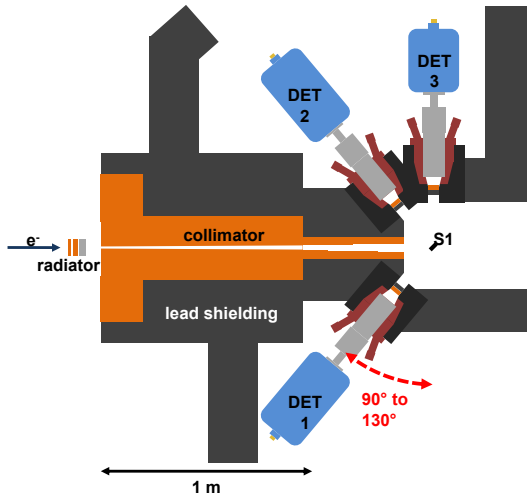


Figure 4.2.: Schematic of DHIPS: This setup is used for NRF experiments. Electrons are provided by the S-DALINAC and produce bremsstrahlung at the radiator, which illuminates the target at $S1$. Detector 2 and 3 are positioned such, that the setup is sensitive to spin quantum numbers of excited states (compare Figure 3.2). Detector 1 can be placed at various angles and was placed at 95° for the experiments in this work. Image provided by [45] and modified.

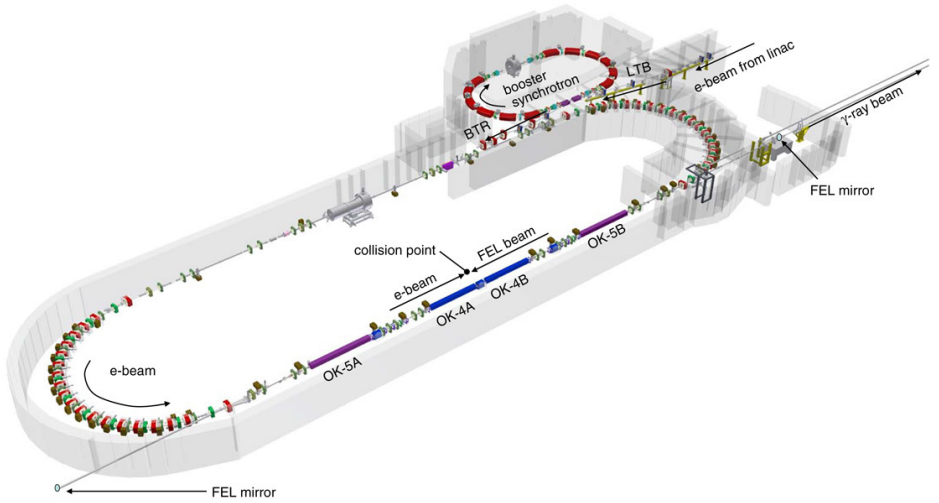


Figure 4.3.: Schematic of HI γ S: Electrons provided by the linac are boosted and then cycle in the storage ring, where the Compton-boosted γ -ray beam is produced from the FEL. Figure taken from Ref. [43].

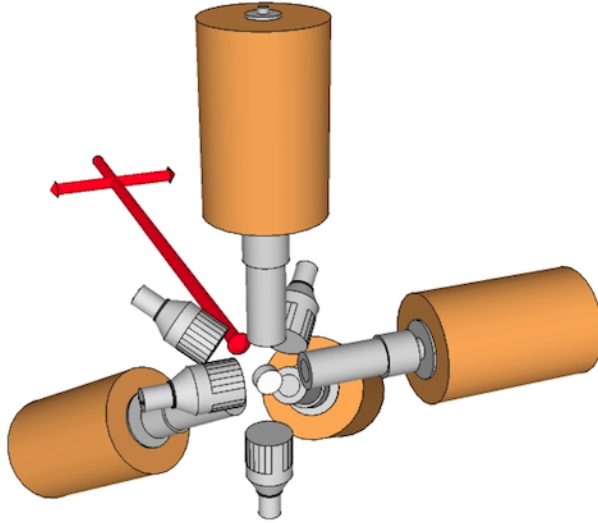


Figure 4.4.: Schematic of the γ^3 -setup: A typical arrangement of HPGe detectors (with orange dewars) and LaBr detectors (with striated encasement) is shown. The red beam marks the photon beam and its polarization plane. The beam points to the target (white cylinder). The detector in the foreground are positioned at $\theta = 90^\circ$, in the plane orthogonal to the beam. The background positions are those at $\theta = 135^\circ$.

4.5. Experimental details

The experiments were conducted in very similar fashion, specifically to ensure comparability. The isotopic enriched target material was bound in Cr_2O_3 and was contained in the form of compressed powder in containers made of polyvinyl chloride. The following tables will list the experimental details varying between the three isotopes.

Table 4.1.: Experimental details of the DHIPS campaign. If two values are given, the upper one is associated to the measurement with higher endpoint energy of the electron beam E_e . Otherwise, the single value is valid for both.

| specification | ^{50}Cr | ^{52}Cr | ^{54}Cr |
|---------------------------------|-----------------------|-----------------------------|-----------------------|
| campaign date | 2014 | 2004 | 2014 |
| E_e (MeV) | 9.7 | 9.9 | 9.7 |
| | 7.5 | 8.0 | 7.5 |
| target mass (mg) | 1988.0(1) | 996.4(5) 2954(1) | 1475.0(1) |
| degree of enrichment (%) | 96.416(20) | 99.8 83.789 ^a | 95.58(5) |
| ^{11}B mass (mg) | 191.8(1) +207.5(1) | 1004.1(5) | 191.8(1) +207.5(1) |
| measuring time ^b (h) | 132 | 62 | 125 |
| | 93 | 23 | 103 |

^a non-enriched chromium, yielding this natural abundance

^b rounded to next full hour

Table 4.2.: Experimental details of the HI γ S campaign.

| specification | ^{50}Cr | ^{52}Cr | ^{54}Cr |
|--------------------------|------------------|------------------|------------------|
| campaign | 2014/2015 | 2014/2015 | 2014/2015 |
| target position | polarimetry | γ^3 | polarimetry |
| target mass (mg) | 1988.0 (1) | 1317.5 (27) | 1475.0 (1) |
| degree of enrichment (%) | 96.416 (20) | 99.54 (20) | 95.58 (5) |

At both facilities the detector signals were fed to spectrum amplifiers and consequently to analog-to-digital converters, resulting in histograms with 16384 channels.

5. Analysis

In this chapter, the analysis of the recorded spectra is presented. The access to the observables listed in Chapter 3 is demonstrated for the example of the experiment on ^{54}Cr . The analysis of the experiments on ^{50}Cr and ^{52}Cr followed the same procedure, but was done by Dr. Haridas Pai. Shortened accounts for this process were given in publications leading up to this work [49, 50, 51].

During the measurements performed at DHIPS, the energy resolution of detector 1 was noticeable worse than that of detector 2 and 3. This is demonstrated in Table 5.1, where the values for the full width at half maximum (FWHM) of the fitted peaks of the calibration target ^{11}B are listed, as well as in Figure 5.1, where this is visualized for the high statistic yielding peaks of ^{11}B at 4444.98(7) keV [52] and ^{12}C at 4439.82(21) keV [53]. Data and spectrum are taken from the measurement of ^{54}Cr with 9.7 MeV endpoint energy.

Because of the inferior performance, spectra of detector 1 was used for qualitative analysis only.

5.1. Energy calibration

The first step necessary for the analysis of the recorded histograms is an energy calibration. The correlation of channel number to energy is done using

Table 5.1.: Energy resolution at DHIPS: Listed are the FWHMs in keV for the well-known and isolated peaks of the calibration target ^{11}B at 2125, 5020 and 8911 keV.

| peaks detector | 2125 keV | 5020 keV | 8911 keV |
|-------------------|----------|----------|----------|
| Det 1 | 5.44 | 8.27 | 9.69 |
| Det 2 | 4.28 | 5.94 | 8.08 |
| Det 3 | 4.12 | 6.39 | 8.46 |

the well-known and recognizable peaks produced by the calibration standard ^{11}B mentioned above. This nucleus is particularly suited, as it provides lines of high intensity over a wide energy range. This allows for robust interpolation and extrapolation using polynomials up to third order. Since the ^{11}B is kept within the target during the hole run time of the experiments at DHIPS, it is possible to partition the histograms and correct for potential shifts in the energy calibration.

The energy calibration for the experiments at $\text{HI}\gamma\text{S}$ is performed using background lines of ^{40}Ar at 1460.820(5) keV [54] and ^{208}Pb at 2614.511(10) keV [55], as well as transitions of the nucleus of interest observed at DHIPS.

5.2. Detector efficiency and photon number

The essential formula, which connects the peak areas fitted in the histogram to the integrated cross section $I_{i \rightarrow j}$ and all derived observables is given by:

$$A_{i \rightarrow j} = I_{i \rightarrow j} \cdot W_{0 \rightarrow i \rightarrow j} \cdot N_T \cdot \varepsilon(E_i) \cdot N_\gamma(E_i). \quad (5.1)$$

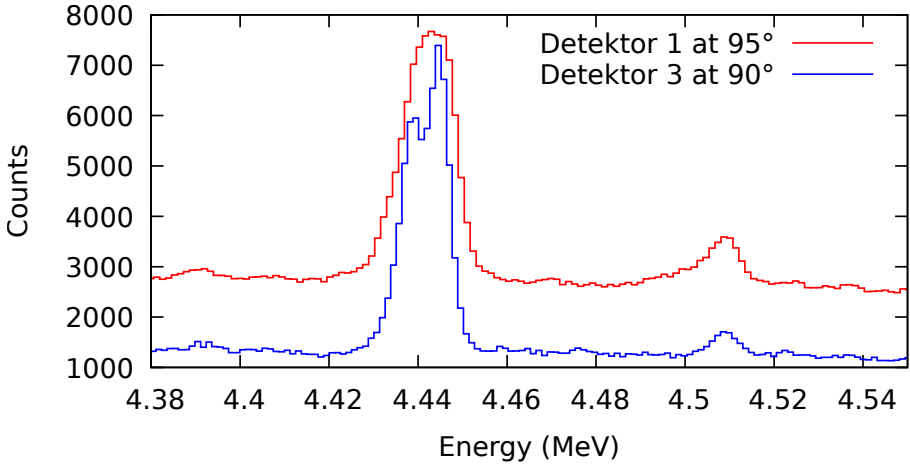


Figure 5.1.: Comparison of the energy resolutions of detector 1 and detector 3: This figure shows the spectra recorded at DHIPS with the aforementioned detectors. The eminent discrepancy in resolving power is demonstrated for the peaks of ^{11}B at 4444.98(7) keV and ^{12}C at 4439.82(81) keV.

Here, the peak area fitted in the histogram, in other words, the number of recorded events associated with the transition from state i to state j , is given by $A_{i \rightarrow j}$. $I_{i \rightarrow j}$ and $W_{0 \rightarrow i \rightarrow j}$ are defined as in Chapter 3. N_T gives the number of target nuclei, which is determined by the targets mass. The remaining factors $\varepsilon(E_i)$ and $N_\gamma(E_i)$ are the detector efficiency and the number of incident photons, respectively. These quantities are in general unknown and have to be determined via the measurement of the calibration standard. In particular, both are energy dependent and may vary for each experiment through several external factors such as detector high voltage supply, filter thickness, energy of the electron beam or radiator thickness and material.

The term $\varepsilon(E_i) \cdot N_\gamma(E_i)$ is determined for transitions of the calibration standard, for which all other components of Equation (5.1) are known, yielding results for the corresponding transition energies. These are interpolated and extrapolated throughout the experimental energy range. Considering that, the behavior of detector efficiency and incident photon number has to be determined.

5.2.1. Efficiency calibration

In order to examine the detector efficiency separately, a source measurement is performed. Here, a ^{56}Co source provides photons with energies up to 3.5 MeV. Considering known relative intensities, the relative detector efficiencies are obtained. A complementary simulation of the detector efficiency using the monte-carlo tool GEANT4 [56] extends these results to higher energies. Both in combination are fitted with the empirical function [57]

$$\log \varepsilon = \sum_{i=1}^4 a_i \cdot \left(\log \frac{E}{E_0} \right)^{i-1}. \quad (5.2)$$

This is shown in Figure 5.2. The uncertainty of the scaling factor of the fit to the source measurement is considered as uncertainty of the relative efficiency.

5.2.2. Photon flux calibration

With the efficiency calibration extrapolated and known relative intensities of the transitions of ^{11}B , it is possible to determine the relative photon flux at the corresponding energies. These values are interpolated with a parametrization of Schiffs formular [58]. This is shown in Figure 5.3

Although, absolute values for detector efficiency (and consequently photon flux) may be determined, provided the activity of the source and the geometry of the setup are known, the relative values suffice to extract the relevant observables.

5.2.3. Parity and spin quantum numbers

Parity and spin quantum numbers are assigned according to the azimuthal asymmetry ϵ measured at HI γ S and the ratio of polar angular distribution w measured at DHIPS, respectively. Here the parity quantum number corresponds to the sign of ϵ , the case is not as clear cut for the spin quantum number. In this work, the criteria, used in order to assign either spin 1 or 2, is, whether w is closer to 0.71 or 2.26 in terms of standard deviations.

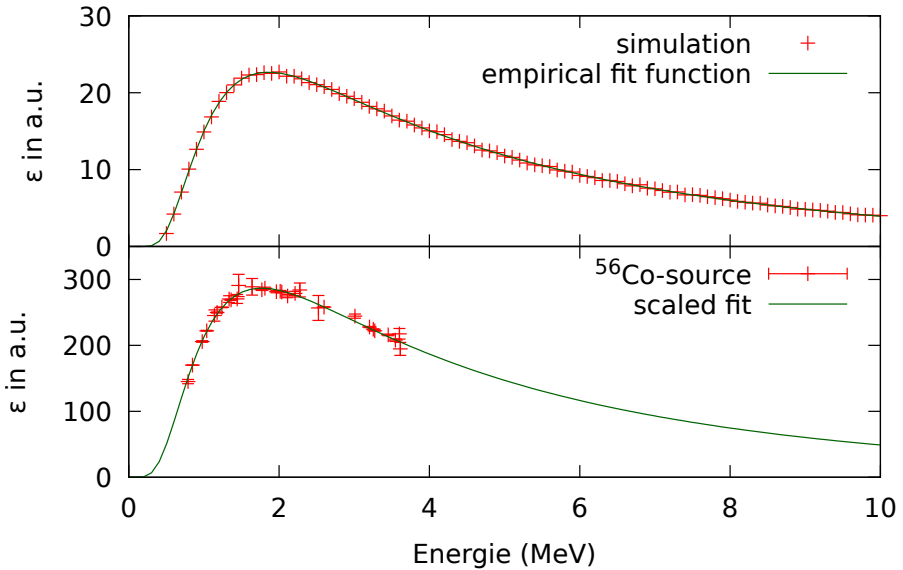


Figure 5.2.: Detector efficiency: The detector efficiency is simulated for several energies and fitted with Equation (5.2) (top panel). Scaled to and verified by the source measurement, the behavior of the detector efficiency is determined for the full experimental range (bottom panel). The results for detector 2 at $\theta = 130^\circ$ are shown.

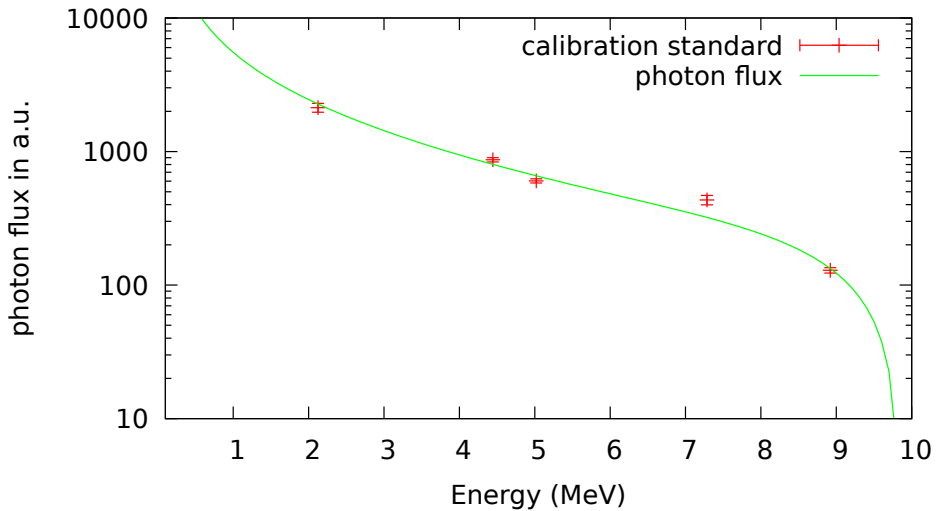


Figure 5.3.: Photon flux calibration: The results for detector 2 at $\theta = 130^\circ$ are shown. The data points in red are given via the known integrated cross sections of the calibration standard. A parametrization of the Schiff formular is fitted to the data points.



6. Results

The results of the analysis, as described above, are presented in this chapter. In the first section revised data and newly determined average branching ratios for the nucleus ^{50}Cr is shown. The second part will depict and list results for ^{54}Cr .

6.1. Results for ^{50}Cr

Results for ^{50}Cr obtained from the NRF campaigns in 2014 and 2015 have been published previously; with regards to the interpretation of the magnetic dipole strength in Ref. [50] and the electric dipole strength in Ref. [51]. Only revised and newly analyzed data will be presented in this section.

6.1.1. Revised transition strength

Since the first publication of the results in the aforementioned publications, they have been revised within the present work. A wrong target mass was previously used in the determination of the cross sections. The real target mass is 0.6 % lower than assumed previously. This issue leaves the determination of spin and parity quantum number unchanged, but affects the integrated cross

section and all derived quantities. The revised results are shown in Table 6.1.

Table 6.1.: Revised results for ^{50}Cr : Given are the excitation energies E_i , spin and parity quantum numbers J^π , integrated cross sections $I_{i,0}$ and the ground state transition strengths $B(E1) \uparrow$ and $B(M1) \uparrow$

| E_i in keV | J^π | $I_{i,0}$ in eV fm ² | $B(E1) \uparrow$ in $10^{-3}e^2 \text{fm}^2$ | $B(M1) \uparrow$ in $10^{-3}\mu_N^2$ |
|-----------------|-----------------------------|------------------------------------|---|---|
| 3628(1) | 1 ⁺ ^a | 121(5) | - | 1120(49) |
| 4997(1) | 1 ⁺ ^b | 16.3(12) | - | 146(15) |
| 5931(1) | 1 ⁺ | 24.0(20) | - | 92(7) |
| 6313(1) | 1 ⁻ | 1.15(15) | 0.16(2) | - |
| 6504(1) | 1 ⁻ | 8.3(11) | 1.11(15) | - |
| 6898(1) | 1 ⁻ | 4.18(71) | 0.52(9) | - |
| 6932(1) | 1 ⁻ | 13.16(77) | 1.65(10) | - |
| 7104(1) | 1 ⁻ | 10.38(68) | 1.27(8) | - |
| 7601(1) | 1 ⁺ | 66.8(73) | - | 198(22) |
| 7646(1) | 1 ⁺ | 23.3(28) | - | 68(8) |
| 7840(1) | 1 ⁻ | 1.86(38) | 0.21(4) | - |
| 7881(1) | 1 ⁻ | 6.90(56) | 0.76(6) | - |
| 7948(1) | 1 ⁺ | 198.9(97) | - | 718(41) |
| 8046(1) | 1 ⁺ | 42.5(47) | - | 119(13) |
| 8111(1) | 1 ⁻ | 21.5(13) | 2.94(20) | - |
| 8122(1) | 1 ⁺ | 16.5(20) | - | 45(5) |
| 8359(1) | 1 ⁻ | 4.22(61) | 0.44(6) | - |
| 8440(1) | 1 ⁻ | 8.16(72) | 0.85(7) | - |
| 8528(1) | 1 ⁺ | 97(11) | - | 355(48) |
| 8651(1) | 1 ⁻ | 12.29(97) | 1.24(10) | - |
| 8715(1) | 1 ⁻ | 10.02(84) | 1.49(14) | - |
| 8770(1) | 1 ⁻ | 3.80(53) | 0.64(10) | - |
| 8886(1) | 1 ⁺ | 78.2(68) | - | 198(17) |

| E_i in keV | J^π | $I_{i,0}$ in eV fm ² | $B(E1) \uparrow$ in $10^{-3} e^2 \text{fm}^2$ | $B(M1) \uparrow$ in $10^{-3} \mu_N^2$ |
|-----------------|----------------|------------------------------------|--|--|
| 8998(1) | 1 ⁻ | 4.02(56) | 0.39(5) | - |
| 9008(1) | 1 ⁺ | 40.7(48) | - | 102(12) |
| 9088(1) | 1 ⁻ | 10.4(17) | 1.00(17) | - |
| 9174(1) | 1 ⁻ | 4.8(10) | 0.46(10) | - |
| 9208(1) | 1 ⁺ | 50(12) | - | 124(30) |
| 9410(1) | 1 ⁺ | 106(17) | - | 254(41) |
| 9553(1) | 1 ⁻ | 10.9(13) | 0.99(12) | - |
| 9579(1) | 1 ⁺ | 37.9(78) | - | 90(18) |
| 9719(1) | 1 ⁺ | 174(21) | - | 404(49) |

^a From Ref. [59]

^b From Ref. [60]

Since the revised data differ by less than 1%, the interpretation of the photon scattering experiments given in the aforementioned publications are unaffected.

6.1.2. Average branching ratios

The average branching ratios of electric dipole states $\langle \beta^- \rangle$ in ⁵⁰Cr are plotted in Figure 6.1. The occasional extreme values close to $\langle \beta^- \rangle = 1$ and extreme uncertainties at lower energies result from low statistics. At higher energies, these fluctuations are mitigated, as more levels are excited within each energy setting and thus more decay channels through the first excited states are available.

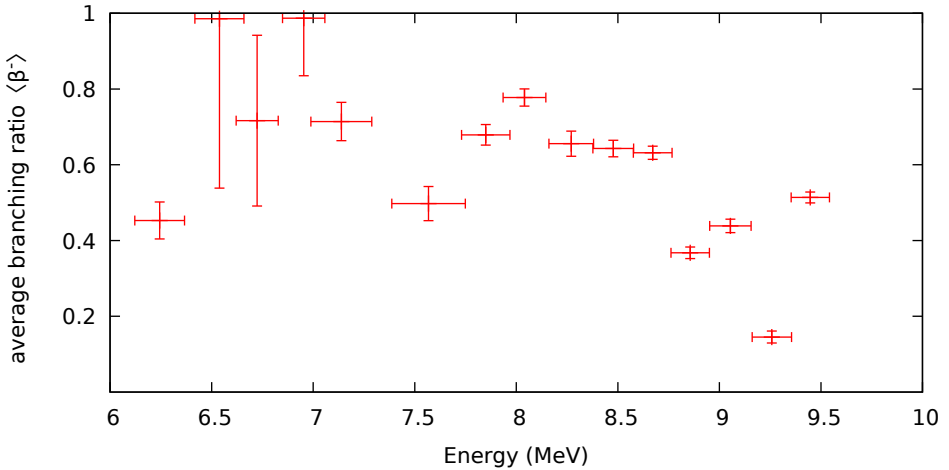


Figure 6.1.: Average branching ratios in ^{50}Cr : The energy intervals given with each data point mark the range of each experimental energy setting.

6.2. Results for ^{54}Cr

The results for ^{54}Cr are part of this work and have been published in [51]. In this work, 70 states have been observed, 58 for the first time. These states are distinguishable thanks to the high energy resolution of HPGe detectors, as can be seen in Figure 6.2, featuring the energy range of the SM, and the spectra given in Appendix A.1. All but one state listed have been observed with at least both fully operational detectors 1 and 2 at DHIPS and with at least one detector at HI γ S. At DHIPS, the excited state at 7411 keV was superimposed with background stemming from a neutron capture line in ^{70}Ge , a constituent of the detector material. This excited state was observed only in HI γ S measurements, where background is drastically reduced. In the following, the

results for each observable will be presented in greater detail.

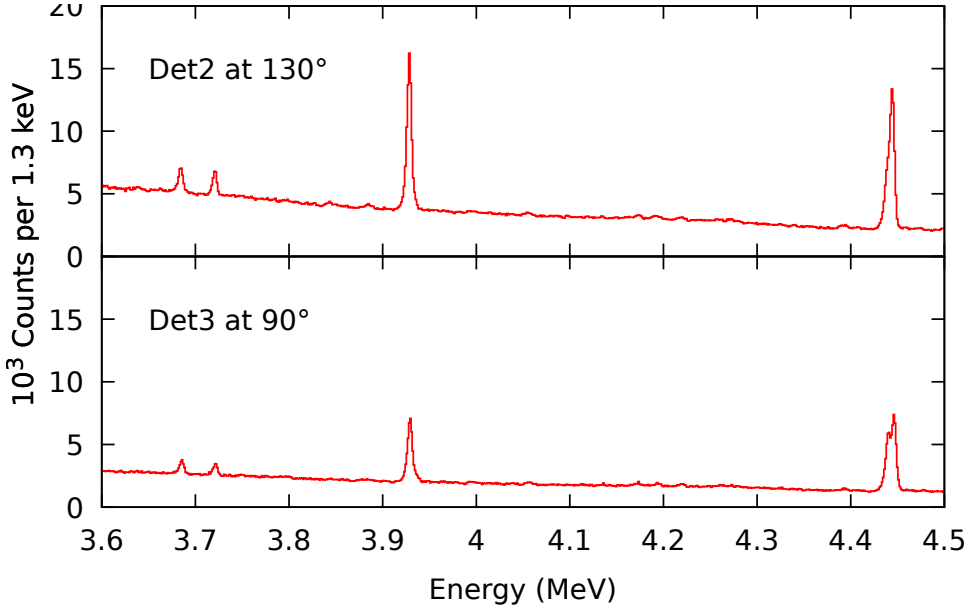


Figure 6.2.: Cutout of ^{54}Cr spectra: The spectrum of detector 2 at 130° is shown in red and detector 3 at 90° in green. The low-lying $J^\pi = 1^+$ states of the scissors mode at 3720(1) and 3927(1) keV as well as the doublet states in ^{12}C and ^{11}B at 4439.82(81) keV and 4444.98(7) keV are featured.

6.2.1. Parity quantum numbers

The results for the parity quantum numbers are shown in Figure 6.3. The experimental range was between 5.5 and 10 MeV. It was not possible to resolve the doublet at 8860(1) and 8866(2) keV in the parity measurement at

$HI\gamma S$, due to low statistics. Considering both states simultaneously, a value for the azimuthal asymmetry of $\epsilon = 0.75(23)$ was determined. It stands to reason, that both states have positive parity, but a conclusive result cannot be reached.

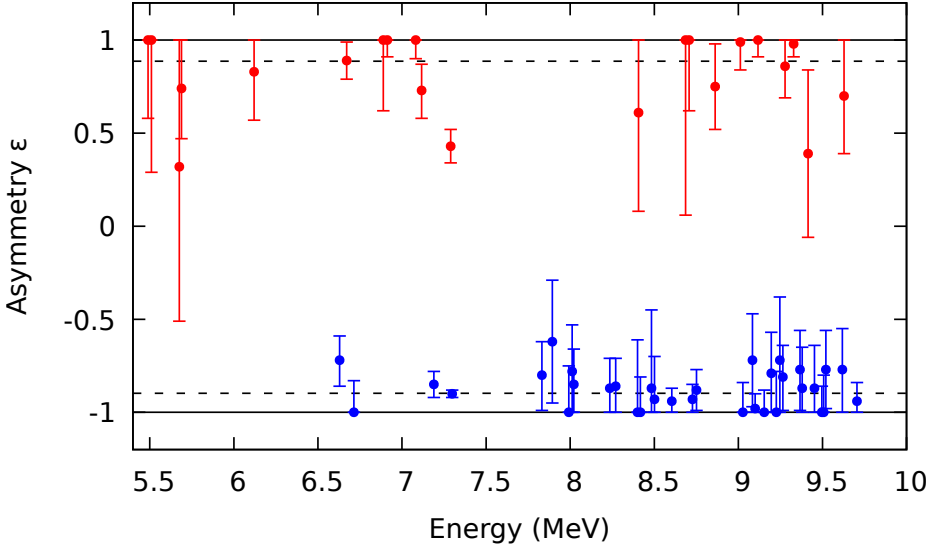


Figure 6.3.: Azimuthal asymmetry: The values of ϵ are plotted for the observed states in ^{54}Cr color-coded according to the parity assigned. Only the states within the experimental range of 5.4 MeV to 10 MeV are shown. States with positive parity plotted in red and states with negative parity in blue. Additionally, the dashed lines mark the weighted mean value of ϵ for the states of positive parity at 0.89 and of negative parity at -0.90. These values could be considered to represent the combination of polarization degree P and parity sensitivity Q .

6.2.2. Spin quantum numbers

The ratio of angular distributions w are visualized in Figure 6.4. The first excited state at 835(1) keV shows a ratio of $w = 0.99(4)$, only compatible with 1, an isotropic emission. This state is known to have $J^\pi = 2^+$. Nevertheless, this behavior is to be expected, due to the feeding from various higher states.

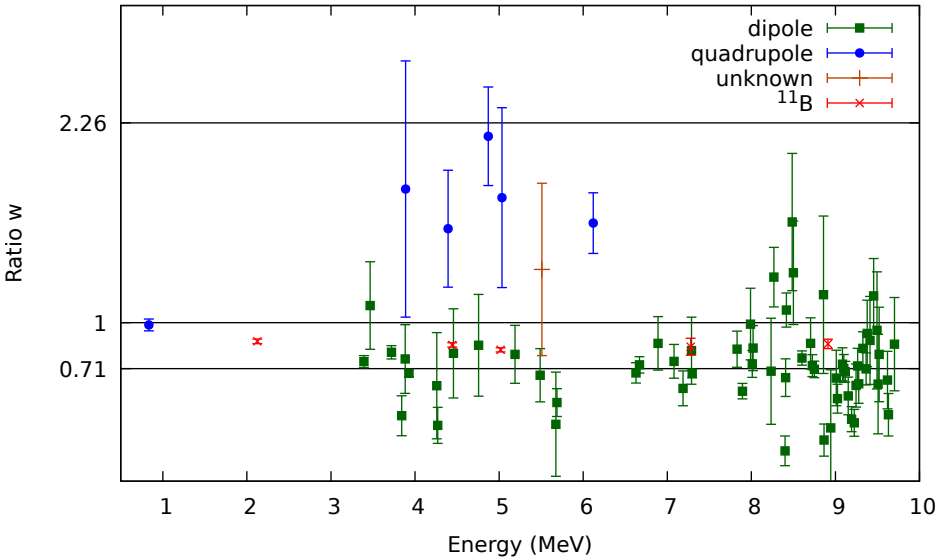


Figure 6.4.: Ratio of angular distribution: The values of w are plotted for the observed states in ^{54}Cr color-coded according to the spin assigned. Dipole states are shown in green, quadrupole states in blue and the states with unknown spin quantum number in orange. Additionally, the ratio is plotted for the excited states in ^{11}B .

The value $w = 1.33(54)$ was determined for the state at 5509(1) keV. Since

both ideal values of 0.71 or 2.26 are reached within two standard deviations but not within one, no conclusive spin assignment was possible. Similarly, the state at 8487(2) keV shows $w = 1.63(43)$, which is closer to 2.26. Nevertheless, the assignment as dipole state was done, due to its negative parity, which otherwise would imply a highly unlikely $M2$ transition.

Furthermore, a spin of $J = 1$ was observed for the states at 3393(1) and 3720(1) keV. Both were previously reported to have either $J = 1$ or $J = 2$ in Ref. [61]. The positive parity for 3393(1) keV and negative parity for 3720(1) keV will be adopted for the further interpretation, respectively.

The same reference lists a doublet of quadrupole states at 3925.55(7) and 3927.69(8), which can be traced back to only two sources, D.L. Watson et al. [62] and R. Chapman et al. [63], respectively. In the later publication, no spin quantum number is given. In the former, the spin quantum number is determined through a comparison with distorted-wave Born approximation calculations, but noting, "... that the fits to the shapes of the angular distributions are good except for the states at 3.927 and 4.637 MeV." [62]. Besides this, Watson et al. give references to a private communication with Chapman and Ref. [64], which does not state a spin quantum number. In contrast to those previous, rather vague reports, the results in this work suggest, that this doublet does not exist but a single dipole state is located at 3927(1) keV. Due to its excitation energy and transition strength, this state will be interpreted as the main fragment of the scissors mode with $J^\pi = 1^+$ in the following. The conclusive determination of the parity quantum number remains highly desired within this context.

Further discrepancies to Ref. [61] occur for the states at 4258(4) and 5190(6) keV. Both are reported be 2^+ -states in Ref. [65] but analyzed as dipole states here. The positive parity quantum number will be adopted for further interpretation.

The results for spin and parity quantum number are listed in Table 6.2.

6.2.3. Cross section

Similar to the case of ^{50}Cr , the data have been revised since. In this incidence, the real target mass is 1.67 % lower than assumed previously, that is 1488 mg instead of 1500 mg. The reevaluated results for integrated cross sections and transition strengths are tabulated in Table 6.3.

Table 6.2.: Quantum numbers ^{54}Cr : Given are the excitation energies E_i , the ratio of azimuthal angular distribution w , the polar asymmetry ϵ and the spin and parity quantum numbers J^π .

| E_i in keV | w | ϵ | J^π |
|-----------------|----------|------------|-----------------------------|
| 835(1) | 0.99(4) | - | 2 ⁺ ^a |
| 3393(1) | 0.75(4) | - | 1 ⁻ ^b |
| 3465(1) | 1.11(28) | - | 1 |
| 3720(1) | 0.81(4) | - | 1 ⁺ ^b |
| 3842(1) | 0.41(13) | - | 1 |
| 3883(1) | 0.77(22) | - | 1 |
| 3888(2) | 1.84(81) | - | 2 ⁺ |
| 3927(1) | 0.68(2) | - | 1 ⁺ |
| 4258(4) | 0.60(33) | - | 1 ⁺ ^b |
| 4270(1) | 0.35(11) | - | 1 |
| 4394(1) | 1.59(37) | - | 2 ⁺ |
| 4458(2) | 0.81(28) | - | 1 ⁺ ^b |
| 4757(1) | 0.86(32) | - | 1 |
| 4872(1) | 2.18(31) | - | 2 ⁺ ^b |
| 5034(2) | 1.79(57) | - | 2 ⁺ |
| 5190(6) | 0.80(18) | - | 1 ⁺ ^b |
| 5489(2) | 0.67(17) | 1.00(42) | 1 ⁺ |
| 5509(1) | 1.34(54) | 1.00(71) | ? ⁺ |
| 5676(2) | 0.36(33) | 0.32(83) | 1 ⁺ |
| 5688(1) | 0.50(9) | 0.74(27) | 1 ⁺ |
| 6120(1) | 1.63(19) | 0.83(26) | 2 ⁺ |
| 6629(1) | 0.68(6) | -0.72(14) | 1 ⁻ |
| 6671(1) | 0.73(5) | 0.89(10) | 1 ⁺ |
| 6891(1) | 0.87(17) | 1.00(38) | 1 ⁺ |

| E_i in keV | w | ϵ | J^π |
|-----------------|----------|-----------------------|----------------|
| 7082(1) | 0.76(11) | -1.00(19) | 1 ⁻ |
| 7189(1) | 0.59(11) | -0.85(7) | 1 ⁻ |
| 7289(1) | 0.82(21) | 0.43(9) | 1 ⁻ |
| 7298(1) | 0.68(3) | -0.90(2) | 1 ⁻ |
| 7413(1) | - | -0.74(23) | 1 ⁻ |
| 7832(1) | 0.83(11) | -0.80(19) | 1 ⁻ |
| 7895(1) | 0.57(5) | -0.62(33) | 1 ⁻ |
| 7992(1) | 0.99(23) | -1.00(25) | 1 ⁻ |
| 8013(1) | 0.74(8) | -0.78(25) | 1 ⁻ |
| 8023(1) | 0.84(14) | -0.85(19) | 1 ⁻ |
| 8236(2) | 0.69(33) | -0.87(16) | 1 ⁻ |
| 8271(1) | 1.29(19) | -0.86(15) | 1 ⁻ |
| 8403(1) | 0.19(9) | -1.00(39) | 1 ⁻ |
| 8409(1) | 0.65(12) | 0.61(53) | 1 ⁺ |
| 8419(1) | 1.08(11) | -1.00(19) | 1 ⁻ |
| 8488(2) | 1.63(43) | -0.87(41) | 1 ⁻ |
| 8503(1) | 1.31(33) | -0.93(24) | 1 ⁻ |
| 8605(1) | 0.78(5) | -0.94(7) | 1 ⁻ |
| 8707(1) | 0.87(16) | 1.00(38) | 1 ⁺ |
| 8728(1) | 0.73(7) | -0.93(8) | 1 ⁻ |
| 8751(1) | 0.71(5) | -0.88(11) | 1 ⁻ |
| 8860(1) | 1.18(50) | 0.75(23) ^c | 1 ⁺ |
| 8866(2) | 0.26(10) | 0.75(23) ^c | 1 ⁺ |
| 8947(2) | 0.34(37) | -0.72(32) | 1 ⁻ |
| 9012(1) | 0.65(18) | 0.99(14) | 1 ⁺ |
| 9027(1) | 0.52(9) | -1.00(16) | 1 ⁻ |
| 9086(1) | 0.74(10) | -0.72(25) | 1 ⁻ |
| 9101(1) | 0.71(9) | -0.98(8) | 1 ⁻ |

| E_i in keV | w | ϵ | J^π |
|-----------------|----------|------------|----------------|
| 9119(1) | 0.69(7) | 1.00(9) | 1 ⁺ |
| 9154(1) | 0.54(12) | -1.00(12) | 1 ⁻ |
| 9195(1) | 0.39(8) | -0.79(22) | 1 ⁻ |
| 9226(1) | 0.37(8) | -1.00(22) | 1 ⁻ |
| 9247(1) | 0.60(14) | -0.72(34) | 1 ⁻ |
| 9266(1) | 0.73(11) | -0.81(18) | 1 ⁻ |
| 9279(1) | 0.61(12) | 0.86(17) | 1 ⁺ |
| 9330(1) | 0.84(10) | 0.98(6) | 1 ⁺ |
| 9367(2) | 0.71(10) | -0.77(22) | 1 ⁻ |
| 9380(1) | 0.93(21) | -0.87(21) | 1 ⁻ |
| 9413(1) | 0.89(28) | 0.39(45) | 1 ⁺ |
| 9457(2) | 1.17(24) | -0.87(22) | 1 ⁻ |
| 9497(3) | 0.95(37) | -1.00(14) | 1 ⁻ |
| 9509(1) | 0.61(31) | -1.00(20) | 1 ⁻ |
| 9522(1) | 0.80(30) | -0.77(21) | 1 ⁻ |
| 9622(1) | 0.64(18) | -0.77(22) | 1 ⁻ |
| 9633(2) | 0.42(13) | 0.70(31) | 1 ⁺ |
| 9705(4) | 0.86(29) | -0.94(10) | 1 ⁻ |

^a taken from Ref. [61]

^b parity quantum number adopted from Ref. [61]

^c doublet not resolvable at HI γ S

Table 6.3.: Transition strength of ^{54}Cr : Given in this table are the excitation energies E_i , the transition width Γ_0 , branching ratio $\frac{\Gamma_0}{\Gamma}$ and the transition strengths $B(E1)$, $B(E2)$ or $B(M1)$ according to the known or adopted J^π .

| E_i in keV | Γ_0 in meV | $\frac{\Gamma_0}{\Gamma}$ | $B(E1) \uparrow$ in $10^{-3}e^2 \text{ fm}^2$ | $B(E2) \uparrow$ in $e^2 \text{ fm}^4$ | $B(M1) \uparrow$ in $10^{-3}\mu_N^2$ |
|-----------------|----------------------|---------------------------|--|---|---|
| 835(1) | 6.14(25) | - | - | $942(38) \cdot 10^2$ | - |
| 3393(1) | 20.0(11) | - | 1.461(82) | - | - |
| 3465(1) | 2.96(54) | - | 0.204(37) | - | 18.5(34) |
| 3720(1) | 26.3(13) | - | - | - | 132.3(65) |
| 3842(1) | 6.55(77) | - | 0.33(4) | - | 30.0(35) |
| 3883(1) | 5.5(11) | - | 0.27(5) | - | 24(5) |
| 3888(2) | 3.1(12) | - | - | 21.5(87) | - |
| 3927(1) | 236.4(90) | - | - | - | 1012(38) |
| 4258(4) | 13.6(95) | - | 0.50(35) | - | 46(32) |
| 4270(1) | 29.8(86) | - | 1.1(3) | - | 99(29) |
| 4394(1) | 7.8(13) | - | - | 29.7(61) | - |
| 4458(2) | 2.1(18) | - | - | - | 6.0(53) |
| 4757(1) | 6.2(16) | - | 0.17(4) | - | 15(4) |
| 4872(1) | 10.3(29) | - | - | 23.3(67) | - |
| 5034(2) | 6.5(17) | - | - | 12.6(33) | - |
| 5190(6) | 22.5(12) | - | - | - | 41.7(45) |
| 5489(2) | 23.3(33) | - | - | - | 36.5(51) |
| 5509(1) | 32.4(84) | - | 0.18(5) | - | 17(4) |
| 5676(2) | 11.3(25) | - | - | - | 15.9(35) |

| E_i in keV | Γ_0 in meV | $\frac{\Gamma_0}{T}$ | $B(E1) \uparrow$ in $10^{-3}e^2 \text{ fm}^2$ | $B(E2) \uparrow$ in $e^2 \text{ fm}^4$ | $B(M1) \uparrow$ in $10^{-3}\mu_N^2$ |
|-----------------|------------------------|----------------------|--|---|---|
| 5688(1) | 76.4(80) | 0.74(13) | - | - | 108(11) |
| 6120(1) | 79.1(73) | - | - | 57.4(53) | - |
| 6629(1) | 578(57) | 0.889(76) | 5.69(57) | - | - |
| 6671(1) | 264(13) | - | - | - | 231(11) |
| 6891(1) | 85.4(74) | - | - | - | 67.7(58) |
| 7082(1) | 126.4(99) | - | 1.02(8) | - | - |
| 7189(1) | 925(38) | - | 7.14(29) | - | - |
| 7289(1) | 223(23) | - | 1.65(17) | - | - |
| 7298(1) | 1763(70) | 0.077(10) | 13.0(5) | - | - |
| 7413(1) | 130(29) | - | 0.92(20) | - | - |
| 7832(1) | 486(22) | - | 2.90(13) | - | - |
| 7895(1) | 546(33) | 0.480(45) | 3.18(19) | - | - |
| 7992(1) | 150(14) | - | 0.85(8) | - | - |
| 8013(1) | 664(68) | 0.46(12) | 3.70(38) | - | - |
| 8023(1) | 791(40) | - | 4.39(22) | - | - |
| 8236(2) | 474(33) | - | 2.43(17) | - | - |
| 8271(1) | 608(47) | 0.115(32) | 3.08(24) | - | - |
| 8403(1) | 336(68) | - | 1.62(33) | - | - |
| 8409(1) | 91(16)·10 ¹ | 0.91(21) | - | - | 396(70) |
| 8419(1) | 354(26) | - | 1.70(13) | - | - |
| 8488(2) | 99(20) | 0.74(22) | 0.463(95) | - | - |
| 8503(1) | 114(20) | - | 0.532(95) | - | - |
| 8605(1) | 2509(96) | - | 11.29(43) | - | - |
| 8707(1) | 248(26) | - | - | - | 97(10) |

| E_i in keV | Γ_0 in meV | $\frac{\Gamma_0}{\Gamma}$ | $B(E1) \uparrow$ in $10^{-3}e^2 \text{ fm}^2$ | $B(E2) \uparrow$ in $e^2 \text{ fm}^4$ | $B(M1) \uparrow$ in $10^{-3}\mu_N^2$ |
|-----------------|-------------------------|---------------------------|--|---|---|
| 8728(1) | 1042(55) | - | 4.49(24) | - | - |
| 8751(1) | 275(14)·10 ¹ | 0.087(26) | 11.76(59) | - | - |
| 8860(1) | 197(73) | - | - | - | 74(27) |
| 8866(2) | 435(87) | - | - | - | 162(32) |
| 8947(2) | 99(28) | - | 0.40(11) | - | - |
| 9012(1) | 436(98) | - | - | - | 154(35) |
| 9027(1) | 717(60) | 0.227(51) | 2.80(23) | - | - |
| 9086(1) | 850(75) | 0.336(64) | 3.25(29) | - | - |
| 9101(1) | 755(49) | - | 2.87(19) | - | - |
| 9119(1) | 1419(74) | 0.212(15) | - | - | 485(25) |
| 9154(1) | 670(87) | 0.47(11) | 2.50(32) | - | - |
| 9195(1) | 826(76) | 0.244(70) | 3.08(28) | - | - |
| 9226(1) | 694(77) | 0.100(87) | 2.53(28) | - | - |
| 9247(1) | 971(88) | 0.301(57) | 3.52(32) | - | - |
| 9266(1) | 1684(82) | - | 6.07(30) | - | - |
| 9279(1) | 1006(63) | - | - | - | 327(21) |
| 9330(1) | 2387(107) | - | - | - | 762(34) |
| 9367(2) | 1120(119) | 0.313(91) | 3.91(41) | - | - |
| 9380(1) | 823(153) | 1.21(26) | 2.86(53) | - | - |
| 9413(1) | 75(20)·10 ¹ | 0.77(27) | - | - | 234(61) |
| 9457(2) | 598(63) | - | 2.03(21) | - | - |
| 9497(3) | 170(71)·10 ¹ | 1.20(46) | 5.7(24) | - | - |
| 9509(1) | 105(51)·10 ¹ | - | 3.5(17) | - | - |
| 9522(1) | 59(19)·10 ¹ | - | 1.96(63) | - | - |

| E_i in keV | Γ_0 in meV | $\frac{\Gamma_0}{\Gamma}$ | $B(E1) \uparrow$ in $10^{-3} e^2 \text{ fm}^2$ | $B(E2) \uparrow$ in $e^2 \text{ fm}^4$ | $B(M1) \uparrow$ in $10^{-3} \mu_N^2$ |
|-----------------|----------------------|---------------------------|---|---|--|
| 9622(1) | $135(27) \cdot 10^1$ | 0.84(22) | 4.36(86) | - | - |
| 9633(2) | $94(13) \cdot 10^1$ | - | - | - | 273(37) |
| 9705(4) | $136(20) \cdot 10^1$ | - | 4.27(62) | - | - |

6.2.4. Average branching ratios

The results for the average branching ratios of electric dipole states in ^{54}Cr are depicted in Figure 6.5. Effects similar to the case of ^{50}Cr are observed here. In particular at low energies, extreme values for $\langle\beta\rangle$ originate from energy settings containing few or none excited states.

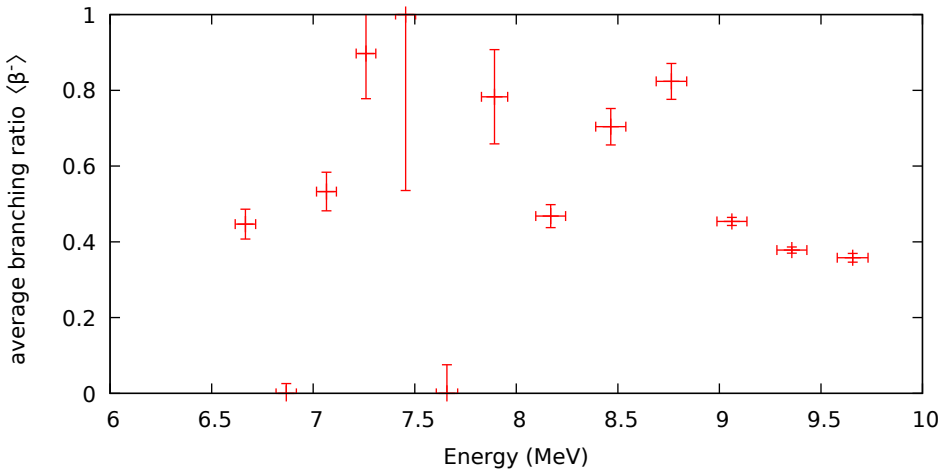


Figure 6.5.: Average branching ratios in ^{54}Cr : The energy intervals given with each data point mark the range of each experimental energy setting.



7. Discussion

One important aspect of the gathered data is the differentiation between electric dipole transition strength and magnetic dipole transition strength, since fundamental different nuclear excitation modes are connected with both, respectively. In this chapter, a discussion of the findings concerning magnetic dipole strength will be conducted, before examining the electric dipole strength. As the focus of this work is on the behavior of the dipole strength across the shell closure, the interpretation will rely on the results of the analyses on the nuclei ^{50}Cr and ^{52}Cr performed by collaborators. The data for ^{52}Cr considered here was taken from Ref. [66], which is based on experiments following the same procedure (see Section 4.5).

7.1. Magnetic dipole strength

A compilation of the ground state $B(M1)$ -values of the isotopes of interest, $^{50,52,54}\text{Cr}$, are given in Figure 7.1. In this figure, the features of the magnetic dipole strength distribution can be recognized, the scissors mode and spin-flip resonance, as they are introduced in Chapter 1.

One striking detail can be found in the high strength of the isolated states just below 4 MeV in ^{50}Cr and ^{54}Cr . The respective excitation energies of 3628(1) keV and 3927(1) keV give an indication of their nature as part of the scissors

mode. In the same manner, the $B(M1)$ values of $1.120(49) \mu_N^2$ and $1.012(38) \mu_N^2$ are within the expected magnitude [10]. Since the scissors mode is understood to be a motion of just the valence neutrons against valence protons, the apparent absence of according strength in ^{52}Cr , exhibiting no valence neutrons at the shell closure $N = 28$, supports this interpretation.

Further investigations into the $M1$ strength associated with the scissors mode were conducted employing shell model calculations. They were executed with the code NuShellX [67], using the effective Hamiltonian GPF1A [68] within the pf model space. The calculations yield excitation energies and $B(M1)$ values for the lowest ten 1^+ states of ^{50}Cr and ^{54}Cr , respectively. The results are visualized in Figure 7.2.

The experimental data for each isotope show one dominant state with strength over $1 \mu_N^2$, which incorporates most of the strength. In contrast to that, the calculations show two states of significant and comparable strength. If comparing the calculation to the experimental results, the overall strength is slightly overestimated, but the excitation energy is well reproduced. More detailed insight is gained, evaluating the individual calculated nuclear matrix elements (NME). For this, the $M1$ operator $\hat{O}(M1)$ is manipulated. Given by

$$\hat{O}(M1) = \sum_{n=1}^Z (g_l^\pi \mathbf{l}_n + g_s^\pi \mathbf{s}_n) + \sum_{n=Z+1}^A (g_l^\nu \mathbf{l}_n + g_s^\nu \mathbf{s}_n), \quad (7.1)$$

with the orbital and spin operators \mathbf{l}_n and \mathbf{s}_n , the g factors $g_{l,s}^{\pi,\nu}$ determine the strength of each term or interaction. The NMEs are determined with four iterations of the calculation per isotope, setting only one g factor to its standard value unequal to zero. The results for the first three states calculated are given in Table 7.1.

As stated above, summing up the $B(M1)$ -values given here for both isotopes, $1.344 \mu_N^2$ and $1.440 \mu_N^2$, the transition strengths of the dominating scissors

Table 7.1.: Nuclear matrix elements from shell model calculations: The results of the calculations for the first three states with excitation energies E_i are listed. The values are determined with only the corresponding g factor set to standard. Also given are the calculated $B(M1)$ -values. Here, $B(M1)_l$ is the resulting transition strength, if no spin contribution is included.

| E_i in MeV | nuclear matrix elements | | | | $B(M1)$ in μ_N^2 | $B(M1)_l$ in μ_N^2 |
|------------------------------------|--------------------------|--------------------------|---------------------------|---------------------------|-------------------------|---------------------------|
| | π spin in μ_N | ν spin in μ_N | π orbit in μ_N | ν orbit in μ_N | | |
| ^{50}Cr | | | | | | |
| 3.347 | -0,253 | -0,082 | -0,591 | -0,056 | 0.968 | 0.420 |
| 4.404 | 0,293 | 0,064 | 0,210 | 0,023 | 0.348 | 0.054 |
| 5.496 | 0,013 | -0,077 | -0,095 | -0,006 | 0.027 | 0.010 |
| ^{54}Cr | | | | | | |
| 3.293 | 0,334 | -0,032 | 0,380 | 0,042 | 0.525 | 0.179 |
| 3.665 | 0,163 | -0,104 | 0,140 | 0,019 | 0.048 | 0.025 |
| 3.702 | 0,176 | 0,312 | 0,411 | 0,032 | 0.867 | 0.196 |

mode states in the experiment, $1.120(49) \mu_N^2$ and $1.012(38) \mu_N^2$, are overestimated. Yet, the sums of the transitions strengths only considering orbital contributions $B(M1)_l$ underestimate the experimental values: For ^{50}Cr $B(M1)_l = 0.484\mu_N^2$ and for ^{54}Cr $B(M1)_l = 0.400\mu_N^2$. Thus, the transition strengths given by the shell model calculations mainly result from spin contributions, which are not observed in the experiment to this degree or not at all, excluding the aforementioned prominent SM states.

The other feature observed for all three isotopes is the spin-flip resonance. In Figure 7.1, a clear separation in energy is observed between the scissors mode strength at 4 MeV and the strength associated to spin-flip around 8 MeV and higher energies. These spin excitations have been attributed to the flip from $f_{7/2} \rightarrow f_{5/2}$ orbitals in ^{50}Cr and ^{52}Cr [59, 49].

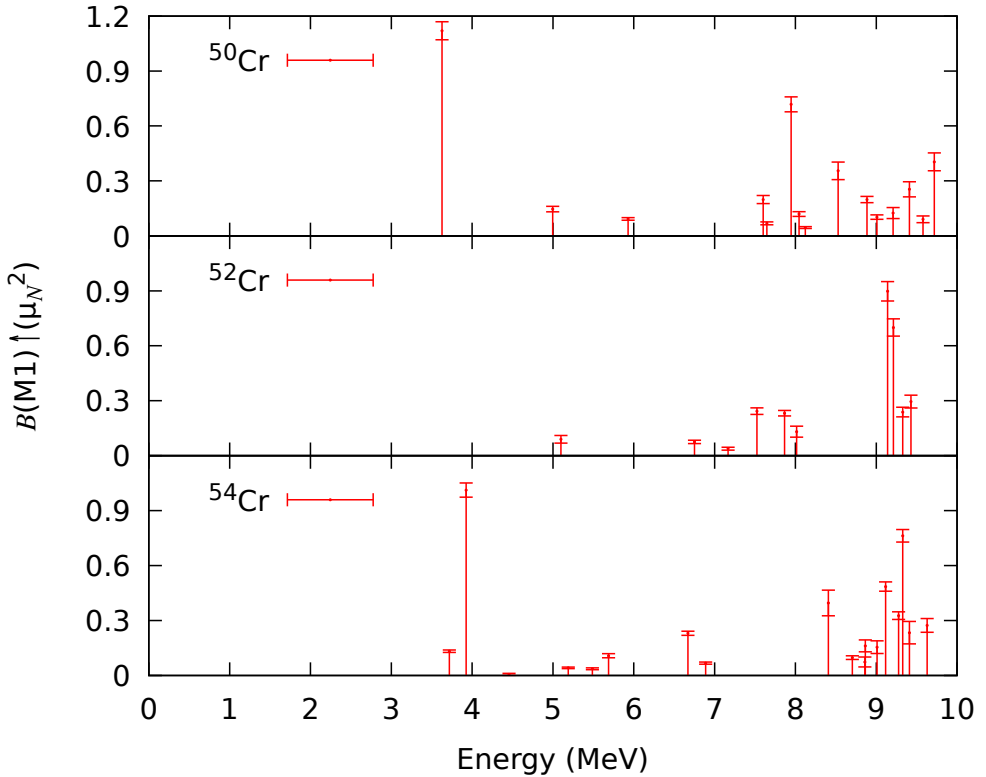


Figure 7.1.: Magnetic dipole transition strengths of examined the chromium isotopes: This compilation of magnetic dipole strength shows the expected features. The scissors mode is observed just below 4 MeV. It is absent in ^{52}Cr , due to missing valence neutrons. Above 7 MeV, all isotopes exhibit the spin-flip resonance.

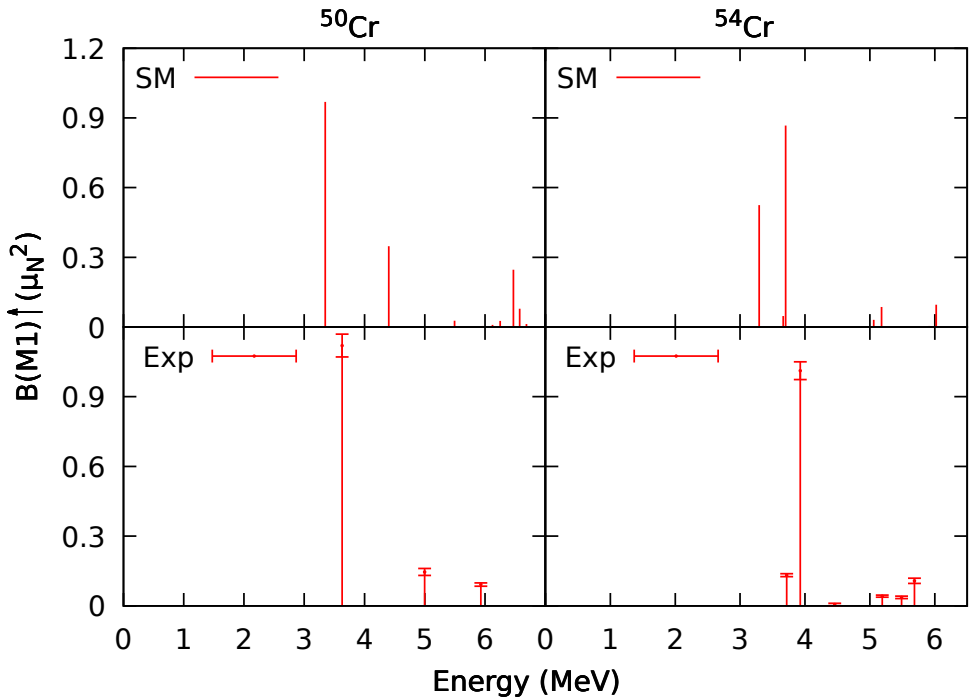


Figure 7.2.: Shell model calculation for the scissors mode in ^{50}Cr and ^{54}Cr : The top panels show the calculations, the bottom one the results of the experiments. The two columns of panels display the isotopes over the range of excitation energy of the lowest ten calculated states, respectively. The states given by the calculations vary in strength over several orders of magnitude, thus not all are visible on the scale of this diagram.

7.2. Electric dipole strength

The ground state $B(E1)$ -values for the stable even-even chromium isotopes, which are partly reported in the previous chapter, are compiled in Figure 7.3. The comparison between the isotopes show an increase in level density and overall strength in ^{54}Cr within the experimental range.

This increase in overall strength can be quantified using the EWSR:

$$\sum_{\text{nucleons}} \sum_i \int dE_i \sigma_{0 \rightarrow i} = I_{\text{total}} \approx \frac{NZ}{A} \cdot 60 \text{MeV mb}. \quad (7.2)$$

In order to compare this estimation with the experimental results, inelastic transitions must be taken into account as well. Since not all individual branching ratios are observed, the average branching ratios are considered to derive corrected excitation cross section for each energy setting $I_{cor, \text{setting}}$. In turn, adding up these individual corrected cross sections, the total corrected cross section I_{cor} can be expressed in terms of the exhausted percentage of the estimation from the EWSR T :

$$T = \frac{I_{cor}}{\frac{NZ}{A} \cdot 60 \text{MeV mb}} \quad (7.3)$$

An effective correcting factor c can be defined as the factor between this percentage and the exhausted percentage, if the average branching ratios are not accounted for.

$$I_{cor} = c \cdot \sum_i I_{0 \rightarrow i \rightarrow 0} \quad (7.4)$$

This procedure of correcting via the average branching ratios was not available for the isotope ^{52}Cr . For this isotope, the peak of the first excited 2_1^+ state at 1434.091(14) keV [69] is contaminated by the natural occurring background at 1435.803(10) keV [54] of the LaBr detectors present in the setup. In order

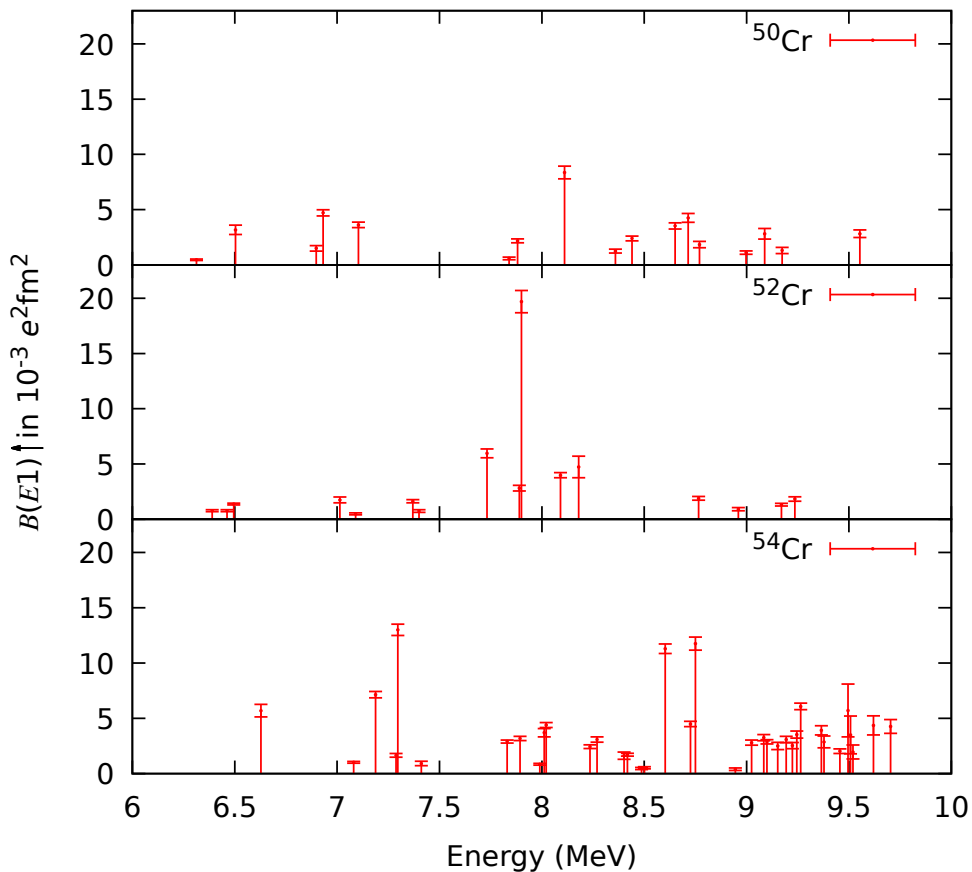


Figure 7.3.: Electric dipole transition strengths of the examined chromium isotopes: In this display, the observed electric dipole strength is shown for the stable even-even chromium isotopes. An increase in level density and overall strength can be observed for ^{54}Cr .

to compare the results for ^{52}Cr as well, the total of the observed cross section of ^{52}Cr is increased by an effective factor of $c_{52\text{Cr}} = 1.79$, which is equal to the average of the two comparable effective factors for ^{50}Cr , $c_{50\text{Cr}} = 1.71$, and ^{54}Cr , $c_{54\text{Cr}} = 1.87$. The results are shown in Figure 7.4.

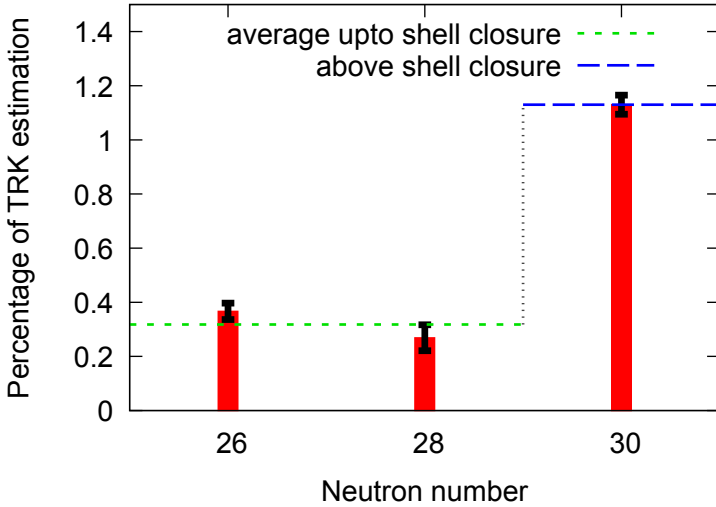


Figure 7.4.: Comparison with the Thomas-Reiche-Kuhn energy-weighted sum rule: The integrated cross section of each state within the energy range of the individual settings at HI γ S are summed up and corrected by the corresponding average branching ratio. Summed up for each isotope, they are compared using the estimations taken from the EWSR.

Since the observed electric dipole transitions are considered to represent the PDR, this shows its little strength of about 1% of the total electric dipole strength, of which the vast majority is contained in the GDR. However, the development of this strength surpassing the shell closure, i.e. the substantial

rise observed in ^{54}Cr , is of interest. Such a rise in strength dependent on the neutron number has not been observed previously. Data available for the Sn isotopes, which reach across subshell closures, do not reflect this behavior [70].

This is in conflict with the prevalent interpretation of the PDR as a collective mode presented in Section 1.2.2, for which a smooth increase in strength is expected as a function of mass number. As the data presented in this work demonstrates, this is not the case, but individual neutrons added and the resulting shell structure affect the PDR strength strongly.

These findings are supported by calculations within a relativistic mean-field (RMF) model utilizing density-dependent meson-nucleon couplings [71]. Here, the neutron skin thickness ΔR_{np} of the chromium nuclei is determined by the difference between the root-mean-square radii of the neutron and the proton density distribution. Details to the calculations are given or referred to in Ref. [51]. The results [72] of these calculations are shown in Figure 7.5. With the calculations not limited by the isotopes stability or abundance, the behavior across the shell closure can be evaluated in a broader view. Linear fits are conducted to each, the data of the isotopes up to and including the shell closure and to the data beyond. As the linear fits to the data reveal, two effects can be observed exceeding the shell closure: On the one hand, an increase of the neutron skin thickness occurs. This increase is bigger than expected, if only the addition of another two neutrons is considered. This is demonstrated by the discontinuity between the linear fits. On the other hand, the rate of growth of the neutron skin $\frac{\delta\Delta R_{np}}{\delta N}$, given by the fits slopes, increases from 0.0256 fm/neutron to 0.0353 fm/neutron, which further indicates a strong influence of the underlying shell structure.

These observations in combination with the experimental results are interpreted as the following: As the closed shell configuration of ^{52}Cr is surpassed, the additional two neutrons of ^{54}Cr are more loosely bound, than those below the magic neutron number $N = 28$. Thus, these valence neutrons cause a

stronger effect on the neutron skin thickness as those filling the core. Since this binding is acting as the restoring force of the neutron skin oscillation in the semi-classical picture, its diminished strength results in a decreased frequency. This in turn implies a lower energy of the mode with larger amplitude. Such a downshift of the PDRs centroid energy above a (sub-)shell closure has been demonstrated in model calculations for the tin and lead isotopic chains, too [73].

The occurrence of this downshift in the experimental data for the chromium isotopes may become apparent, if the running sums of the transition widths $\sum\langle\Gamma\rangle$ are considered, as depicted in Figure 7.6. In this figure, the transition widths corresponding to the corrected cross sections $I_{cor,setting}$ are added up with each energy setting of the measurements at HI γ S. Although, the original (solid) graphs show little commonalities, an upward shift in excitation energy for ^{54}Cr by 800 keV (dashed graph) seems to compensate for the aforementioned downshift.

With the rise of significant $E1$ transition strength in the chromium isotopes, the conclusion is drawn, that the PDR finds its onset here. Its initial character seems to be dictated by valence neutrons, as the strength in respect to the EWSR increases by a factor of 3. Thus, the PDR apparently originates in a few-nucleon effect. However, this does not eliminate the possibility of its evolution to a more collective mode for heavier nuclei. Indeed, a recent *statistical* analysis based on the same data set indicates, that this might already be the case within the Cr isotopic chain itself [74]. One possibility to further investigate this region of the PDRs onset may be given by an extension of the experimental range of excitation energy for ^{50}Cr and ^{52}Cr up to their respective neutron separation thresholds at 13 and 12 MeV. This may consolidate the findings in regards of the energy downshift of the PDR and even make it quantifiable.

Either way, it has been concluded, that the shell structure in the $A \approx 50$ mass region significantly affects the nuclear electric dipole response. If the

correlations of the PDR strength to neutron skin thickness, and with that, to the symmetry energy of the nuclear equation of state are investigated or utilized for predictions, it may be required to consider the shell effects raised in this work.

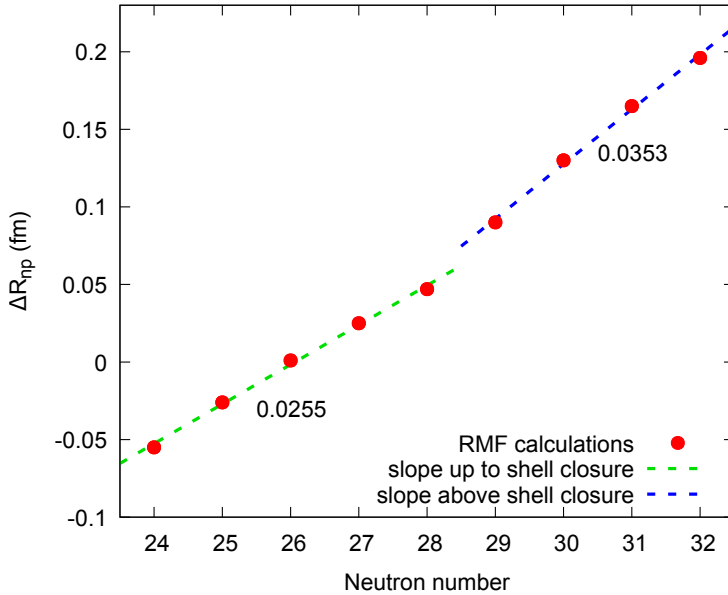


Figure 7.5.: Neutron skin thickness in Cr isotopes: The neutron skin thicknesses ΔR_{np} calculated within the RMF model are shown in red. The dashed lines represent a linear fit to the data for $^{48-52}\text{Cr}$ up to the shell closure (green) and for $^{53-56}\text{Cr}$ above the shell closure (blue), each respectively, which highlight the changing behavior. In addition, the slopes of both fits $\frac{\delta\Delta R_{np}}{\delta N}$ are given by the labels.

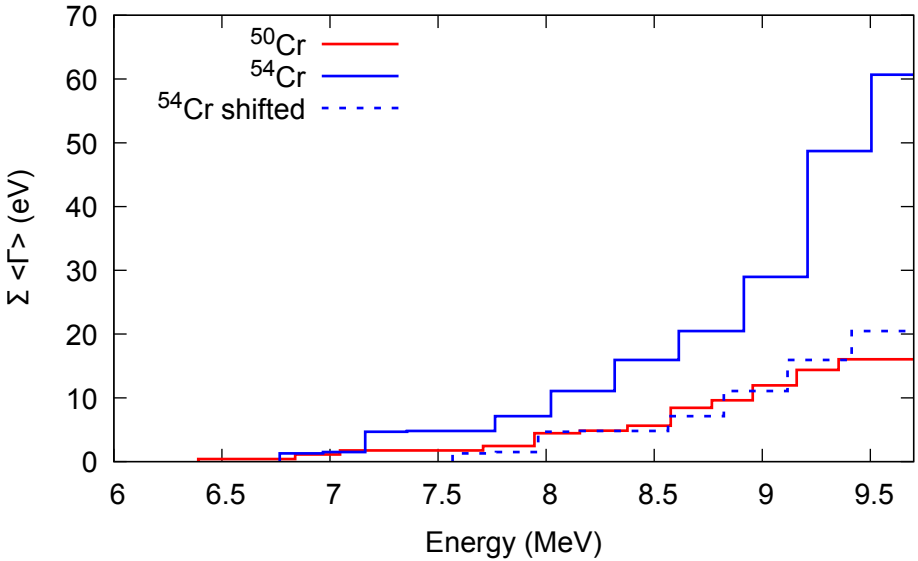


Figure 7.6.: Running sum of transition widths: The solid lines in red and blue show the running sums of the transition widths after correcting for branching ratios $\sum\langle\Gamma\rangle$ of ^{50}Cr and ^{54}Cr , respectively. The dashed blue line shows the same for ^{54}Cr but shifted up by 800 keV. The binning corresponds to the beam-energy setting of the measurements at HI γ S.

8. Summary

In this present work, the data collected through experiments using the NRF-method has been analyzed. The goal of this analysis was the study of the behavior of the low-lying dipole strength in an isotopic chain across a shell closure. The isotopes $^{50,52,54}\text{Cr}$ proved to be the most promising, if not the only possible candidates for doing so using real photons as probes.

The advantages of the NRF-method have been capitalized on and with the selective excitation of dipole states it was possible to determine the observables excitation energies, spin and parity quantum numbers, branching ratios, cross sections and, derived from the latter, transition widths and strengths. As further advantage of these NRF-experiments, the usage of HPGe-detectors revealed numerous states previously unknown, in particular in ^{54}Cr , as this isotope has never been examined in (γ, γ') -experiments before.

Concerning the magnetic dipole excitation, the observed strength followed the expected behavior and exhibits quite symmetric features around the shell closure. This means in particular, that, with available valence neutrons, the scissors mode is observed in ^{50}Cr and ^{54}Cr . For both isotopes, its strength is concentrated in one state just below 4 MeV excitation energy and with just above $1 \mu_N^2$ transition strength. Shell-model calculations have been performed to complement the experimental findings. However, shell model interactions and commonly used effective g-factors need to be adjusted to experimental

findings. As to be expected, no scissors mode is observed in ^{52}Cr . Accumulations of spin-flip states above 8 MeV are present in all three isotopes.

More distinguished behavior is found for the electric dipole strength. A significant and abrupt increase in ^{54}Cr demonstrates a extensive influence of the shell structure on the PDR. Calculations yielding neutron skin thicknesses within the RMF model solidified these findings, extending beyond the isotopes accessible in the experiment. The results even suggest an increase of the rate, with which the $E1$ strength grows. In particular, these finding should be taken into consideration, if the electric dipole strength associated with the PDR and the linked neutron skin thickness are examined in order to gain insights on the parametrization of the EoS.

The experiments leading up to this work have been conducted specifically to ensure comparability between the isotopes. In particular, the interpretation arguing for a downshift of the PDR in ^{54}Cr may motivate measures to improve in this regard. In detail, fixing the experimental range to the neutron separation energy of ^{54}Cr at 9.7 MeV could be considered to cut off the range of data acquisition for ^{50}Cr and ^{52}Cr at a rather arbitrary point. The extension of the experimental range to each isotopes separation energy may provide an more intuitive cut off. A more robust assessment of the PDRs strength and centroid energy might follow for that.

A. Spectra of the measurements of the isotope ^{54}Cr

This appendix shows the spectra for the isotope ^{54}Cr measured at DHIPS and HI γ S. The angles given for each detector refer to the polar angle at DHIPS and the azimuthal angle at HI γ S. The part below 2.5 MeV is omitted for the DHIPS spectra. For the HI γ S spectra, the energy range of the corresponding quasi-monoenergetic γ -ray beam, i.e. mean energy ± 200 keV, is shown. Only two HPGe detectors were operational for the spectra from 6300 keV to 6900 keV.

A.1. Spectra recorded at DHIPS

A.1.1. Endpoint energy 7.5 MeV

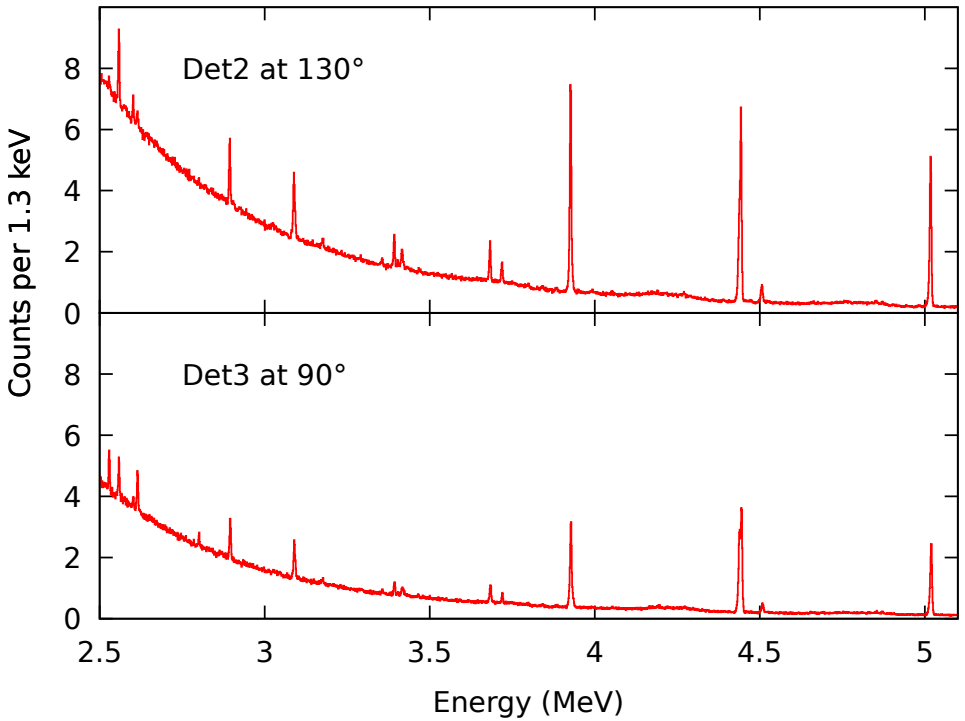


Figure A.1.: Spectra of the isotope ^{54}Cr recorded at DHIPS with an electron endpoint energy of 7.5 MeV: The energy range from 2.5 to 5.1 MeV is shown.

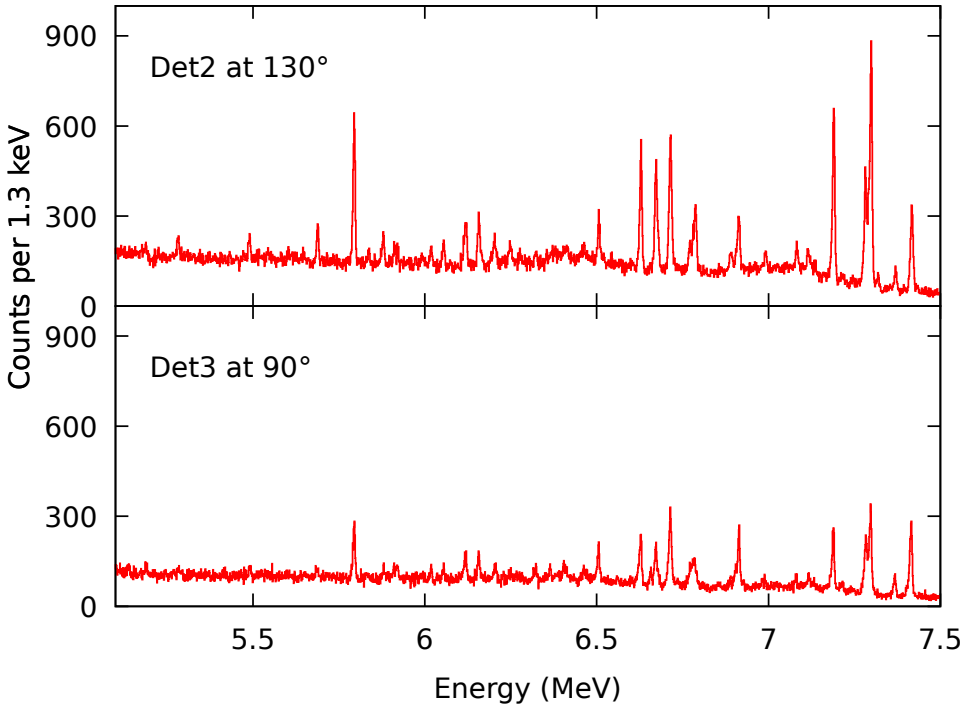


Figure A.2.: Spectra of the isotope ^{54}Cr recorded at DHIPS with an electron endpoint energy of 7.5 MeV: The energy range from 5.1 to 7.5 MeV is shown.

A.1.2. Endpoint energy 9.7 MeV

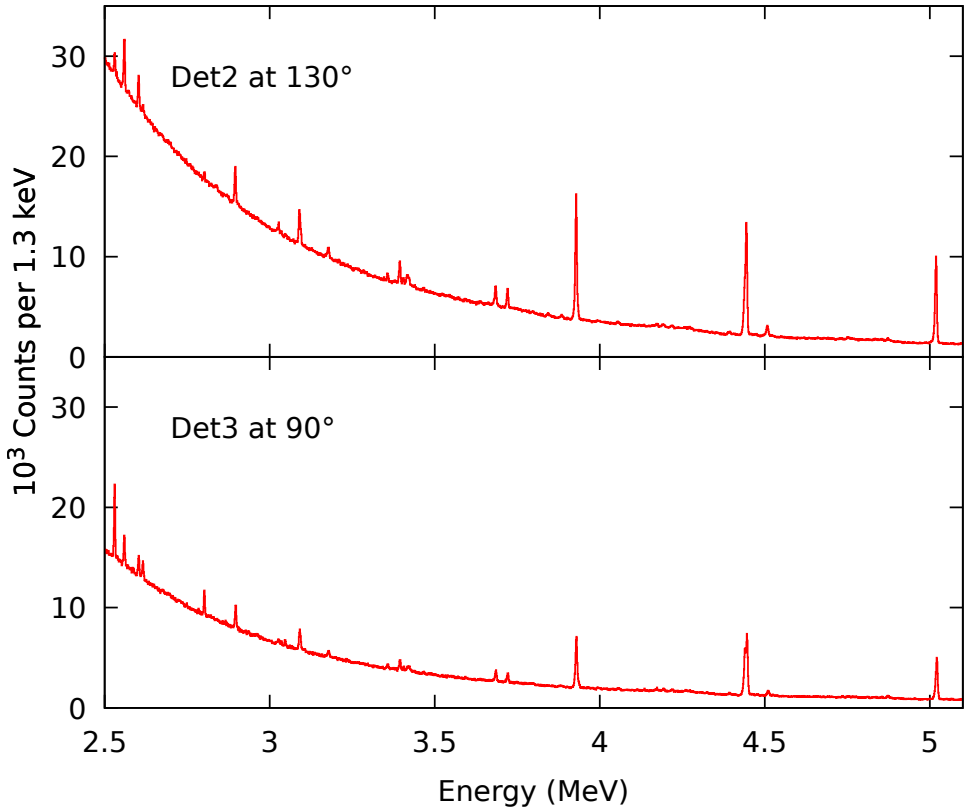


Figure A.3.: Spectra of the isotope ^{54}Cr recorded at DHIPS with an electron endpoint energy of 9.7 MeV: The energy range from 2.5 to 5.1 MeV is shown.

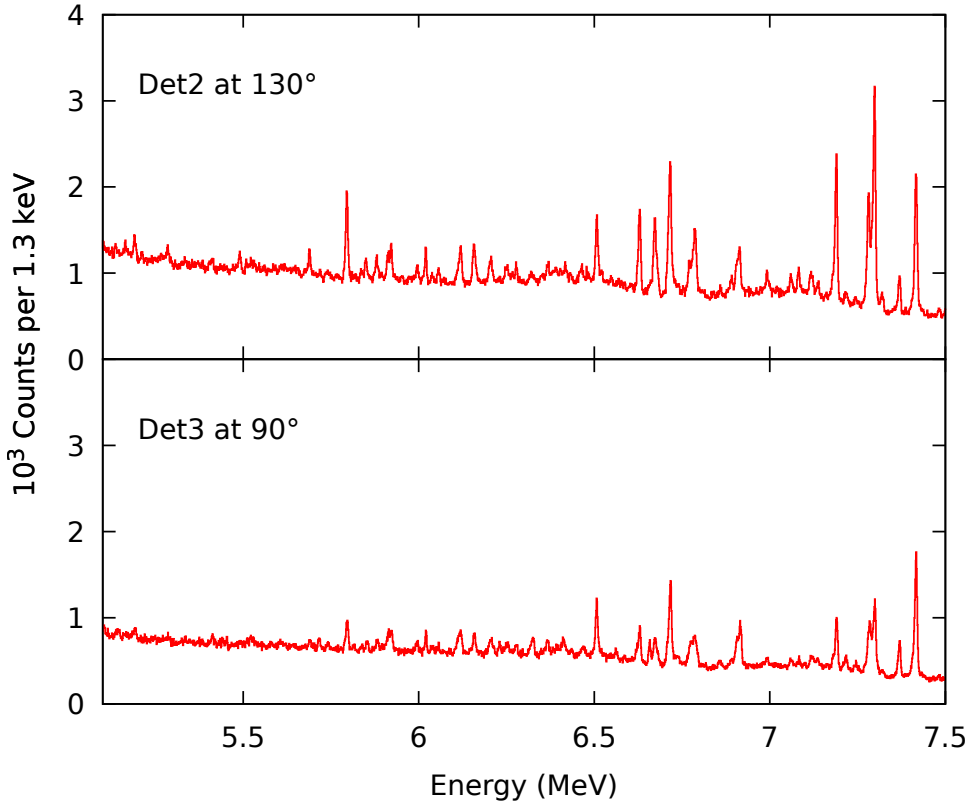


Figure A.4.: Spectra of the isotope ^{54}Cr recorded at DHIPS with an electron endpoint energy of 9.7 MeV: The energy range from 5.1 to 7.5 MeV is shown.

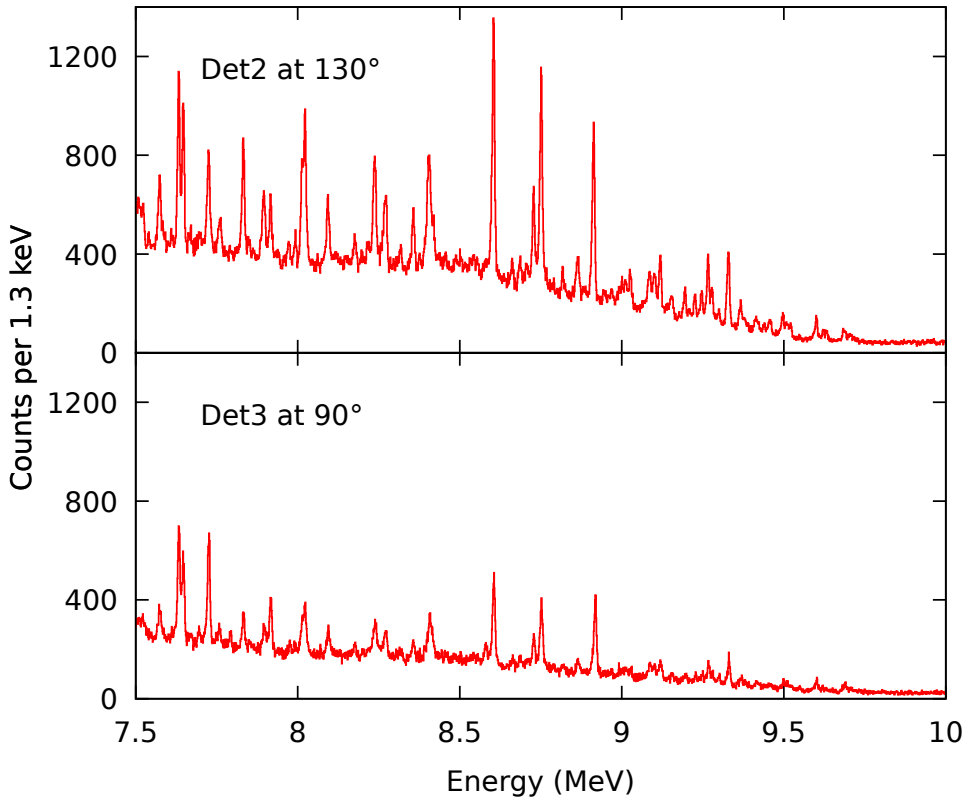


Figure A.5.: Spectra of the isotope ^{54}Cr recorded at DHIPS with an electron endpoint energy of 9.7 MeV: The energy range from 7.5 to 10 MeV is shown.

A.2. Spectra recorded at HI γ S

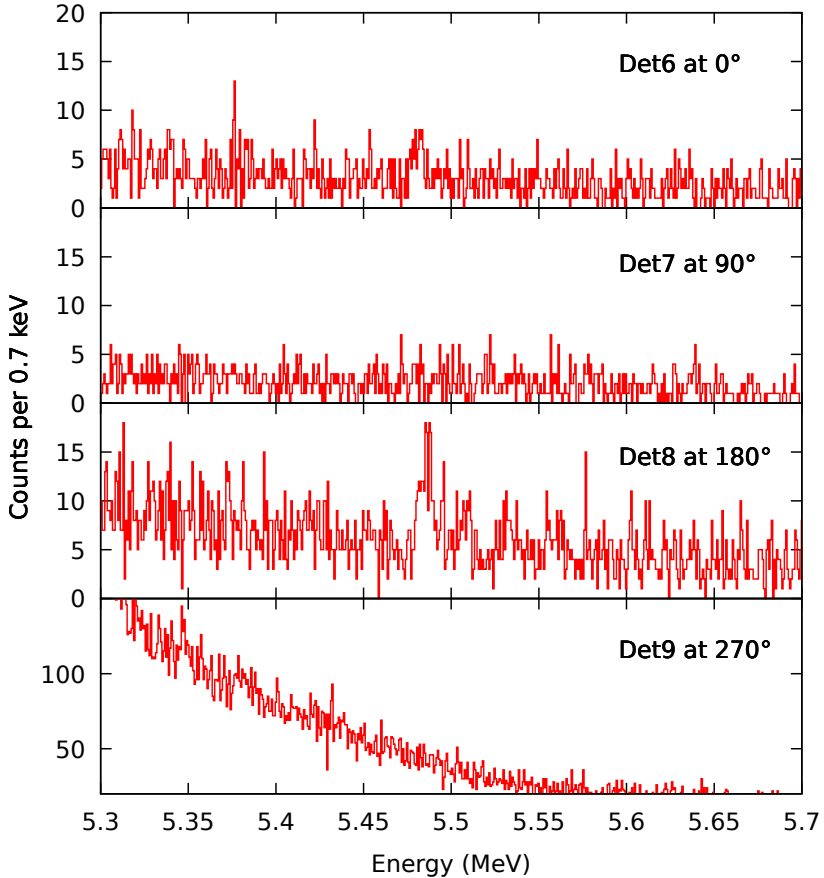


Figure A.6.: Spectra of the isotope ^{54}Cr recorded at HI γ S. The mean energy of the photon beam is 5.5 MeV.

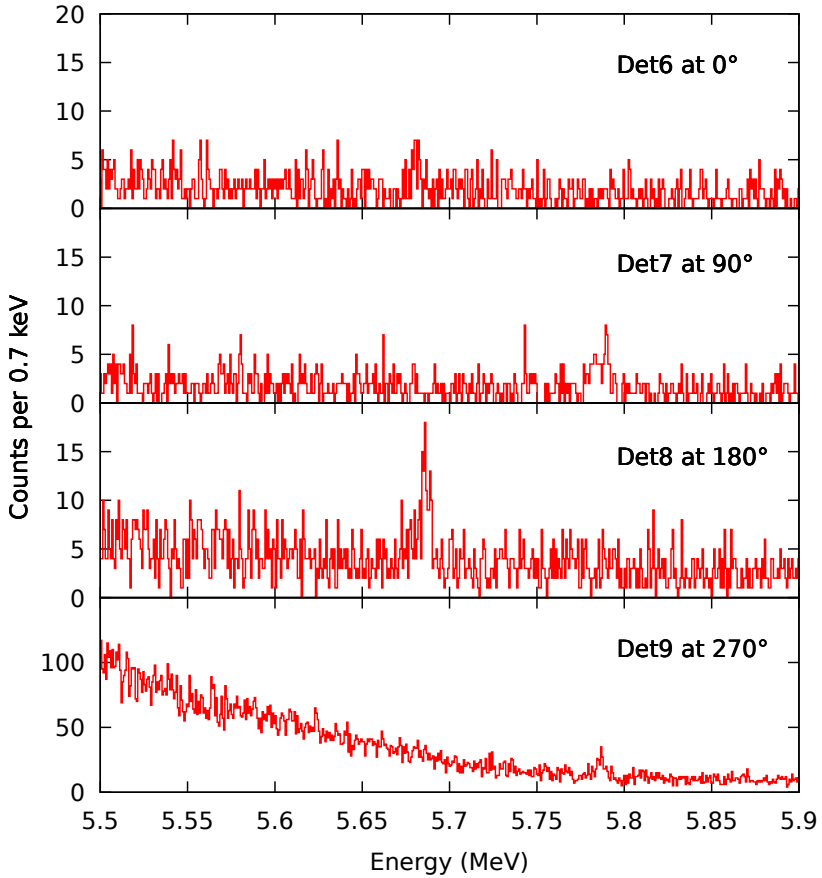


Figure A.7.: Spectra of the isotope ^{54}Cr recorded at HI γ S. The mean energy of the photon beam is 5.7 MeV.

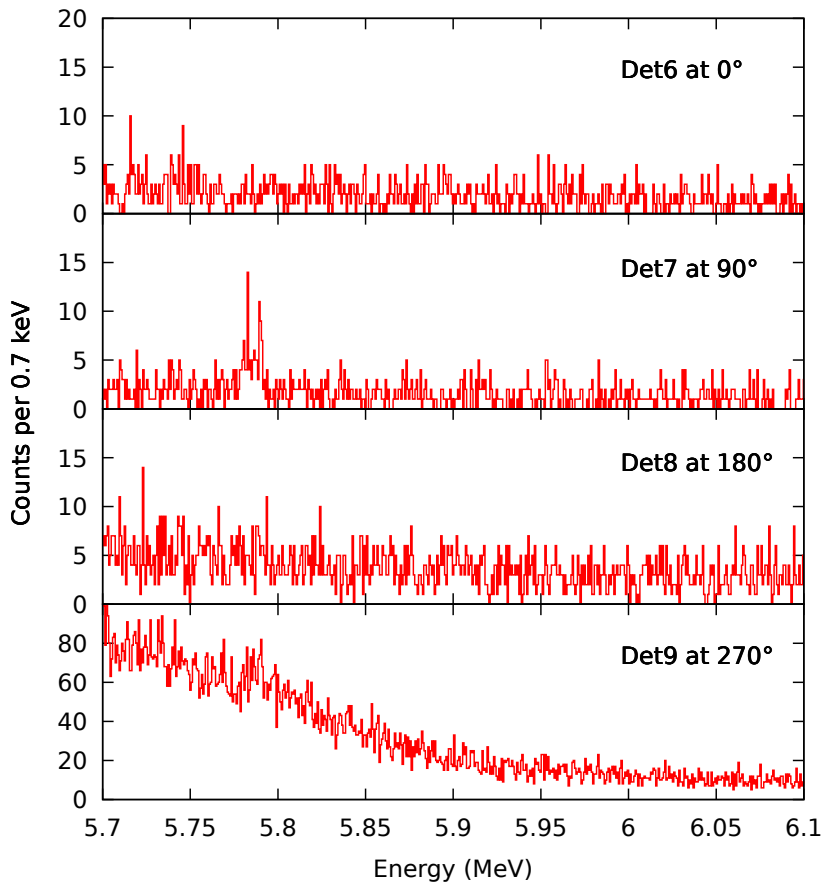


Figure A.8.: Spectra of the isotope ^{54}Cr recorded at $\text{HI}\gamma\text{S}$. The mean energy of the photon beam is 5.9 MeV.

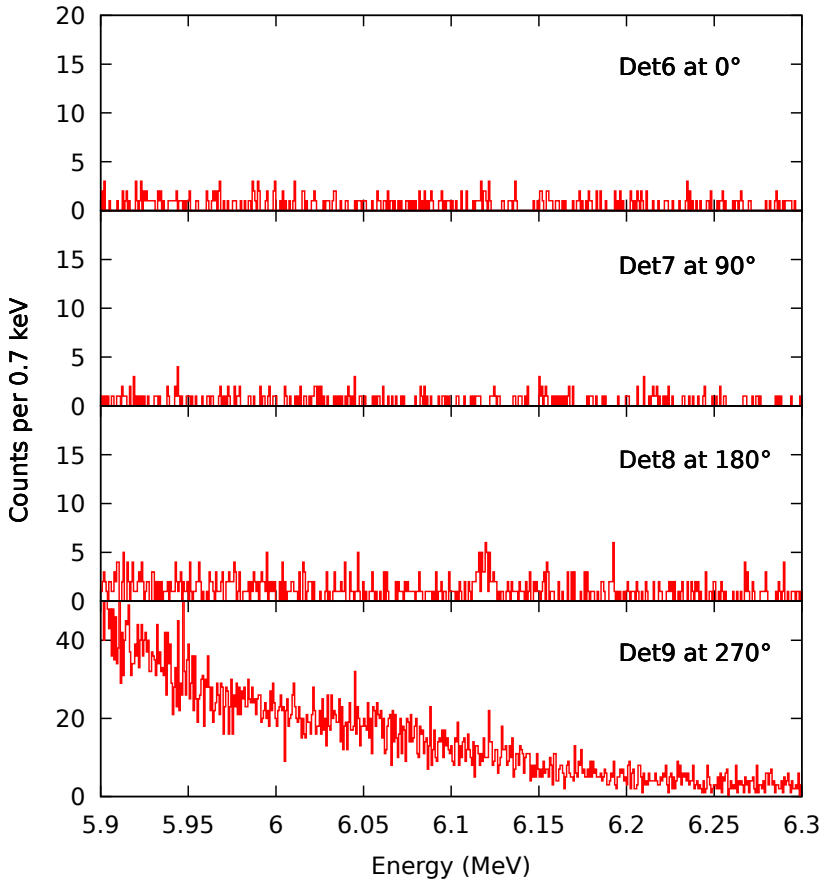


Figure A.9.: Spectra of the isotope ^{54}Cr recorded at HI γ S. The mean energy of the photon beam is 6.1 MeV.

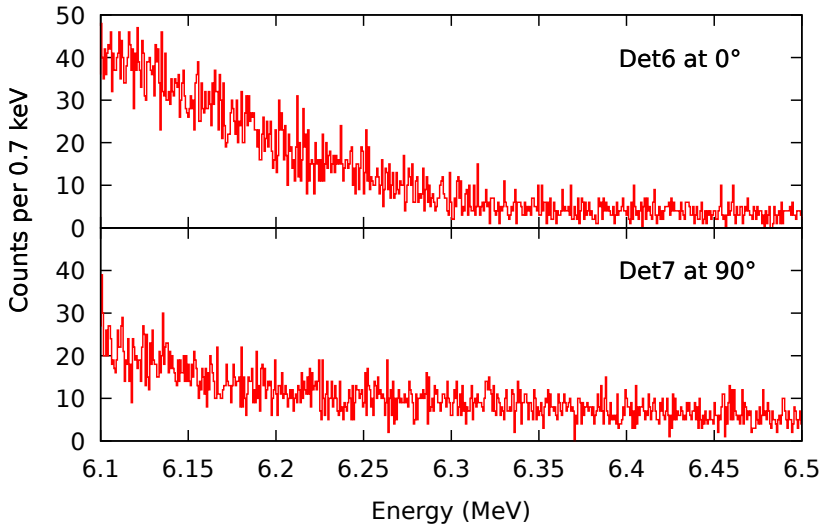


Figure A.10.: Spectra of the isotope ^{54}Cr recorded at HI γ S. The mean energy of the photon beam is 6.3 MeV.

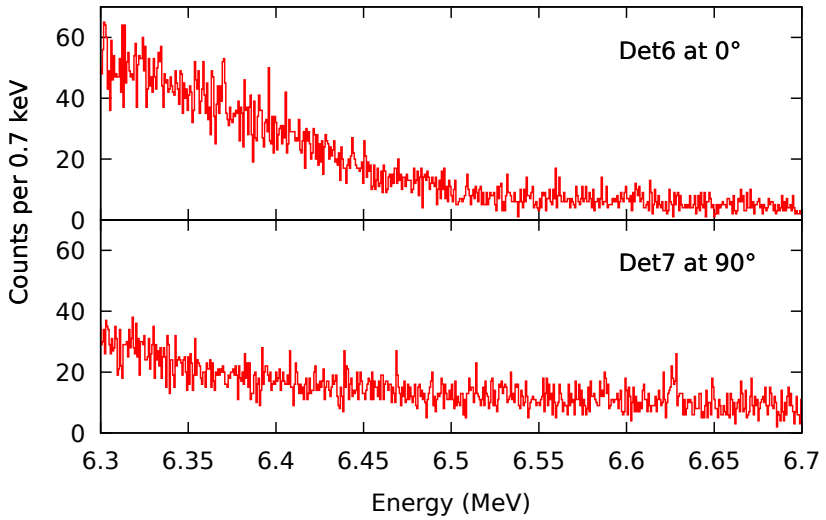


Figure A.11.: Spectra of the isotope ^{54}Cr recorded at HI γ S. The mean energy of the photon beam is 6.5 MeV.

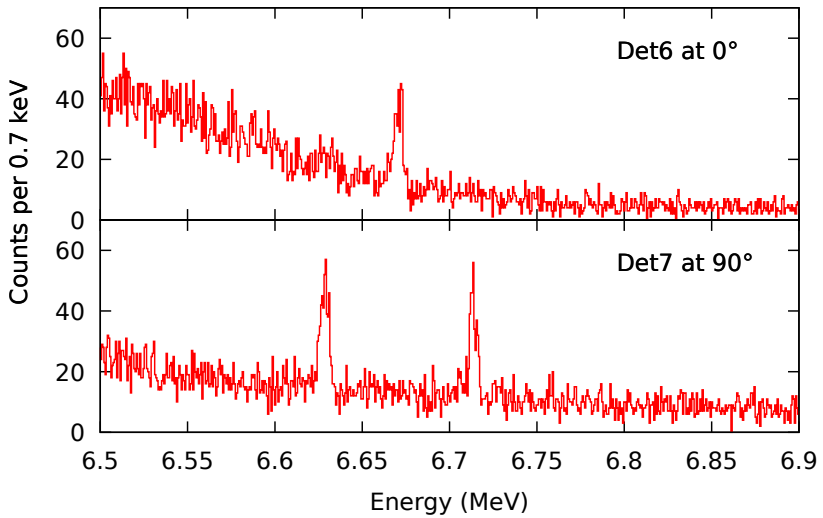


Figure A.12.: Spectra of the isotope ^{54}Cr recorded at HI γ S. The mean energy of the photon beam is 6.7 MeV.

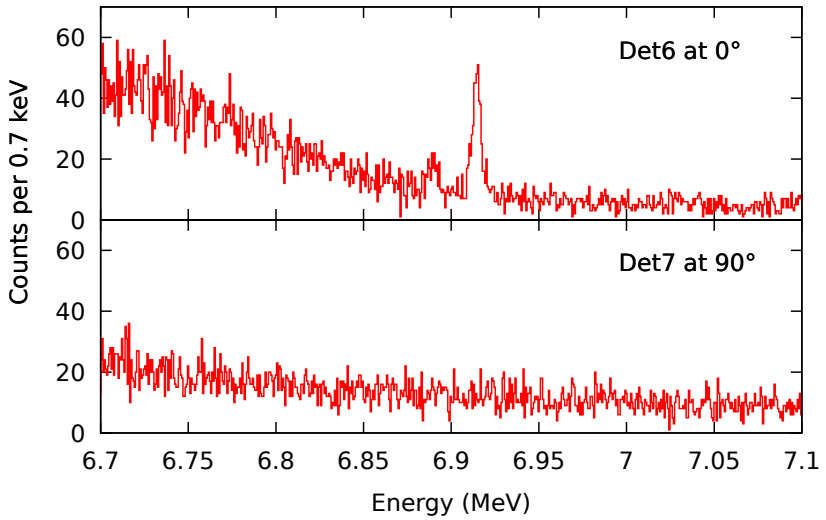


Figure A.13.: Spectra of the isotope ^{54}Cr recorded at HI γ S. The mean energy of the photon beam is 6.9 MeV.

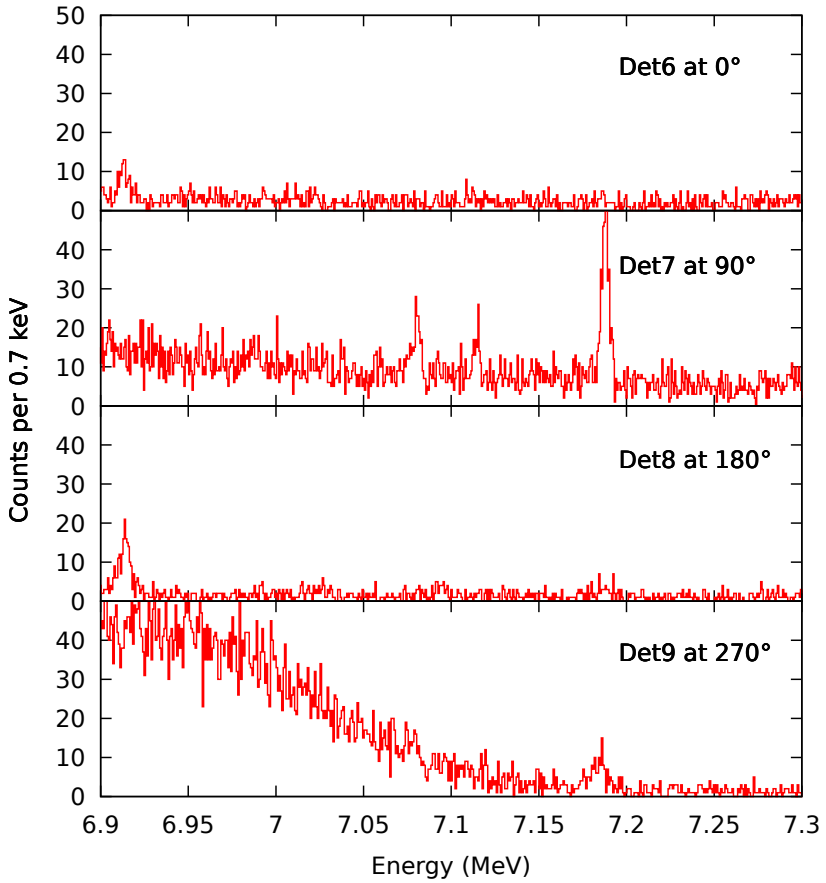


Figure A.14.: Spectra of the isotope ^{54}Cr recorded at HI γ S. The mean energy of the photon beam is 7.1 MeV.

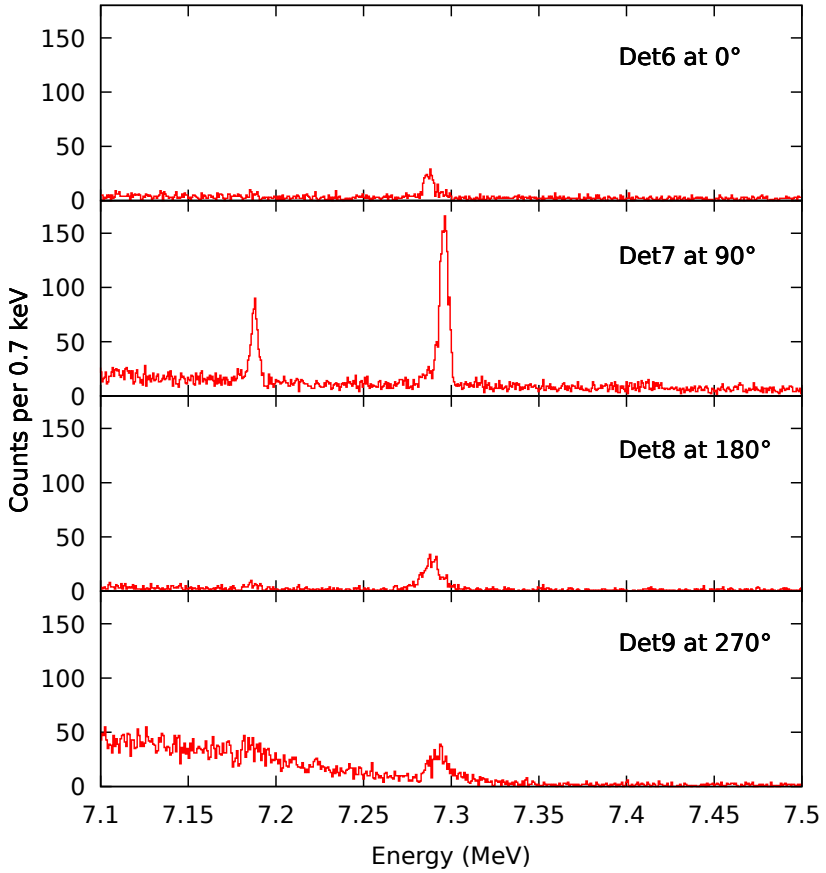


Figure A.15.: Spectra of the isotope ^{54}Cr recorded at HI γ S. The mean energy of the photon beam is 7.3 MeV.

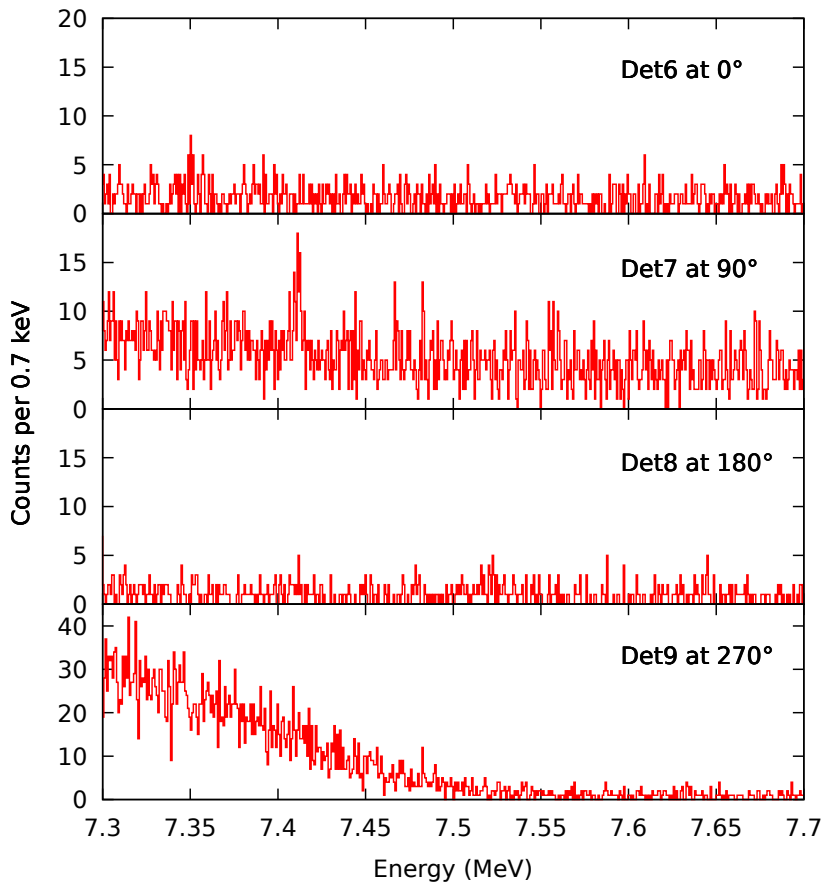


Figure A.16.: Spectra of the isotope ^{54}Cr recorded at HI γ S. The mean energy of the photon beam is 7.5 MeV.

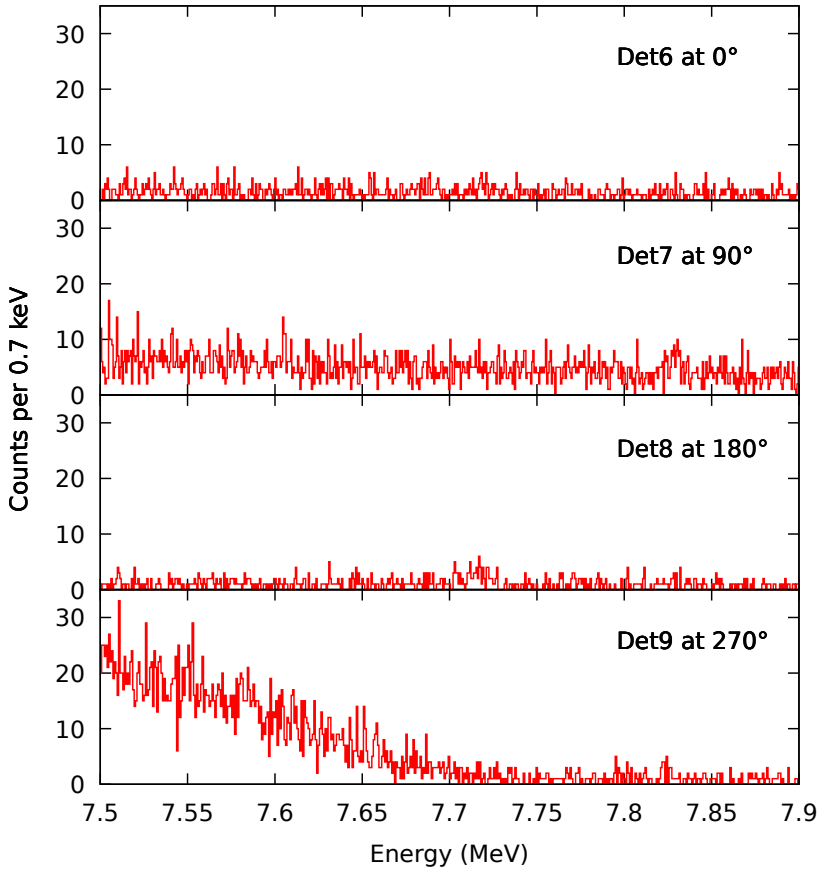


Figure A.17.: Spectra of the isotope ^{54}Cr recorded at HI γ S. The mean energy of the photon beam is 7.7 MeV.

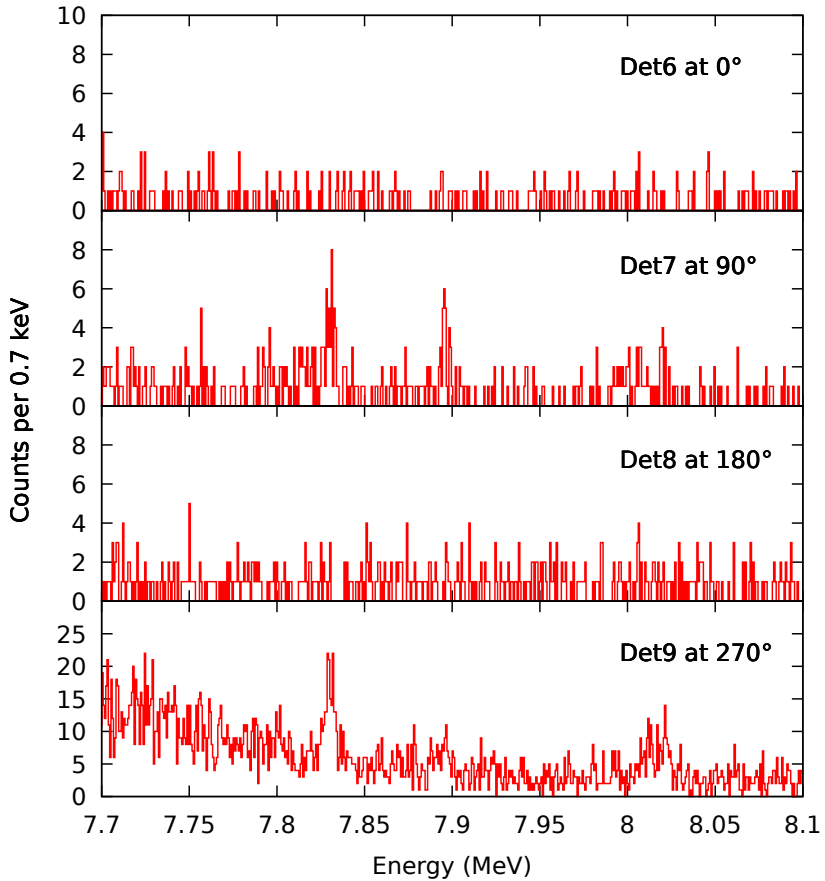


Figure A.18.: Spectra of the isotope ^{54}Cr recorded at HI γ S. The mean energy of the photon beam is 7.9 MeV.

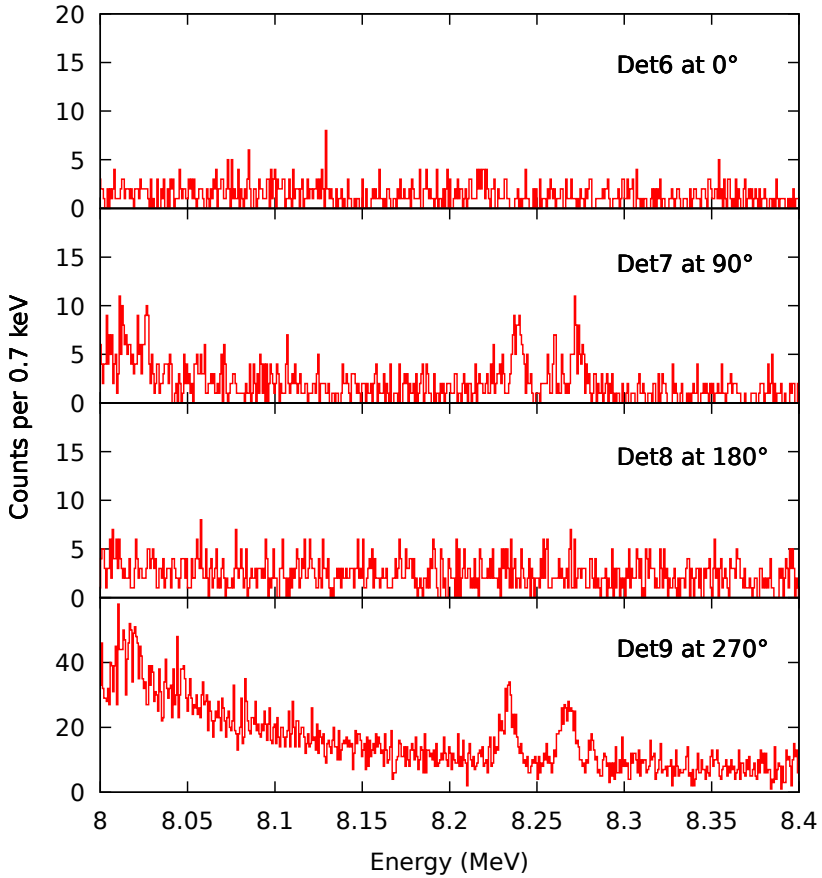


Figure A.19.: Spectra of the isotope ^{54}Cr recorded at HI γ S. The mean energy of the photon beam is 8.2 MeV.

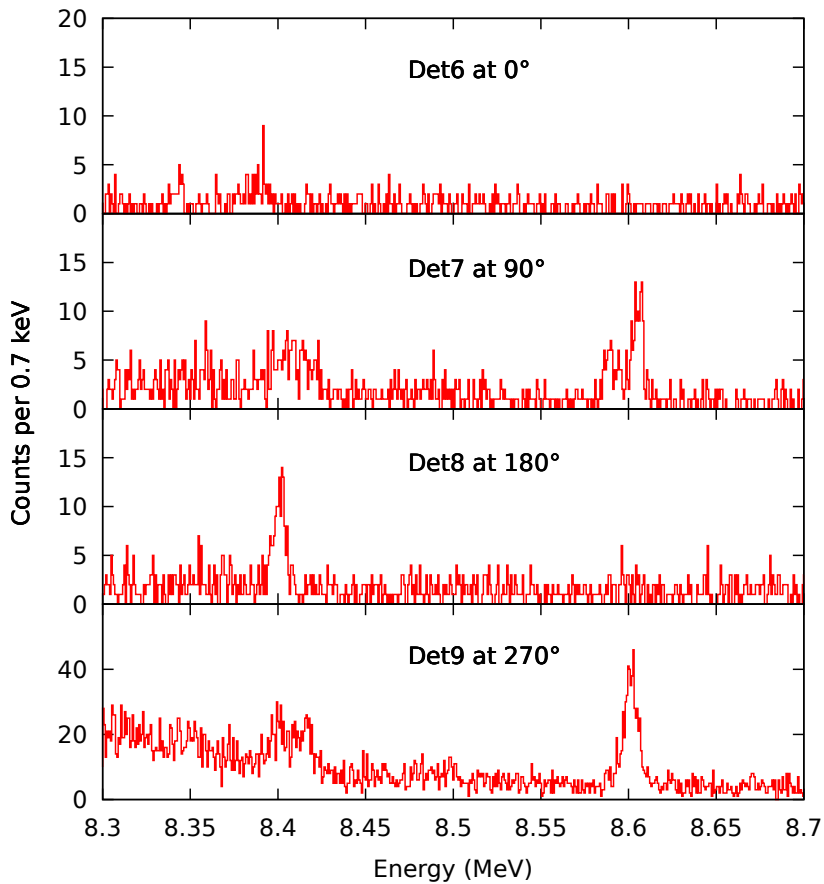


Figure A.20.: Spectra of the isotope ^{54}Cr recorded at HI γ S. The mean energy of the photon beam is 8.5 MeV.

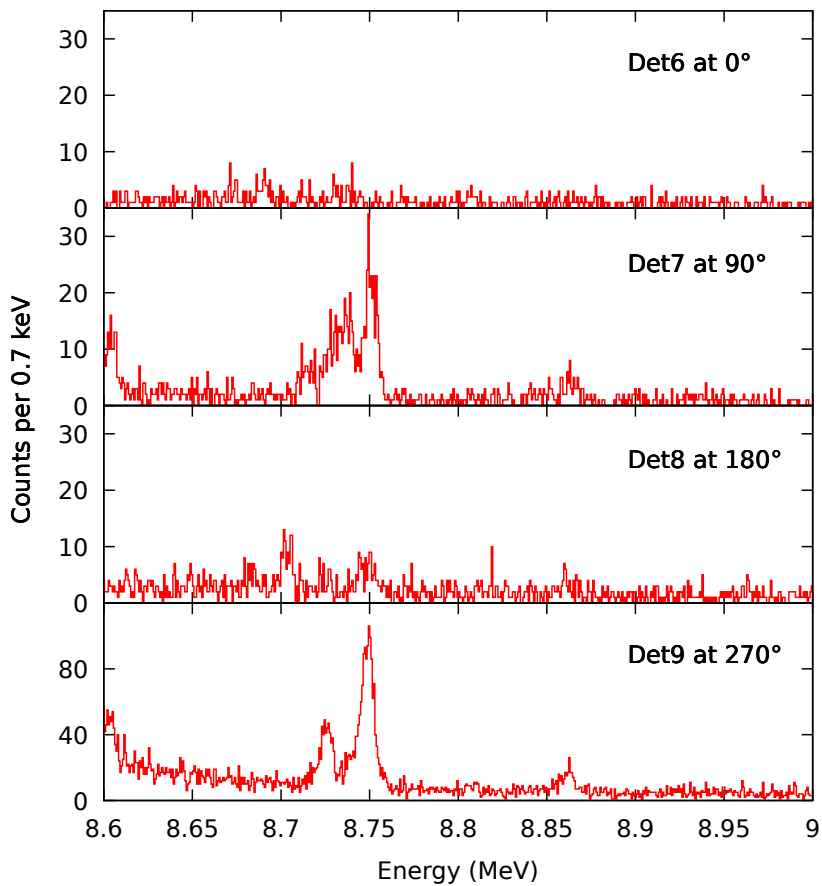


Figure A.21.: Spectra of the isotope ^{54}Cr recorded at HI γ S. The mean energy of the photon beam is 8.8 MeV.

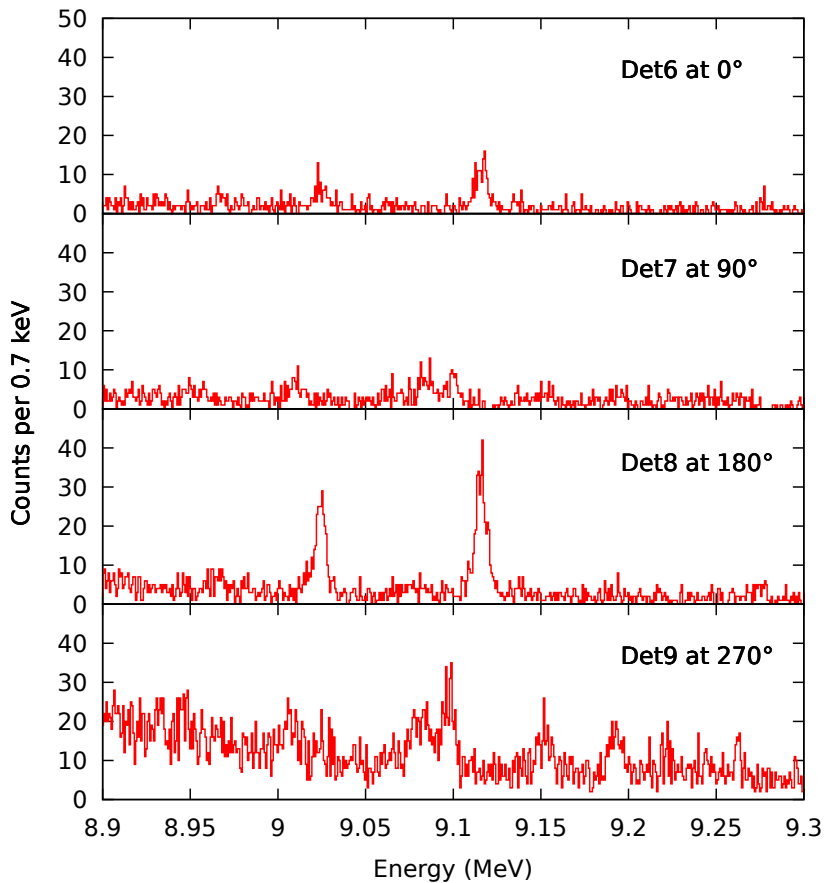


Figure A.22.: Spectra of the isotope ^{54}Cr recorded at HI γ S. The mean energy of the photon beam is 9.1 MeV.

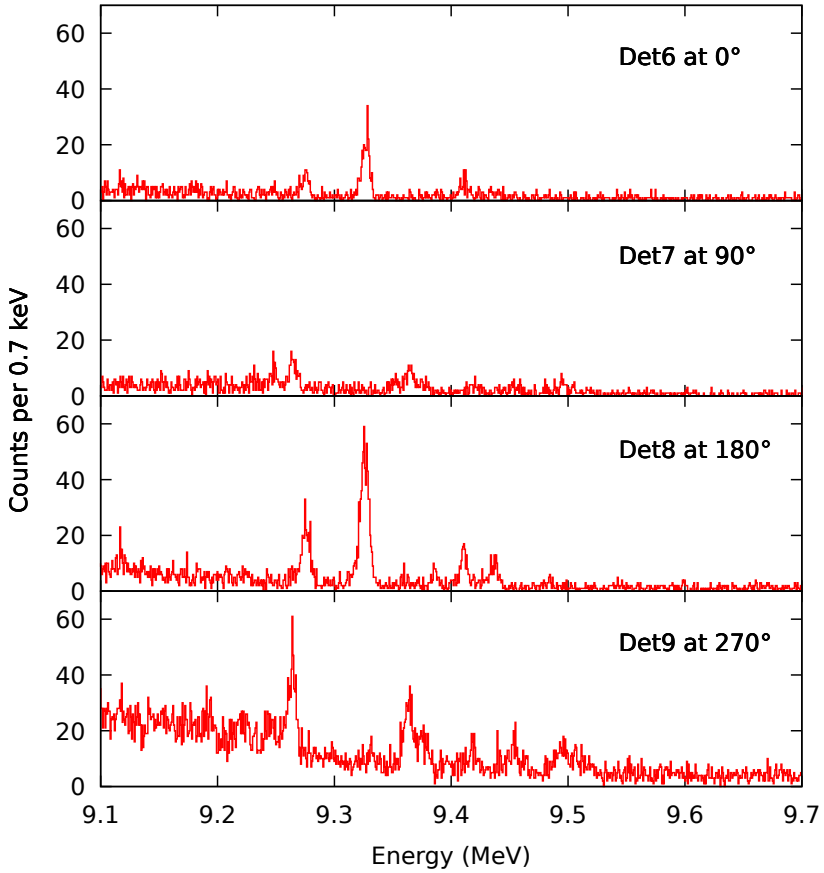


Figure A.23.: Spectra of the isotope ^{54}Cr recorded at HI γ S. The mean energy of the photon beam is 9.4 MeV.

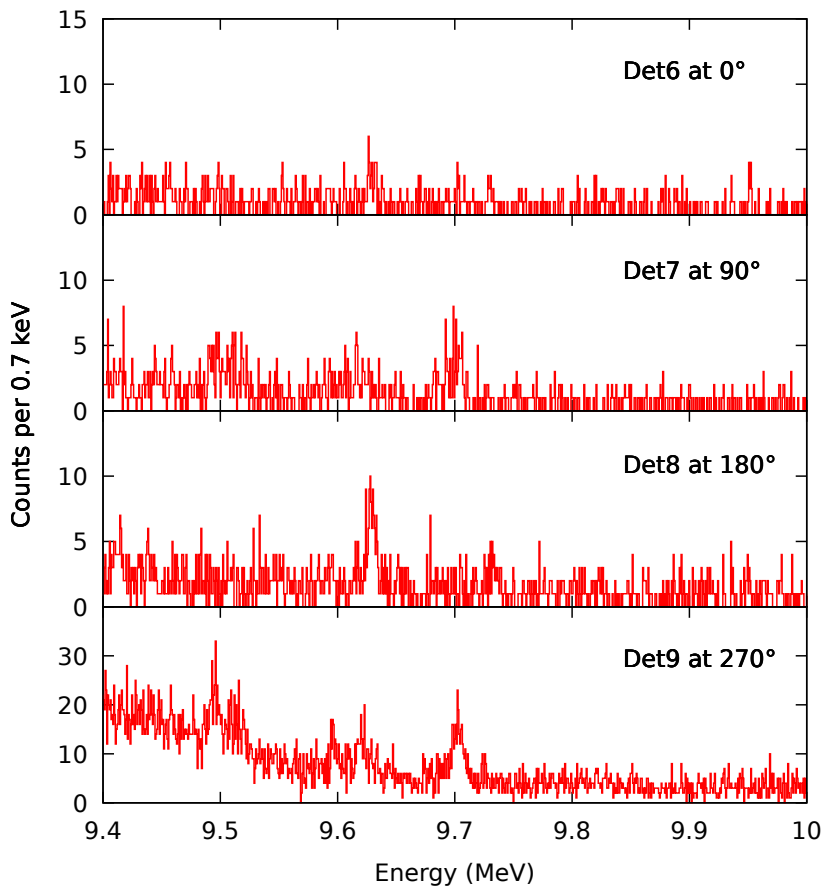


Figure A.24.: Spectra of the isotope ^{54}Cr recorded at HI γ S. The mean energy of the photon beam is 9.7 MeV.

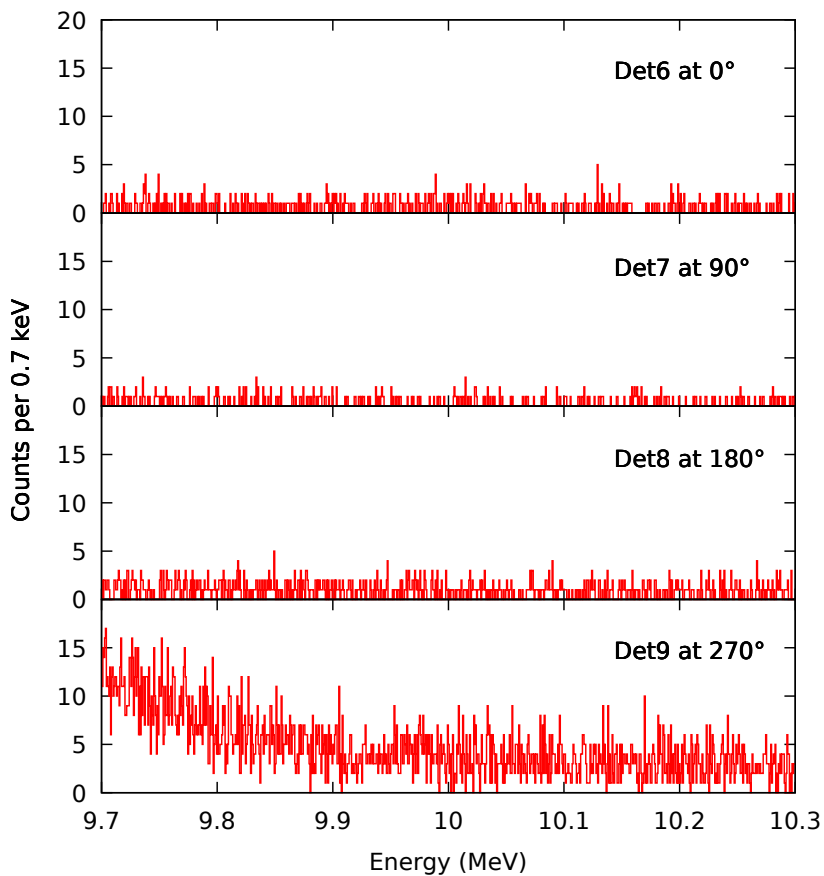


Figure A.25.: Spectra of the isotope ^{54}Cr recorded at HI γ S. The mean energy of the photon beam is 10.0 MeV.

B. LINTOTT scattering chamber

The following appendices present the results of work, which was performed parallel to the analysis and interpretation of the experiments on chromium, but is not directly linked to them. In particular, this section shows specifics of the new scattering chamber of the so-called LINTOTT electron spectrometer at the S-DALINAC. It replaced the existing one, which was suffering from wear and tear. The most severe problems were posed by worn-out screw threads and scratched sealing surfaces, which hampered the application of vacuum. The new scattering chamber was designed in cooperation with and produced by the Kurt J. Lesker Company. Fig. B.1 shows a schematic drawing of the new chamber. Technical drawings including essential measurements are presented in Figure B.2 and Figure B.3. Details, which will be explained in the following text, are marked with corresponding number.

This design is based on the previous scattering chamber to great extent in order to be compatible with the existing infrastructure at the experimental site. However, it was complemented with steel cartridges for the screw threads, so-called HELICOILS®, to prolong their lifetime. Moreover, with this opportunity several other changes were incorporated in the design of the new chamber, which improve and augment the handling of the scattering chamber and associated equipment at the spectrometer. These include a snap closing lid for easy access (1), markings of the cardinal angles and available scattering angles for alignment purposes (2) as well as standardized (3-7) and additional

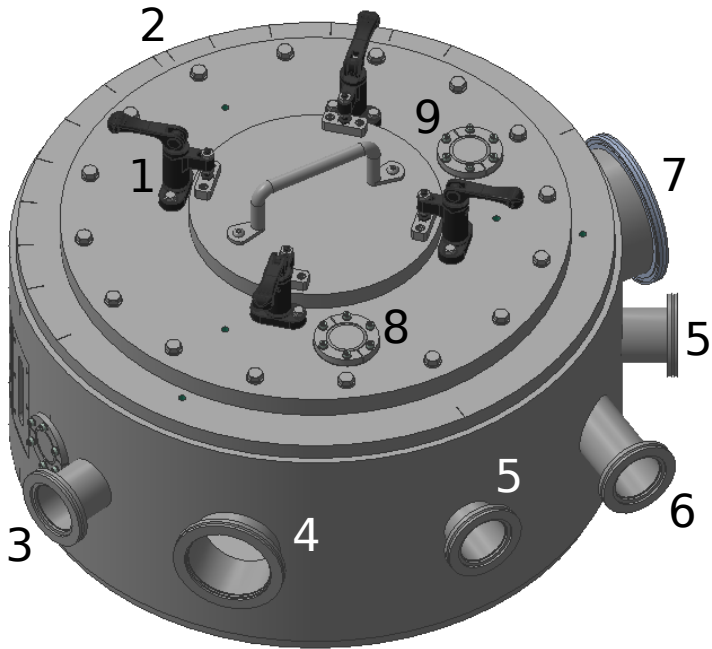


Figure B.1.: Schematic drawings of the new scattering chamber design: The numbers mark details, which correspond to significant changes or additions with respect to the design of the hitherto existing chamber: snap closing lid (1), markings (2), ISO-K-63 view port (3), ISO-K-100 flange for turbo-pump (4), ISO-K-63 flanges for multipurpose (5) and OTR-view-port (6), ISO-K-160 flange for downstream beampipe (7), ISO-KF-40 flange for multipurpose (8) and OTR-target (9).

(8,9) vacuum flanges. The additional flange (9) on top of the chamber allows the installation of a target downstream from the scattering target. Such a tar-

get made of metal and irradiated by the electron beam would produce optical transition radiation (OTR). The intensity of this emitted visible light can be used to quantify the current of the initial electron beam and can be measured by a CCD-camera placed at the dedicated flange (6) at 90° with respect to the beam. The chamber is produced out of aluminum, which reduced weight and cost compared to steel. Furthermore, in the process of exchanging the scattering chamber, a valve was added in the beamline behind the chamber itself, which allows to significantly decrease the volume, which has to be pumped after accessing the chamber during the experiment campaign. Therefore, the existing beam pipe was shortened and a standardized flange (ISO-K-200) was welded on.

The scattering chamber itself was certified by the production company to be leak tight up to background levels of 7×10^{-10} STD cc/sec. A pressure of $< 10^{-5}$ mbar was achieved after installation at the spectrometer and connected to beamline and vacuum system.

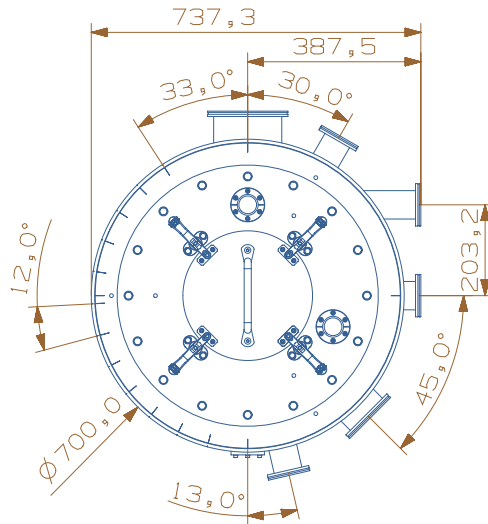


Figure B.2.: Technical drawing of the new scattering chamber top view: The beam passes in vertical direction, entering from the bottom. The measurements are given in millimeter. The positioning of the spectrometer ports resembles the old design, beginning at 33° and continuing in 12° steps.

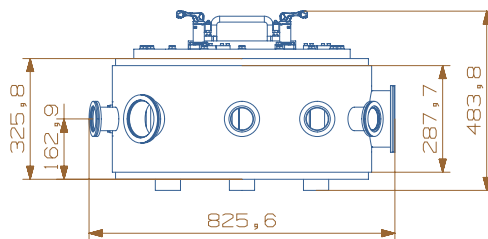


Figure B.3.: Technical drawing of the new scattering chamber side view: The beam passes in horizontal direction, entering from the left. The measurements are given in millimeter.

C. Gas target

In this section, the newly designed and produced containers for gaseous targets at the electron spectrometers LINTOTT and QClam at the S-DALINAC accelerator facility are presented. Preceding that, experiments on xenon gas, performed in the December 2018, showed, that the containers used so far were no longer suitable. Their cylindrical shape allowed for the path lengths in material of the scattered electrons to vary up to 2 cm, as visualized in Figure C.1. The resulting spread of energy loss within the target surpassed the improved, inherent energy spread of the electron beam and consequently was the leading factor for an insufficient energy resolution.

The new design features a planar geometry of the volume for gases, which minimizes the difference in path lengths in the material, as can be seen in Figure C.1. Technical drawings containing the essential measurements of the new container are shown in Figures C.2 and C.3. A target container consists of a front and a back part, manufactured from a single aluminum piece each, which feature thin beam entry and exit windows. These parts are separated by supporting frames, that determine the target thickness and hold a rubber seal in place.

In comparison to the previous target containers, the area density of probed gas is necessarily substantially reduced for the new design. Considering natural Xe gas and an average target thickness of the gas of 1.57 cm, the old design would provide an area density of $9.26 \frac{\text{mg}}{\text{cm}^2}$ at standard conditions. The new

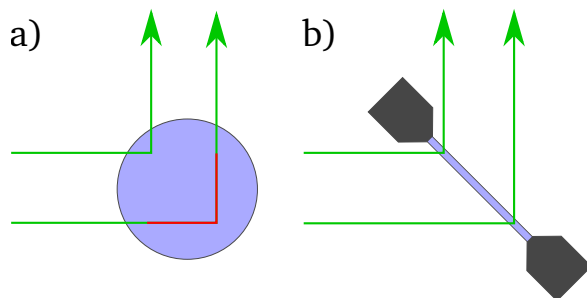


Figure C.1.: Comparison of old and new gaseous target designs: Schematics of both target designs are shown. Panel a) features a profile of the old, cylindrical design and panel b) of the new, planar one. The path length of scattered electrons (green) within the target material (blue) may vary substantially for a) (difference highlighted in red). The geometry in b) is similar to conventional electron scattering target, albeit comparatively thick.

design with 0.141 cm thickness (for 90° scattering angle) provides $0.83 \frac{\text{mg}}{\text{cm}^2}$. In order to compensate for this, the new containers are meant to be pressurized with the gas of interest during an experiment. A test performed using helium with a pressure of up to 4 bar in atmospheric environment indicated, that the containers can withstand these pressures. The pressure dropped at an average rate of 13 mbar/d, as can be seen in Figure C.4. Tests exceeding the time period considered here or pressurizing of the containers excessive number of times have not been performed. It stands to reason, that repeated pressurizing of an individual container may weaken the filigree windows for beam entry. Therefore, a failure of a container and sudden release of the content should in general not be foreclosed.

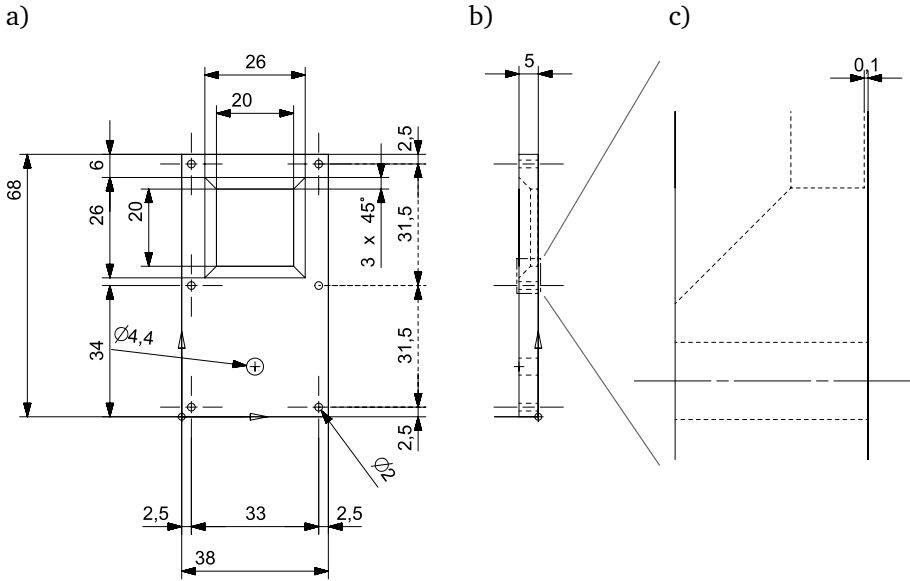


Figure C.2.: Technical drawing of the new target container: The panels show: a) front view, b) side view and c) enlarged cutout of the side view. The part depicted is the frontal half of the container, which is identical to the back part, with the exception of the hole for intake. All measurements are given in millimeter.

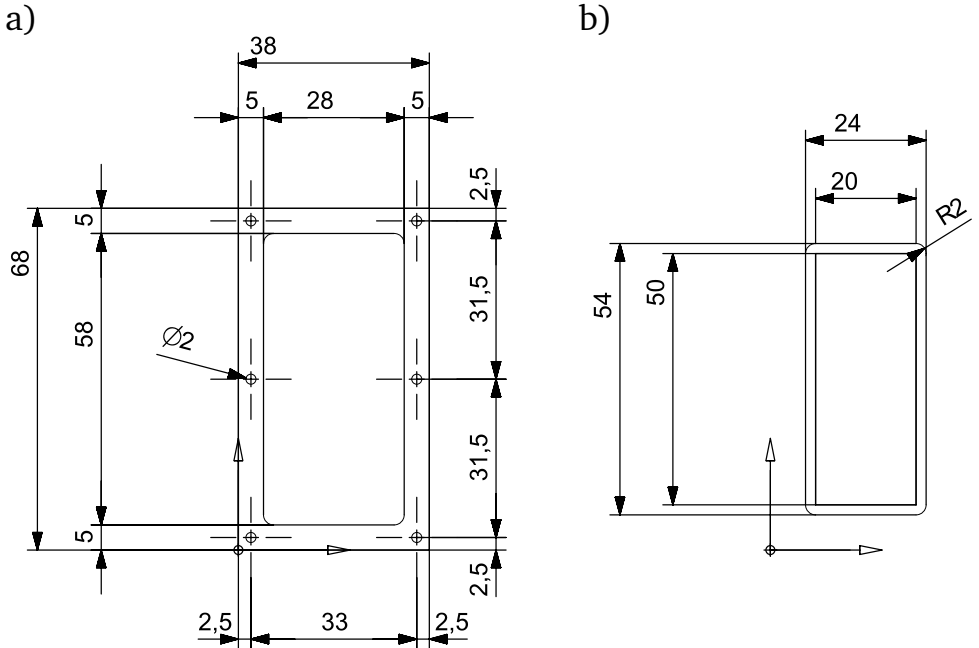


Figure C.3.: Technical drawing of the support frame of the target container: The panels show: a) the outer support frame and b) the inner one. These support frames have thickness of one millimeter and thus determine the thickness of the gaseous target. The rubber sealing is hold in place between both frames.

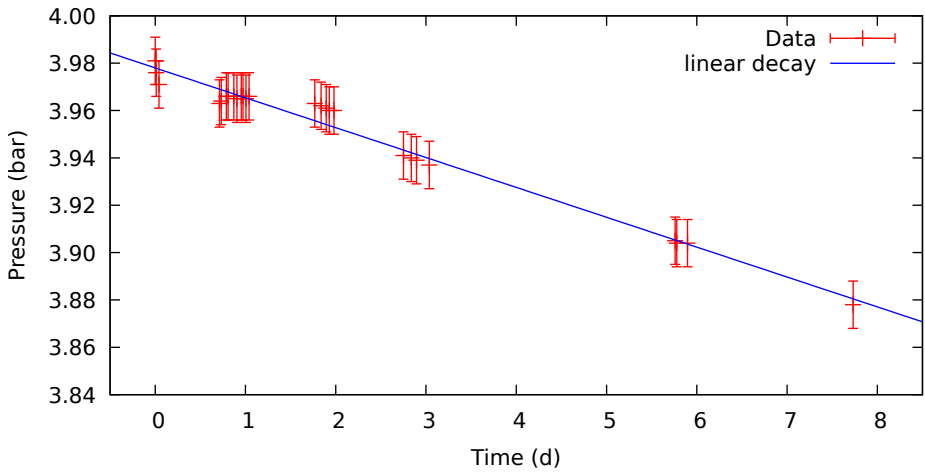


Figure C.4.: Gas target leak rate: Measurements of the pressure in the target container are shown in red. The uncertainties of 0.01 bar are estimated by the maximal fluctuation within a day. A linear fit is shown in blue. Its gradient equals $-12.6(4)$ mbar/d.



Bibliography

- [1] H. Becquerel. Sur les radiations émises par phosphorescence. *Compte Rendu*, 122:501, 1896.
- [2] P. Curie, M. Curie, and G. Bémont. Sur une nouvelle substance fortement radio-active contenue dans la pechblende. *omptes rendus hebdomadaires des séances de l'Académie des sciences*, 127:1215–1217, 1898.
- [3] E. Rutherford. The scattering of α and β particles by matter and the structure of the atom. *Philosophical Magazine*, 92(4):379–398, 2012.
- [4] J. Chadwick. Possible existence of a neutron. *Nature*, 129:312, 1932.
- [5] W. Heisenberg. Über den bau der atomkerne. *Zeitschrift für Physik*, 77(1):1–11, Jan 1932.
- [6] G. Gamow. Mass defect curve and nuclear constitution. *Proc. R. Soc. Lond. A*, 126, 1930.
- [7] M. G. Mayer. On closed shells in nuclei. *Phys. Rev.*, 74:235–239, Aug 1948.
- [8] Roger D. Woods and David S. Saxon. Diffuse surface optical model for nucleon-nuclei scattering. *Phys. Rev.*, 95:577–578, Jul 1954.

-
- [9] 'Shells.png' by the user Bakken of the english Wikipedia at <https://commons.wikimedia.org/wiki/File:Shells.png>. licence at <https://creativecommons.org/licenses/by-sa/3.0/> as of 26.9.2019.
- [10] Kris Heyde, Peter von Neumann-Cosel, and Achim Richter. Magnetic dipole excitations in nuclei: Elementary modes of nucleonic motion. *Rev. Mod. Phys.*, 82:2365–2419, Sep 2010.
- [11] N. Pietralla, C. Fransen, D. Belic, P. von Brentano, C. Frießner, U. Kneissl, A. Linnemann, A. Nord, H. H. Pitz, T. Otsuka, I. Schneider, V. Werner, and I. Wiedenhöver. Transition rates between mixed symmetry states: First measurement in ^{94}Mo . *Phys. Rev. Lett.*, 83:1303–1306, Aug 1999.
- [12] A. Arima, T. Ohtsuka, F. Iachello, and I. Talmi. Collective nuclear states as symmetric couplings of proton and neutron excitations. *Physics Letters B*, 66(3):205 – 208, 1977.
- [13] Ulrich Kneissl, Norbert Pietralla, and Andreas Zilges. Low-lying dipole modes in vibrational nuclei studied by photon scattering. *Journal of Physics G: Nuclear and Particle Physics*, 32(8):R217–R252, Jun 2006.
- [14] R. A. Gatenby, J. R. Vanhoy, E. M. Baum, E. L. Johnson, S. W. Yates, T. Belgia, B. Fazekas, Á. Veres, and G. Molnár. Fast $E1$ transitions and evidence for octupole-octupole and quadrupole-octupole excitations in ^{144}Sm . *Phys. Rev. C*, 41:R414–R418, Feb 1990.
- [15] M. Wilhelm, S. Kasemann, G. Pascovici, E. Radermacher, P. von Brentano, and A. Zilges. Two-phonon character of the lowest electric dipole excitation in ^{142}Nd and in other nuclei near shell closures. *Phys. Rev. C*, 57:577–582, Feb 1998.
- [16] Norbert Pietralla. Empirical correlation between two-phonon $E1$ transition strengths in vibrational nuclei. *Phys. Rev. C*, 59:2941–2944, May 1999.

-
- [17] Helmut Steinwedel, J. Hans D. Jensen, and Peter Jensen. Nuclear dipole vibrations. *Phys. Rev.*, 79:1019–1019, Sep 1950.
- [18] W. Bothe and W. Gentner. Atomumwandlungen durch γ -strahlen. *Zeitschrift für Physik*, 106(3):236–248, Mar 1937.
- [19] G. C. Baldwin and G. S. Klaiber. Photo-fission in heavy elements. *Phys. Rev.*, 71:3–10, Jan 1947.
- [20] M. Goldhaber and E. Teller. On nuclear dipole vibrations. *Phys. Rev.*, 74:1046–1049, Nov 1948.
- [21] W. Kuhn. Über die gesamtstärke der von einem zustande ausgehenden absorptionslinien. *Zeitschrift für Physik*, 33(1):408–412, Dec 1925.
- [22] F. Reiche and W. Thomas. Über die zahl der dispersionselektronen, die einem stationären zustand zugeordnet sind. *Zeitschrift für Physik*, 34(1):510–525, Dec 1925.
- [23] Radhe Mohan, M. Danos, and L. C. Biedenharn. Three-fluid hydrodynamical model of nuclei. *Phys. Rev. C*, 3:1740–1749, May 1971.
- [24] G.A. Bartholomew. Neutron capture gamma rays. *Annu. Rev. Nucl. Sci.*, 11:259–302, 1961.
- [25] J.S. Brzosko, E. Gierlik, A. Soltan, and Z. Wilhelmi. Effect of the pigmy resonance on the calculations of the neutron capture cross section. *Can. J. Phys.*, 47:2849, 1969.
- [26] D. Savran, T. Aumann, and A. Zilges. Experimental studies of the pygmy dipole resonance. *Progress in Particle and Nuclear Physics*, 70:210 – 245, 2013.
- [27] J. Piekarewicz. Pygmy resonances and neutron skins. *Phys. Rev. C*, 83:034319, Mar 2011.

-
- [28] B.A. Brown. Neutron radii in nuclei and the neutron equation of state. *Phys. Rev. Lett.*, 85:5296–5299, Dec 2000.
- [29] M. Oertel, M. Hempel, T. Klähn, and S. Typel. Equations of state for supernovae and compact stars. *Rev. Mod. Phys.*, 89:015007, Mar 2017.
- [30] A. Klimkiewicz, N. Paar, P. Adrich, M. Fallot, K. Boretzky, T. Aumann, D. Cortina-Gil, U. Datta Pramanik, Th. W. Elze, H. Emling, *et al.* Nuclear symmetry energy and neutron skins derived from pygmy dipole resonances. *Phys. Rev. C*, 76:051603, Nov 2007.
- [31] J. Piekarewicz. Pygmy dipole resonance as a constraint on the neutron skin of heavy nuclei. *Phys. Rev. C*, 73:044325, Apr 2006.
- [32] X. Roca-Maza and N. Paar. Nuclear equation of state from ground and collective excited state properties of nuclei. *Progress in Particle and Nuclear Physics*, 101:96 – 176, 2018.
- [33] G. Audi, F.G. Kondev, M. Wang, *et al.* The ubase2016 evaluation of nuclear properties. *Chin Phys. C*, 41(3):030001, 2017.
- [34] F.R. Metzger. Resonance fluorescence in nuclei. *Prog. in Nucl. Phys.*, 53, 1959.
- [35] U. Kneissl, H.H. Pitz, and A. Zilges. Investigation of nuclear structure by resonance fluorescence scattering. *Porg. Part. Nucl. Phys.*, 37:349–433, 1996.
- [36] H. A. Bethe and G. Placzek. Resonance effects in nuclear processes. *Phys. Rev.*, 51:450–484, Mar 1937.
- [37] K. S. Krane and R. M. Steffen. Determination of the $\frac{E2}{M1}$ multipole mixing ratios of the gamma transitions in ^{110}Cd . *Phys. Rev. C*, 2:724–734, Aug 1970.

-
- [38] Frauenfelder H. and Steffen R.M. *Alpha-,Beta-,and Gamma-Ray Spectroscopy*. North-Holland Publishing Company, Amsterdam, 1965.
- [39] Lawrence W. Fagg and Stanley S. Hanna. Polarization measurements on nuclear gamma rays. *Rev. Mod. Phys.*, 31:711–758, Jul 1959.
- [40] Werner V. *Proton-neutron symmetry at the limits of collectivity*. PhD thesis, Universität zu Köln, 2004.
- [41] N. Pietralla, Z. Berant, V. N. Litvinenko, S. Hartman, F. F. Mikhailov, I. V. Pinayev, G. Swift, M. W. Ahmed, J. H. Kelley, S. O. Nelson, *et al.* Parity measurements of nuclear levels using a free-electron-laser generated γ -ray beam. *Phys. Rev. Lett.*, 88:012502, Dec 2001.
- [42] Norbert Pietralla. The institute of nuclear physics at the tu darmstadt. *Nucl. Phys. News*, 28(2):4–11, 2018.
- [43] Henry R. Weller, Mohammad W. Ahmed, Haiyan Gao, *et al.* Research opportunities at the upgraded hi γ s facility. *Progress in Particle and Nuclear Physics*, 62(1):257 – 303, 2009.
- [44] K. Sonnabend, D. Savran, J. Beller, *et al.* The darmstadt high-intensity photon setup (dhips) at the s-dalinac. *Nucl. Instrum. Methods Phys. Res. A*, 640(1):6 – 12, 2011.
- [45] C. Romig. private communication.
- [46] C. Romig. Investigation of nuclear structure with relative self-absorption measurements. dissertation, TU Darmstadt, 2015.
- [47] V. N. Litvinenko, B. Burnham, M. Emamian, *et al.* Gamma-ray production in a storage ring free-electron laser. *Phys. Rev. Lett.*, 78:4569–4572, Jun 1997.
- [48] B. Löher, V. Derya, T. Aumann, *et al.* The high-efficiency spectroscopy setup at. *Nucl. Instrum. Methods Phys. Res. A*, 723:136 – 142, 2013.

-
- [49] H. Pai, J. Beller, N. Benouaret, J. Enders, T. Hartmann, O. Karg, P. von Neumann-Cosel, N. Pietralla, V. Yu. Ponomarev, C. Romig, *et al.* Low-lying dipole strength in the $n = 28$ shell-closure nucleus ^{52}Cr . *Phys. Rev. C*, 88:054316, Nov 2013.
- [50] H. Pai, T. Beck, J. Beller, R. Beyer, M. Bhike, V. Derya, U. Gayer, J. Isaak, Krishichayan, J. Kvasil, *et al.* Magnetic dipole excitations of ^{50}Cr . *Phys. Rev. C*, 93:014318, Jan 2016.
- [51] P. C. Ries, H. Pai, T. Beck, J. Beller, M. Bhike, V. Derya, U. Gayer, J. Isaak, B. Löher, Krishichayan, *et al.* Valence-shell dependence of the pygmy dipole resonance: $e1$ strength difference in $^{50,54}\text{Cr}$. *Phys. Rev. C*, 100:021301, Aug 2019.
- [52] J.H. Kelley, E. Kwan, J.E. Purcell, C.G. Sheu, and H.R. Weller. Energy levels of light nuclei $a=11$. *Nuclear Physics A*, 880:88 – 195, 2012.
- [53] J.H. Kelley, J.E. Purcell, and C.G. Sheu. Energy levels of light nuclei $a=12$. *Nuclear Physics A*, 968:71 – 253, 2017.
- [54] Jun Chen. Nuclear data sheets for $a=138$. *Nuclear Data Sheets*, 146:1 – 386, 2017.
- [55] M.J. Martin. Nuclear data sheets for $a = 208$. *Nuclear Data Sheets*, 108(8):1583 – 1806, 2007.
- [56] S. Agostinelli, J. Allison, K. Amako, J. Apostolakis, H. Araujo, P. Arce, M. Asai, D. Axen, S. Banerjee, G. Barrand, *et al.* Geant4—a simulation toolkit. *Nuclear Instruments and Methods in Physics Research Section A: Accelerators, Spectrometers, Detectors and Associated Equipment*, 506(3):250 – 303, 2003.
- [57] G.F. Knoll. *Radiation Detection and Measurement*, volume 3. Wiley Verlag, 2000.

-
- [58] L. I. Schiff. Energy-angle distribution of thin target bremsstrahlung. *Phys. Rev.*, 83:252–253, Jul 1951.
- [59] A. Willis, M. Morlet, N. Marty, C. Djalali, D. Bohle, H. Diesener, A. Richter, and H. Stein. Spin-flip transitions in ^{46}Ti , ^{48}Ti and ^{50}Cr excited by inelastic proton scattering. *Nuclear Physics A*, 499(2):367 – 380, 1989.
- [60] Zoltan Elekes, Janos Timar, and Balraj Singh. Nuclear data sheets for $a = 50$. *Nuclear Data Sheets*, 112(1):1 – 131, 2011.
- [61] Yang Dong and Huo Junde. Nuclear data sheets for $a = 54$. *Nuclear Data Sheets*, 121:1 – 142, 2014.
- [62] D.L. Watson, M.A. Abouzeid, H.T. Fortune, L.C. Bland, and J.B. McGrory. The $^{52}\text{Cr}(t, p)^{54}\text{Cr}$ reaction at $E_t = 15$ mev. *Nuclear Physics A*, 406(2):291 – 305, 1983.
- [63] R. Chapman, S. Hinds, and A.E. MacGregor. A study of ^{52}Cr , ^{54}Cr and ^{56}Cr by the (t, p) reaction. *Nuclear Physics A*, 119(2):305 – 324, 1968.
- [64] A. M. Nathan, J. W. Olness, E. K. Warburton, and J. B. McGrory. Yrast decay schemes from heavy-ion + ^{48}Ca fusion-evaporation reactions. iii. $^{57,58}\text{Fe}$, $^{54,55}\text{Cr}$, and $^{57,58}\text{Mn}$. *Phys. Rev. C*, 17:1008–1025, Mar 1978.
- [65] C. Coceva. Radiative transitions from neutron capture in ^{53}Cr resonances. *Il Nuovo Cimento A*, year = 1994, OPTkey = •, volume = 107, OPTnumber = •, pages = 85-116, OPTmonth = •, OPTnote = •, OPTanote = •.
- [66] J. Wilhelmy, B. A. Brown, P. Erbacher, U. Gayer, J. Isaak, Krishichayan, B. Löher, M. Müscher, H. Pai, N. Pietralla, *et al.* Investigation of $j = 1$ states and their γ -decay behavior in ^{52}Cr . *Phys. Rev. C*, 98:034315, Sep 2018.

-
- [67] B.A. Brown and W.D.M. Rae. The shell-model code nushellx@msu. *Nuclear Data Sheets*, 120:115 – 118, 2014.
- [68] Otsuka T. Brown B.A. et al. Honma, M. Shell-model description of neutron-rich pf-shell nuclei with a new effective interaction gxpf 1. *Eur. Phys. J. A*, 25:499–502, 2005.
- [69] Yang Dong and Huo Junde. Nuclear data sheets for $a = 52$. *Nuclear Data Sheets*, 128:185 – 314, 2015.
- [70] H. K. Toft, A. C. Larsen, A. Bürger, M. Guttormsen, A. Görge, H. T. Nyhus, T. Renstrøm, S. Siem, G. M. Tveten, and A. Voinov. Evolution of the pygmy dipole resonance in sn isotopes. *Phys. Rev. C*, 83:044320, Apr 2011.
- [71] S. Typel and H.H. Wolter. Relativistic mean field calculations with density-dependent meson-nucleon coupling. *Nucl. Phys. A*, 656(3):331 – 364, 1999.
- [72] S. Typel. private communication.
- [73] N. Paar, T. Nikšić, D. Vretenar, and P. Ring. Isotopic dependence of the pygmy dipole resonance. *Physics Letters B*, 606(3):288 – 294, 2005.
- [74] B. Dietz, B. A. Brown, U. Gayer, N. Pietralla, V. Yu. Ponomarev, A. Richter, P. C. Ries, and V. Werner. Chaos and regularity in the spectra of the low-lying dipole excitations of $^{50,52,54}\text{Cr}$. *Phys. Rev. C*, 98:054314, Nov 2018.
- [75] H. Morinaga and T. Yamazaki. *In-beam gamma-ray spectroscopy*. North-Holland publishing company, 1976.
- [76] J. Enders, P. von Brentano, J. Eberth, R.-D. Herzberg, N. Huxel, H. Lenske, P. von Neumann-Cosel, N. Nicolay, N. Pietralla, H. Prade, et al. Photon scattering off ^{52}Cr : Two-phonon $e1$ strength at the $n = 28$ shell closure? *Nuclear Physics A*, 636(2):139 – 155, 1998.

Lebenslauf

Persönliche Daten

| | |
|---------------------|------------------------|
| Name | Philipp Christian Ries |
| Geburtsdatum | 25.07.1988 |
| Geburtsort | Hadamar |
| Staatsangehörigkeit | deutsch |
| Familienstand | ledig |

Schul Ausbildung

| | |
|-----------|-------------------------------------|
| 1995-1999 | Oranienschule, Elz |
| 1999-2008 | Fürst-Johann-Ludwig-Schule, Hadamar |
| Mai 2008 | Abitur |

Hochschulausbildung

| | |
|-----------|---|
| 2009-2012 | Technische Universität Darmstadt B.Sc. Physik <i>Die Charakterisierung von Lanthanbromid-Szintillationsdetektoren</i> |
| 2012-2015 | Technische Universität Darmstadt M.Sc. Physik <i>Untersuchung der Kernstruktur an ^{54}Cr mit Hilfe der Kernresonanzfluoreszenz</i> |
| seit 2015 | Technische Universität Darmstadt Promotionsstudium |

List of publications

C. Romig, T. Beck, J. Beller *et al.*, EPJ Web of Conferences **93**, 01035 (2015)

M. Zweidinger, T. Beck, J. Beller *et al.*, AIP Conference Proceedings **1645**, 259 (2015)

T. Beck, J. Beller, V. Derya *et al.*, AIP Conference Proceedings **1681**, 040007 (2015)

P.C. Ries, T. Beck, J. Beller *et al.*, J. Phys. Conf. Ser. **724** 012040 (2016)

H. Pai, T. Beck, J. Beller *et al.*, Phys. Rev. C **93**, 014318 (2016)

J. Wilhelmy, P. Erbacher, U. Gayer *et al.*, J. Phys. Conf. Ser. **966** 012035 (2018)

V. Werner, U. Gayer, J. Kleemann *et al.*, J. Phys. Conf. Ser. **1056** 012061 (2018)

-
- J. Wilhelmy, B.A. Brown, P. Erbacher *et al.*, Phys. Rev. C **98**, 034315 (2018)
- U. Gayer, V. Werner, T. Beck *et al.*, EPJ Web of Conferences **194**, 02004 (2018)
- B. Dietz, B.A. Brown, U. Gayer *et al.*, Phys. Rev. C **98**, 054314 (2018)
- P.C. Ries, H. Pai, T. Beck *et al.*, Phys. Rev. C **100**, 021301(R) (2019)
- P.C. Ries, T. Beck, J. Beller *et al.*, Springer Proceedings in Physics **225**, 233 (2018)
- U. Gayer, T. Beck, M. Bhike *et al.*, Phys. Rev. C **100**, 034305 (2019)
- M. Hilcker, J. Birkhan, A. D'Alessio *et al.*, Nucl. Instrum. Methods A **957**, 163418 (2020)
- C. Douma, K. Zuber, P.C. Ries *et al.*, Eur. Phys. J. A **56**, 2 (2020)

Danksagung

Es gibt viele Leute, die mich in den vergangenen Jahren mit Rat und Tat unterstützt haben und denen ich hier meinen herzlichsten Dank aussprechen möchte.

Ich möchte zunächst **Prof. Dr. Dr. hc mult. Norbert Pietralla** dafür danken, mir die Gelegenheit gegeben zu haben, in seiner Arbeitsgruppe diese Doktorarbeit anfertigen zu dürfen. Trotz seiner zahlreichen Verpflichtungen, hat er stets ein offenes Ohr für Fragen und Diskussionen. Auch dass mir die Möglichkeiten gegeben wurden, diverse Konferenzen oder Experimente zu besuchen, selbst in fernen Ländern wie den USA und Japan, ist keine Selbstverständlichkeit, wofür ich ebenfalls äußerst dankbar bin.

Ein besonderer Dank geht an all die Personen, die mit Wartung und Betrieb der Beschleunigeranlagen S-DALINAC und $HI\gamma S$ die nötigen Experimente überhaupt erst möglich gemacht haben. Die Beschleunigergruppe selbst, aber auch Betriebsgruppe und Werkstattpersonal, haben darüber hinaus oft mit ihrer langjährigen Erfahrung aus der Patsche geholfen.

Ebenfalls herzlich bedanken möchte ich mich bei **Dr. Volker Werner**, der als Betreuer und Leiter der KRF-Gruppe sich um jedes noch so kleine Wehwehchen kümmern musste, es aber stets gerne tat. Auch für das Korrekturlesen meiner Arbeit bedanke ich mich.

Ich werde schmerzlich die beispiellose Kameradschaft und Zusammenarbeit mit meinen Kolleginnen und Kollegen der Arbeitsgruppe vermissen. Gab es doch einen steten Wandel der Besetzung, so sei nichtsdestotrotz hier jedem einzelnen, **Dr. Esra Aciksöz, Tobias Beck, Marcel Berger, Dr. Udo Friman-Gayer, Katharina Ide, Jörn Kleemann, Dr. Haridas Pai, Oliver Papst, Dr. Christopher Romig, Dr. Volker Werner und Dr. Markus Zweidinger**, gedankt. Ich möchte ebenfalls die Mitglieder der Spektrometergruppe erwähnen, mit denen ich aufgrund der verschiedenen Aufgaben, die mir anvertraut wurden, eng zusammen arbeitete. Vielen Dank an **Antonio D'Alessio, Dr. Sergej Bassauer, Dr. Jonny Birkhan, Michaela Hilcker, Dr. Johann Isaak, Tobias Klaus, Prof. Andreas Krugmann, Prof. von Neumann-Cosel, Dr. Maxim Singer und Gerhart Steinhilber**.

Ich möchte auch ein herzliches Dankeschön an das Personal im Sekretariat, **Marco Brunken, Jessica Kramer, Catja Noll de Lopez, Carina Seeger und Giovanna Umberti-Caroli** aussprechen, die mit ihrem unermüdlichen Schaffen abseits der wissenschaftlichen Arbeit für alles Organisatorische Sorge tragen.

Wie für viele der bereits namentlich Erwähnten, bedanke ich mich bei **Axel Frotscher, Ralph Kern, Laura Mertes, Dr. Philipp Napiralla, Dr. Johannes Wiederhold und Dr. Waldemar Witt**, die ich ebenfalls während meiner Zeit am IKP gleichsam als Freunde gewinnen konnte, und halfen, abseits vom Institut den Stress der Arbeit zu abzubauen.

Auch fern abseits dieses Trubels fand ich immer wieder die nötige seelische Unterstützung bei meiner Familie. Größter Dank geht an meine Eltern **Roswitha und Peter**, an meine Schwester **Juliane** und ihrem Ehemann **Fredrik** sowie an meinen Bruder **Patrick** und seiner Ehefrau **Sandra**.

Ich bedanke mich bei der Deutschen Forschungsgemeinschaft, die diese Arbeit im Rahmen des Sonderforschungsbereichs 1245 finanziell unterstützte.

Ebenso geht Dank an die Helmholtz Gesellschaft, die diese Arbeit durch die Helmholtz Graduate School for Hadron and Ion Research (HGS-HIRe) unterstützte.